THESIS FOR THE DEGREE OF LICENTIATE OF ENGINEERING

Water and alkali salts in the hydrating and hardened green cement-based materials

Hydration process, moisture content and transport

Liming Huang

Division of Building Technology

Department of Architecture and Civil Engineering

CHALMERS UNIVERSITY OF TECHNOLOGY

Gothenburg, Sweden 2022

Water and alkali salts in the hydrating and hardened green cement-based materials

Hydration process, moisture content and transport

Liming Huang

Technical report ACE 2022:1,

Lic /Architecture and Civil Engineering / Chalmers University of Technology

Department of Architecture and Civil Engineering
Division of Building Technology
Chalmers University of Technology
SE-412 96 Gothenburg
Sweden
Telephone + 46 (0)70-879 1506
Author e-mail: limingh@chalmers.se

Cover:

Graphical illustration of the theme of this research

Chalmers Reproservice
Gothenburg, Sweden 2022

Water and alkali salts in the hydrating and hardened green cement-based materials

Hydration process, moisture content and transport

LIMING HUANG
Department of Architecture and Civil Engineering
Division of Building Technology, Building materials
Chalmers University of Technology

Abstract

Reducing CO_2 emissions in the production of cementitious binder is the most effective way to decrease the environmental impact of the construction industry, so a large amount of supplementary cementitious materials (SCMs) has been used in the green concrete. Both the SCMs and alkali salts in binders influence the hydration process and the structure in hardened cement-based materials. Experiments were performed to investigate the effects of them on the hydration reaction in fresh paste, the pore structure and moisture transport in hardened pastes because these properties determine the durability of concrete during its service life. The composition and morphology of hydration products were determined by X-ray diffraction (XRD) and scanning electron microscopy (SEM). The electrical conductivity of hydrating paste was real-time monitored by a newly invented device to detect the structure change during hydration. An easy procedure was developed to determine the water distribution in paste. Electrical conductivity of the pore solution was calculated with the volume of evaporable water and chemical composition of the binders. The moisture transport in hardened pastes was measured by the new procedure and setup. The chloride migration in paste was measured by the rapid chloride migration method (RCM). The mercury intrusion porosimeter (MIP) was used to test the pore size distribution.

The results show that the precipitation of C-S-H is a nonclassical nucleation process. The initial structure building starts with the nucleation of primary globules. It grows by particle attachment and potassium salts influence not only the size of primary globule floc but also the packing orientation. A large increase in the heat release after the induction period may be due to the growing attachment rate of flocs instead of the dissolution of etch pits. The duration of induction period correlates to the size of primary floc. Al ion will change the size of floc to prolong the low-rate period, but alkali salts can mitigate the effect from it. A hypothesis regarding the dissolution of C_3S and the nucleation of C-S-H within the near-surface region narrows the gap in the current theories.

The hydration reactivity of binders can be indicated by the evolution of electrical conductivity, formation factor and its growth rate in the hydrating pastes. The electrical properties of pastes are related to the setting, pore connectivity and volume of evaporable water. An increase in the water-binder ratio (*w/b*) lowers the electrical conductivity of pore solution due to the dilution of alkali concentration. However, it increases the connectivity of pore solution and reduces the formation factor of pastes. The blending of slag decreases the conductivity of pore solution and increases the formation factor. Fly ash induces a higher connectivity of pores at the early age owing to its lower reactivity compared to clinker, but the connectivity of pores in the fly ash paste is much lower than the plain pastes after long-term hydration (1 year). Limestone increases the connectivity of pore solution at the early age, but its filling effect becomes effective after a certain hydration age. The relationship between volume of evaporable water and formation factor can be well demonstrated by the extended percolation theory, and this provides theoretical basis for an in-situ detecting of evaporable water in pastes by electrical conductivity.

The procedure developed in this study can measure the moisture transport properties in both steady-state and non-steady state transport condition. The moisture transport coefficient in the hardened cement paste is RH dependent. The differences in RH dependency are due to discrepancies in the critical RH for percolation of liquid in pastes. The blended pastes have a more complex pore structure and lower concentration of alkali ions in pore solution, so the critical RH of the blended pastes is higher than that of OPC. The blending of fly ash and slag evidently reduce the moisture and chloride diffusivity in pastes due to its reduction effect in formation factor and pore connectivity. Formation factor is the major determinant for the moisture transport at a high RH interval, but porosity of small pores (middle capillary and mesopores) becomes the major determinant at a low RH. This study provides the meaningful data for the prediction and simulation of moisture and ion (e.g. chloride) transport in concrete during its service life with a continuous long-term hydration.

Keywords:

Sustainable cement-based materials; supplementary cementitious materials; alkali salts; hydration; electrical conductivity; pore structure; formation factor; moisture transport

Vatten och alkalisalter i hydratiserande och hårdnande gröna cementbaserade materialen

Hydratationsprocess, vattenhalt och fukttransport

LIMING HUANG
Institutionen för Arkitektur och samhällsbyggnadsteknik
Avdelningen för Byggnadsteknologi, byggmaterial
Chalmers tekniska högskola

Sammanfattning

Att minska koldioxidutsläppen vid tillverkningen av bindemedel är det mest effektiva sättet att minska miljöpåverkan i byggbranschen, så en stor mängd mineraliska tillsatsmaterial har använts i grön betong. De alternativa materialen tillför extra alkalisalter i cementmassorna, vilket påverkar hydratationssprocessen och strukturen i härdade cementbaserade material. Flera experiment utfördes för att undersöka effekten av alkalisalter och tillsatsmaterial på hydratationssprocessen, strukturen och fuktfördelningen i härdade prover. Hydrationsprodukternas sammansättning och morfologi bestämdes med hjälp av röntgendiffraktion (XRD) och svepelektronmikroskopi (SEM). Den elektriska ledningsförmågan hos hydrerande pasta övervakades i realtid med hjälp av en nyuppfunnen anordning för att upptäcka strukturförändringen under hydratation. Ett enkelt förfarande skapades för att bestämma vattenfördelningen i pastan. Porlösningens ledningsförmåga beräknades med hjälp av volymen av förångningsbart vatten och den kemiska sammansättningen av bindemedlen. Fuktsfördelningen i härdade pastor mättes med hjälp av det utvecklade metoden och utrustningen. Kloridmigrationen i pastan bestämdes med hjälp av kloridmigrationsmetoden (RCM). Kvicksilverintrusionsporosimetern (MIP) användes för att bestämma porstorleksfördelningen i de härdade pastorna.

Resultaten visar att utfällningen av C-S-H är en icke-klassisk kärnbildningsprocess. Den inledande strukturbildningen börjar med kärnbildning av primära globuler. Den växer genom partikelfästning och kaliumsalter påverkar inte bara storleken på den primära globulära flockens storlek utan även packningsorienteringen. Den stora ökningen av värmeavgivningen efter induktionsperioden kan bero på att flockarnas fästningshastighet ökar i stället för på upplösningen av etsningsgroparna. Induktionsperiodens längd korrelerar med storleken på de primära flockarna. Al-joner kommer att förändra flockens storlek och förlänga perioden med låg hastighet, men alkalisalter kan mildra effekten av detta. En hypotes om upplösningen av C_3S och kärnbildning av C-S-H i området nära ytan kan minska gapet i de nuvarande teorierna.

Bindemedlens hydreringsreaktivitet kan indikeras av utvecklingen av den elektriska ledningsförmågan, formationsfaktorn och dess tillväxttakt i de hydratiserande cementpastorna. Cementmassornas ledningsegenskaper är relaterade till tillstyvnande, porernas förbindelse och volymen av avdunstningsbart vatten. En ökning av förhållandet mellan vatten och bindemedel (*w*/*b*) sänker porlösningens ledningsförmåga på grund av utspädningen av alkalikoncentrationen. Det ökar dock porlösningens förbindelse och minskar formationsfaktorn för pastorerna. Blandning av slagg minskar porlösningens ledningsförmåga och ökar formationsfaktorn. Flygaska ger en högre förbindelse hos porerna vid tidig ålder på grund av dess lägre reaktivitet jämfört med klinker, men förbindelse hos porerna i flygaskpasta är mycket lägre än vanlig pasta efter långvarig hydratation (1 år). Kalksten ökar porlösningens förbindelse vid tidig ålder, men dess fyllningseffekt är effektiv efter en viss hydratationssålder. Förhållandet mellan volymen av avdunstningsbart vatten och formationsfaktorn kan påvisas väl med hjälp av den utvidgade perkolationsteorin. Detta ger teoretiskt stöd för en in situ-detektion av förångningsbart vatten i pastorerna genom att bestämma den elektriska ledningsförmågan.

Det utvecklade förfarandet kan mäta ångdiffusionskoefficienten och den totala fuktdiffusionskoefficienten för samma prov i ett och samma förfarande. Fukttransportkoefficienten i den härdade cementpastan är RF-beroende. Skillnaden i RF-beroendet beror på att den kritiska RF-nivån för perkolation av vätska i pastor är olika. De pastor med tillsatsmaterial har en mer komplex porstruktur och lägre koncentration av alkalijoner i porlösningen, vilket innebär att den kritiska RF för dessa är högre än för de baserade på enbart portlandcement. Inblandning av flygaska och slagg minskar uppenbarligen fukt- och kloriddiffusionen i pastorna på grund av den minskade effekten på bildningsfaktorn och porernas förbindelse. Formationsfaktorn är den viktigaste parametern för fukttransporten vid hög RF, men porositeten hos små porer (mellankapillär- och mesoporer) blir den viktigaste faktorn vid låg RF. Denna studie ger meningsfulla data för förutsägelse och simulering av fuktdiffusion och joninträngning (t.ex. klorider) i betong under dess livslängd i samband med kontinuerlig långvarig hydratation.

Nyckelord:

Hållbara cementbaserade material; kompletterande cementmaterial; alkalisalter; hydratation; elektrisk konduktivitet; porstruktur; fukttransport

Acknowledgement

I would firstly like to express my heartfelt thanks to my academic supervisor, Luping Tang and Zhenghong Yang. I appreciate your guidance and support in my long journey of pursuing knowledge. The fruitful discussion with you inspires me a lot for coming up with novel ideas to deal with research nodus. Thanks also goes to my assistant supervisor, Ingemar Löfgren, Jan Swenson, Nilla Olsson and Itai Panas, for your helpful discussion in the experimental design and the understanding of results during the reference group meeting. I would also like to present my gratitude to Lars Wadsö and Ingemar Segerholm for the collaboration in lab work and good suggestions in experiments.

My sincere gratitude also goes to all the colleagues. Thank you for the help in lab work and the happy daily talk during fika time. This gives me much energy in both work and life during the special corona period. I would like to thank all the members in my family for the endless support in my work and life overseas. I express my special thanks to the colleagues in the Physic and Chemistry department for the collaboration in experiments test. Finally, the colleagues in building materials group are appreciated for the challenging discussion and collaboration.

The author appreciates the financial support from Swedish Research Council for Environment, Agricultural Sciences and Spatial Planning (FORMAS) [Grant No. 2018-01430] and National Key Research and Development Program of China [No. 2018YFD1101002]. I also appreciate the partially financial supports from Thomas Concrete Group, SBUF (the construction industry's organization for research and development) and Cementa AB.

Liming Huang

Gothenburg, January 2022.

List of Publications

This licentiate thesis is based mainly on the work presented in the following publications:

I. Liming Huang, Luping Tang, Haitao Gu, Zhen Li, Zhenghong Yang, "New insights into the reaction of tricalcium silicate (C_3S) with solutions to the end of the induction period" Cement and Concrete Research 152 (2022) 106688.

II. Liming Huang, Luping Tang, Ingemar Löfgren, Nilla Olsson, Zhenghong Yang, "Real-time monitoring the structure evolution of cement-based materials during hydration with the electrical properties", preprint submitted to Cement and Concrete Composites, Jan., 2022 (under review).

III. Liming Huang, Luping Tang, Ingemar Löfgren, Nilla Olsson, Zhenghong Yang, Yongqiang Li, "Moisture and ion transport properties in the blended pastes and their relation to the refined pore structure", preprint submitted to Cement and Concrete Research, Feb., 2022.

Additional Publications

Other publications that are related to the content of the thesis are listed below.

IV. Liming Huang, Luping Tang, Ingemar Löfgren, Nilla Olsson. "Water distribution in green cementitious materials under different relative humidity" *proceedings of ERICA-CASH II Final Conference*, Heidelberg, Germany, January, 2021.

Contents

Abbreviations

SCMs	Supplementary cementitious materials
XRD	X-ray diffraction
SEM	Scanning electron microscopy
RCM	Rapid chloride migration method
MIP	Mercury intrusion porosimeter
OPC	Ordinary Portland cement
hcp	Hardened cement-based pastes
C-S-H	Calcium silicate hydrates
C-A-S-H	Calcium aluminosilicate hydrates
LD C-S-H	Low density calcium silicate hydrates
HD C-S-H	High density calcium silicate hydrates
w/b	Water to binder ratio
F	Formation factor
CP	Critical entry pore size
C_3S	Tricalcium silicate
C_3A	Tricalcium aluminate
IP	Induction period
FA	Fly ash
SL	Slag
LL	Limestone powder
RH	Relative humidity
D_v	The vapor diffusion coefficient
D_w	The total moisture transport coefficient
D_{RCM}	Chloride migration coefficient by RCM test
$D_{v,s}$	The diffusion coefficient by semi-infinite drying
Epw	Evaporable water
Nw	Nonevaporable water

1 Introduction

This chapter will start with a brief introduction on the background of this study. The main purpose for this thesis will be illustrated in the section 1.2. The main content of this thesis includes three divergent directions, which is internally connected by the theoretical framework in the section 1.3. The limitations in the whole framework and the experimental investigation have been specified in the last section of this chapter.

1.1 Background

Cement is the most widely used materials in construction, covering residential and commercial buildings, bridges and roads. According to statistics, the global cement consumption reached 4.13 billion tons in 2016 [1] and this value is expected to reach 4.68 billion tons in 2050 [2]. The production of ordinary Portland cement (OPC) consumes a lot of energy and releases massive CO_2 due to the large demand of concrete. It is the third largest energy-consuming industry, with CO_2 release accounting for 6–7% of anthropogenic CO_2 emissions and 4–5% of greenhouse gases [3,4]. In response to energy conservation and emission reduction for the sustainable development, plenty of alternative raw fuels are used in cement production [5,6]. Meanwhile, the blending of SCMs is the most efficiency way to decrease the clinker content in cement [7], thus reducing the emission from its production. Both alternative raw fuels and SCMs brings more foreign trace elements in cement-based concrete compared to the traditional production process. Sulfur (S) and potassium (K) are the typical representatives in the introduced elements in the blended pastes. In addition, sulfates were used as an activator in cement-based concrete to boost the reactivity of SCMs [8].

SCMs make impact on the hydration of OPC as well as the microstructure in the hardened cement-based pastes (hcp), which affects the properties of fresh slurry (setting time and rheology), the hardened properties and the durability of concrete. Alkali sulfates also alters the hydration process [9–11], so that they change the setting and rheology of fresh pastes, and the microstructure in both plain and the blended concrete [12,13]. During the hydration without introducing extra alkali salts, the C-S-H grows with a morphology of long needle-like structures and finally links together. However, C-S-H grows in a dispersed single needle-like morphology with the presence of alkali sulfates or calcium sulfates. When only alkali ions are added, C-S-H grows in the short tree-shape structure attached on the surface of the unhydrated particles as shown in [10,14]. Several different build-up patterns of products cause a large difference in the pore structure, thus affecting the strength, shrinkage, durability of the hcp.

The effects of SCMs on the microstructure of the main hydration products, C-S-H and CH, have attracted plenty of research attention. Berodier and Scrivener [15] reported that the volume of hydration products in the blended pastes is lower than that in the OPC paste, so SCMs increased the total porosity of the hcp. However, the pore structure is refined because of the filling effect of later age hydration products from SCMs. Some studies found that the incorporation of slag can also reduce total porosity at an early stage and enforce a pore refinement effect [16]. The mechanical performance of the modified hydration products was evaluated by means of nanoindentation in some previous investigations. It was found that the blending of silica fume, fly ash, slag and metakaolin altered the elastic modulus of hydration products. The specific trend of change is closely related to the water to binder ratio (*w/b*) and the amount of mineral blending [17,18]. Some studies found that the incorporation of SCMs has no effect on the performance of low-density (LD) C-S-H and high-density (HD) C-S-H itself, but it increases the percentage of HD C-S-H in the composition of hcp. Wilson [19] found that the chemical structure of calcium aluminosilicate hydrate (C-A-S-H) was largely modified in hcp with *w/b* of 0.4, but the mechanical properties fluctuate only in a small range (e.g., modulus is in the range of 25–27 GPa). Nonetheless, the variation in the percentage of LD and HD C-S-H in the hcp have a significant influence on the mass transport process in hcp. The mass transport in hcp is determined by the multiscale pore structure in hcp from about 5 Å up to 10 μm and microstructure of C-S-H as illustrated in Figure 1.1.

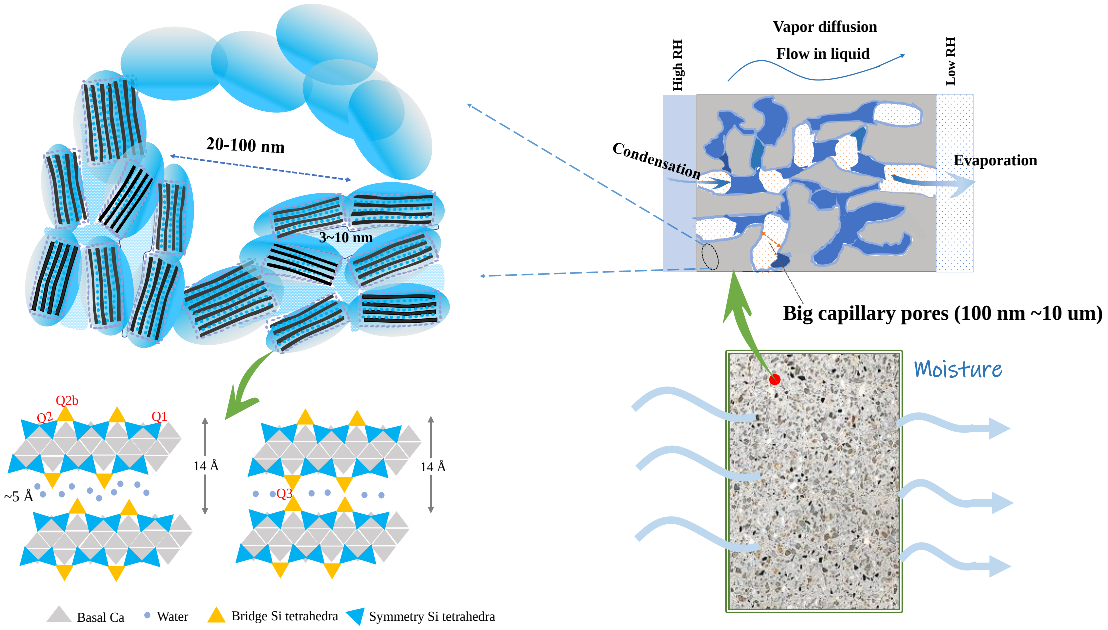

Multiscale pore size distribution from ~5 Å to 10 µm related to transport process

Figure 1.1. A sketch of multiscale pore distribution in the hcp related to the moisture and ions transport properties.

In 2000, Jennings [20] proposed a holistic C-S-H structural model based on the results from the small-angle X-ray diffraction and small-angle neutron diffraction, in which the structure of LD and HD C-S-H were detailly interpreted. Allen [21] quantitatively characterized the chemical structure of C-S-H with the specific mole ratio of the bound and adsorbed water so that the true density of C-S-H was accurately determined. Based on the above research, Jennings [22] proposed a more detailed globular particle model, and this model has been adopted in this paper (see Figure 1.1) and illustrated at nanoscale. In this model, the pores inside the hcp can be divided into four categories. the size of the interlayer gel pore is about several layers of water molecules (5–25 Å) and the gel pore is a pore formed by the overlapping of globular floc, which can be subdivided into small gel pores and large gel pores, corresponding to 1–3 nm and 3–12 nm, respectively. The size of the capillary pores is in a wide range from 20 nm to10 μm depending on the *w/b*. Mehta and Monteiro [23] classified the pores in hcp into 4 categories with respect to their effect on strength and mass transport properties, that is, gel micropores (<4.5 nm), mesopores (4.5–50 nm), middle capillary pores (50–100 nm) and large capillary pores (>100 nm). The percentage and absolute volume of pores with variant sizes determine the moisture and ion transport properties in hcp.

The correlation between the refined pore structure and mass transport properties in hcp is still lack of a clear clarification due to complexity of pore structure in hcp. In addition, the transport process relates not only to the pore structure but also to the alkali concentration in the pore solution. Ionic conductivity of pore solution is mainly determined by the alkali concentration in hcp with normal *w/b* (<20). The alkali concentration in hcp can be calculated based on the chemical compositions of binders and their hydration degree [24]. Therefore, the pore structure properties, such as formation factor (*F*), detected by the electrical conductivity test may appropriately reflect the effect of pore solution in the evaluation of transport properties. Many published papers intended to correlate the transport properties to the pore structure parameters from mercury intrusion porosimeter test (MIP), for instance, the critical entry pore size (CP) [25–27]. However, CP as the determinant can hardly explain the fact that FA blended mortar has a much lower vapor diffusion but with a higher CP compared to OPC mortar.

The mechanism of the bottom-up structure formation during the hydration is of great importance but lack of research attention. This work tried to reveal the effect of potassium salts on the packing of globular floc up to the end of induction period, which is the initial process for the structure building. Thereafter, the electrical conductivity of cement pastes during hydration were measured as an index for structure evolution up to 12 days. There are many unsolved problems in the hydration of pure minerals and cement, which deserves the further investigations. Finally, the effects of SCMs on the moisture or chloride transport properties in hcp were detailly discussed by correlating them with several pore structure parameters.

There are several methods to determine the moisture transport properties based on steady-state conditions (constant flux through discs, such as cup method [28]) or non-steady state conditions (such as semi-infinite drying) [29]. The cup method takes a long time (almost 6 months) to get the equilibrium for a constant flux, which also depends on the dimension of slabs and sealing conditions. These methods are time-consuming because of a long-term equilibrium time. In addition, the experiments are only able to be operated in the labs with special setup. An in-situ monitoring of moisture loss in the cement-based concrete is meaningful for the utilization of green binders in the modern construction, so it is urgent to invent some novel methods with the proper theories and to build models for the application of these methods.

1.2 Objectives

Alkali salts affect the hydration of C_3S to change heat release evolution and modify the morphology of C-S-H in hydration products. This work aims to reveal the underlying mechanism in the building-up of C-S-H structure during the early hydration with and without potassium salts. The real-time monitoring of electrical conductivity was operated to investigate the structure evolution in both the plain and blended pastes during the hydration process. The efforts were paid to explore the potential use of electrical conductivity for indicating the moisture content in hcp. To measure the transport of moisture in hcp under both steady and non-steady state, a new setup and the corresponding procedure were described in detail. The pore size distribution in the hcp was tested by MIP to identify a clear correlation between pore structure and moisture or chloride transport in hcp. The following questions have been addressed in the present work:

- How do K_2SO_4, KOH and C_3A influence the precipitation of C-S-H during the early hydration?
- What is the relationship between the duration of induction period and size of globular flocs?
- How do SCMs influence the structure evolution of pastes during hydration up to 12 days, based on the real-time monitoring of electrical conductivity?
- How can we operate a nondestructive measurement on the moisture content in hcp on-site?
- Which structure parameter is the determinant on the moisture and chloride transport properties in hcp?
- What is the refinement effect from the SCMs on the pore structure in hcp under the sealed curing?

1.3 Theoretical framework

After mixing with water, the hydration of cement initiates with the quick dissolution of minerals. The concentration of ions (Ca, Al, Si and S etc.) in the bulk pore solution increases as the dissolution proceeds, which will in turn suppress the dissolution of minerals to slow down the hydration process. This was the widely adopted dissolution theory. However, the dissolution of minerals is controlled by the density of dissociated ion complex attached on its surface instead of ions in bulk pore solution. The colloidal structure of the dissolved minerals builds a saturation state in a local region. Precipitation of C-S-H in the local region is a non-classical nucleation process. It starts with the nucleation of primary globule as shown in Figure 1.2 and then grows by particle attachment to pack up the main structure of hcp.

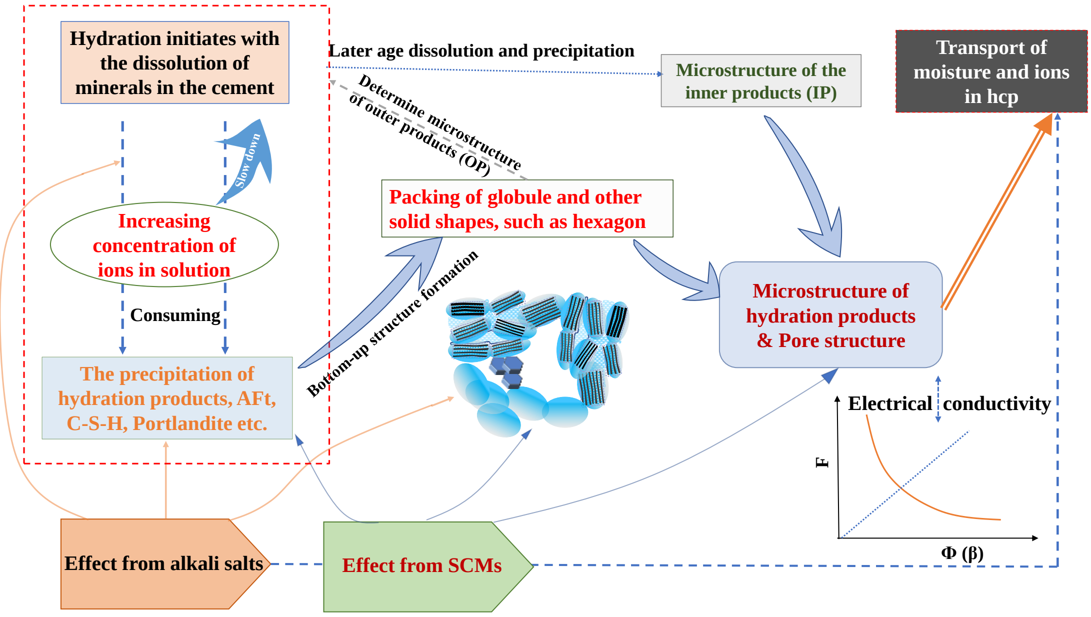

Figure 1.2. Illustration of theoretical framework by a flowchart.

Alkali and sulfate ions alter the ionic species in the solution so that they influence the dissolution of minerals, nucleation kinetic of primary globule and the packing preference of particles. These effects change the bottom-up structure formation of the outer products in hcp, which in turns determines the dissolution of minerals and precipitation of the inner products at later age. SCMs provide the nuclei during the hydration after its dissolution, so it will change the precipitation of products. Moreover, the latent hydraulic activity of SL and the secondary hydration of FA modify the structure of both outer and inner hydration products in hcp.

The effects from SCMs on the moisture content, water accessible porosity and pore connection change the electrical conductivity of pore solution and hcp. Therefore, the measurement of electrical conductivity in the pastes during hydration can indicate the differences in the structure growth of hcp. The transport of moisture and migration of chloride in hcp are mainly controlled by the pore structure, which can be indexed by pore size and Formation factor (*F*) of hcp by taking electrical conductivity of pore solution into consideration.

1.4 Limitations

The chemical composition in binders is an important parameter for the calculation of conductivity of pore solution. Compositions of oxide in Table 2.1 were measured by the X-ray fluorescence, so it is not the actual content of the dissolvable alkali in binders. Therefore, we introduced a modifying equation, but there are still some deviations between the actual concentration and the calculated value. The determination of water content in hcp by the invented procedure neglects the carbonation in pastes during hydration, but this effect is weak in pastes at early hydration. The sample for moisture diffusion test is limited in small sizes in this study, so it may need some modification in the coefficient due to the size effect if we apply it in the practical model for predicting the moisture properties of buildings.

The dissolution and precipitation only occur in the interface of solid contacting with solution, but all the analysis are based on the SEM images of the dried samples instead of the in-situ measurement. Therefore, the main conclusion for the nucleation of C-S-H at early hydration is based on these two assumptions: Firstly, the solvent exchange treatment by isopropanol has the same effect on all samples hydrating in different solutions; Secondly, the freeze-dry and the plating of Au have the negligible effects on the sizes and number of etch pit on particles surface.

The packing of hydration products from induction period to the main hydration peak is a very complex process, but it is the main process that determines the structure of hardened pastes. This study only investigated the details in nucleation process at very early age and the structure information after the main peak was indexed by the electrical conductivity. The correlation between the spatial packing of hydration products and the pore size distribution or the electrical properties is lack of quantitative mathematical expression. The direct measurement of conductivity in pastes would be affected by many factors, such as temperature or polarization of electrode, so the indication of moisture content at early age is not as valid as the later age. Moreover, there is weak general correlation between the moisture content and conductivity in pastes with different binder mixtures. The invented procedure and setup for moisture transport test can only be operated in the lab with a good curing condition and the limited dimensions. The investigation in this study was focused on the hcp. The moisture transport in the hcp may be different from that in the concrete because of the presence of aggregates. Therefore, the further study for application of the theory from hcp to concrete is needed.

2 Materials and methods

This chapter provides the detail information about the raw materials, the procedure for mixing and casting of the samples, and the setting of instrument measurement. The setup for conductivity test and the new setup for moisture transport test are described in this part. Some equations are illustrated to determine the content of the evaporable water and nonevaporable water in hcp.

2.1 Raw materials

2.1.1 Pure minerals

The triclinic tricalcium silicate (C_3S) and cubic tricalcium aluminate (C_3A) were purchased from DMT Materials Technology Co., Ltd. The specific surface area of C_3A powder is 1.26 m^2/g. C_3S has a purity of 98.57% and a specific surface area of 1.92 m^2/g. The particle size distribution of C_3S powder is presented in Figure 2.1. The majority of C_3S has a size smaller than 10 μm. Some analytical reagents were used in the experimental investigation, including NaCl, KCl, KOH, K_2SO_4 and AR sulfuric acid (CAS:7664-93-9).

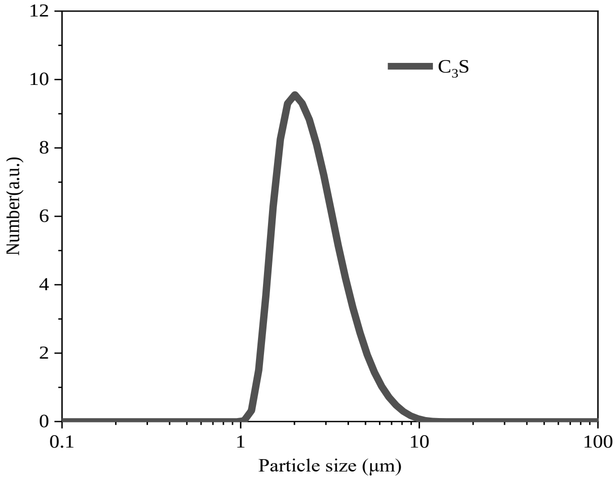

Figure 2.1. Particle size distribution of C_3S.

2.1.2 Cement and SCMs

Cement is an ordinary Portland cement (CEM I 52.5 R) with a Blaine surface of 525 m^2/kg. Three kinds of SCMs were used in the experiments: slag Bremen (SL) with a Blaine surface of 420 m^2/kg from Thomas cement; fly ash (FA) from Cementa; limestone powder from Nordkalk, Limus 15 with a D_{50}=18 µm (LL). The chemical composition of each binder is shown in Table 2.1. The limestone has a calcite content ~89% and 9% SiO_2. Figure 2.2 shows the particle size distribution of the raw materials. LL filler has the finest particle size among all the binders.

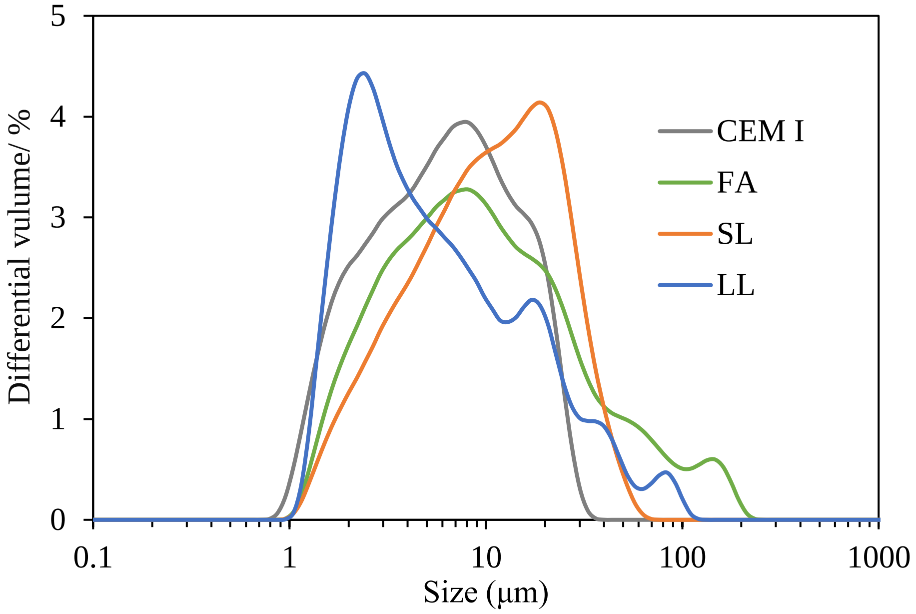

Figure 2.2. Particle size distribution of binders.

Table 2.1. Chemical composition of different binders (*LOI*: loss of ignition; δ_i: mole of chemical composition per gram binder).

Chemical Composition	CEM I 52.5 R		Slag		Fly ash		Limestone
	wt%	δ_i(mol/g)	wt%	δ_i(mol/g)	wt%	δ_i(mol/g)	wt%
CaO	62.2	1.11×10^{-02}	39.11	6.98×10^{-03}	5.1	9.11×10^{-04}	49.5
SiO_2	19.6	3.06×10^{-03}	36.63	5.72×10^{-03}	54.6	8.53×10^{-03}	9.0
Al_2O_3	4.5	4.41×10^{-04}	13.56	1.33×10^{-03}	22.4	2.20×10^{-03}	0.6
Fe_2O_3	3	1.88×10^{-04}	0.49	3.06×10^{-05}	8.7	5.44×10^{-04}	0.3
SO_3	3.5	4.38×10^{-04}	0.27	3.38×10^{-05}	0.8	1.00×10^{-04}	0.03
MgO	3.5	8.75×10^{-04}	8.52	2.13×10^{-03}	1.8	4.50×10^{-04}	-
K_2O	1.01	1.07×10^{-04}	0.57	6.06×10^{-05}	2.1	2.23×10^{-04}	0.3
Na_2O	0.27	4.35×10^{-05}	0.42	6.77×10^{-05}	1	1.61×10^{-04}	0.1
Cl	0.07	1.97×10^{-05}	0.009	2.54×10^{-06}	-	-	-
Sulfide	-	-	0.73*	-	-	-	
LOI	2.5		-1.07		3.5		40.1

*Note: The sulfide in slag will be oxidized during the LOI test, so this induces an increase of weight. Although the hydration also makes oxidization of sulfide [30], we assume that its oxidization is rare due to the low hydration degree at the early age.

2.2 Preparation of samples

2.2.1 Minerals at early hydration

C_3S was mixed with three different kinds of solutions with a solid to solution ratio of 0.5 at 25 °C. The liquid includes the deionized water (TC_3S), 0.06 g/mL KOH solution (KH) and 0.06 g/mL K_2SO_4 solution (KS). All samples were stirred for 1 min in a glovebox with N_2 gas and then they were cured in this box before we took them out to stop hydration. The hydration was stopped at 0.5 h by solvent exchange.

C_3A was used to replace a part of the C_3S to make a C_3S:C_3A mixture system (90%:10% by weight). The hydration of mixture system with the deionized water, KH, and KS were conducted with a solution to solid ratio of 0.5 at 25 °C in the glovebox. It was stopped at 4 h by immersing the samples into liquid nitrogen and then samples were quickly moved into a freeze-drying machine at -50 °C and 0.7 Pa for 3 days. The same procedure was used to stop the hydration of a reference sample (pure C_3S with deionized water).

2.2.2 Preparation of pastes

Table 2.2 shows the mixing proportion of 11 samples. In binary systems, OPC was replaced with 35% FA or SL by weight. In the ternary system, OPC was replaced with 35% SL and 16% LL. Pastes were mixed with three different water-binder ratios (*w/b*) with 0.35, 0.45 and 0.55 respectively, except for the fly ash pastes with two *w/b* (0.35 and 0.45), due to the fact that there is less availability of FA in the future.

Table 2.2. The mix proportion of samples (LOI_b: the normalized loss of ignition of binder system).

Samples	Binder	*w/b*	LOI_b
P035	OPC (SH P Slite CEM I 52.5 R)	0.35	2.5%
P045	OPC (SH P Slite CEM I 52.5 R)	0.45	
P055	OPC (SH P Slite CEM I 52.5 R)	0.55	
P135	65%OPC+35%FA	0.35	2.85%
P145	65%OPC+35%FA	0.45	
P235	65%OPC+35%SL	0.35	1.2%
P245	65%OPC+35%SL	0.45	
P255	65%OPC+35%SL	0.55	
P335	49%OPC+35%SL+16%LL	0.35	0.85%
P345	49%OPC+35%SL+16%LL	0.45	
P355	49%OPC+35%SL+16%LL	0.55	

The pastes were homogeneously mixed in a planetary mixer with 100 stainless steel balls (16 mm diameter) in the bowl. The speed of the agitator was controlled with 75 revolutions per minute and 7 rotations per revolution to avoid bouncing of the ball. For the OPC paste (P0) with *w/b*=0.35, it was mixed for 1 min after the addition of all the deionized water. A rubber spatula was used to scrape the materials adhering on the wall and in the bottom to the middle. In the last step, the paste was mixed for another 2 min.

For the pastes with *w/b*=0.45, they were firstly mixed with the amount of water equal to *w/b*=0.35 for 1 min. Afterwards, the mixture was scraped with a rubber spatula as described above. The remained water was added, and the slurry was mixed for another 1 min. After a second scraping, the paste was mixed for the last 2 min. For the pastes with *w/b*=0.55, they were firstly mixed with the amount of water equal to *w/b*=0.35 for 1 min. After the first scraping, the water was added up to *w/b*=0.45. It was followed with 1 min mixing and the second scraping. Finally, the rest of water was added and mixed for 1 min. After the third scraping, the paste was mixed for 2 min. For the blended pastes, an extra 1 min premix of dry binder was performed before adding water. Afterwards, the blended pastes were mixed by following the same protocol as the OPC pastes.

2.3 Measurement procedures

2.3.1 Procedure for conductivity test

The electrical conductivity of paste was tested by four electrodes positioned in the Wenner configuration [31]. As shown in Figure 2.3, the stainless screws were used as the electrodes. They are positioned in the middle line with a parallel distance of 25 mm to the bottom. The Wenner space of electrodes is 40 mm. A brief circuit diagram of the setup is presented in Figure 2.3 The whole system was recorded and controlled by a datalogger. Two relays (a and b) were used to control the power supply and one relay (c) to control the data collection.

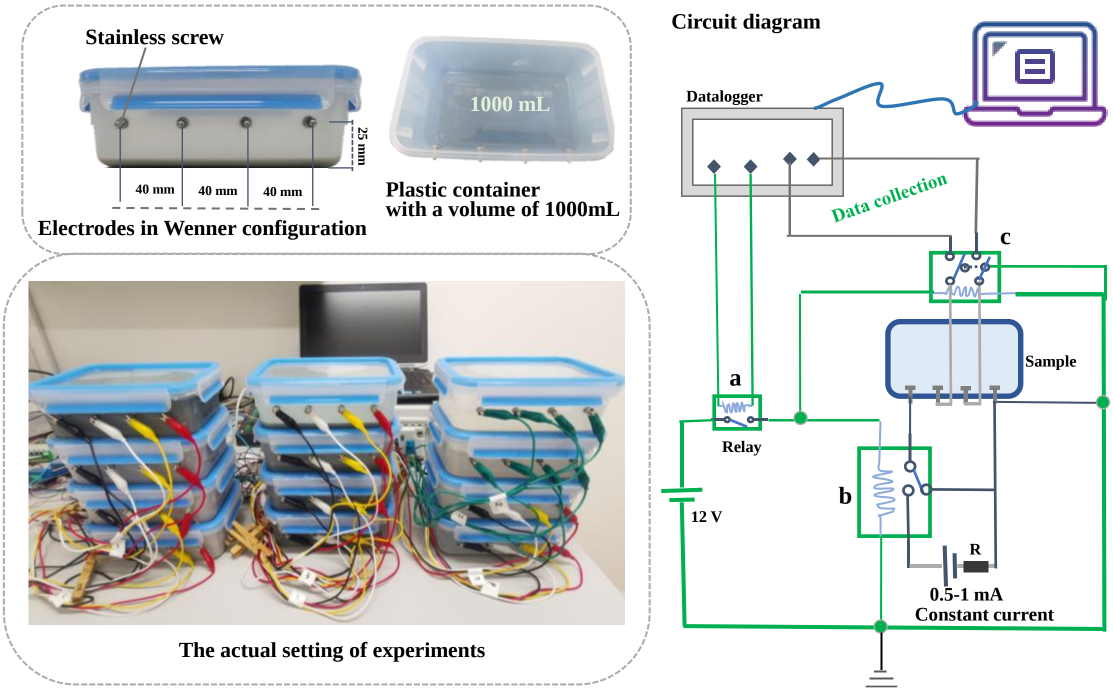

Figure 2.3. The setup for real-time conductivity measurement of pastes.

The datalogger released an instant signal every 2 min from water addition to 24 h to provide a constant current (0.5–1 mA) flowing through the outer two electrodes in each sample. Simultaneously, the relay "c" created the connection for detecting the voltage difference between the inner two electrodes in each sample. It takes about 0.2 seconds to finish one instant test. After 1 day the test time interval was switched to 10 min. Besides the time for an instant voltage test, the paired electrodes were connected to avoid polarization of electrodes. The electrical conductivity of the sample was calculated as a semi-infinite slab with the voltage and current value. The whole setup was calibrated with the standard conductive solutions (KCl) in the range of 0.015–74.97 mS/cm.

Figure 2.4 presents the calibration plot of the setup for in-situ conductivity measurement. Due to the limitation of the measuring range of the datalogger, two kinds of the impose current was set during the calibration process. Although the current is different, the measured conductivity in the 12 calibration points has a good correlation with the actual conductivity through a power function. The equation is $y=3.26x^{1.01}$ with a $R^2=0.9995$. All the measured conductivity data in this study were converted to the actual electrical conductivity by this calibrated equation.

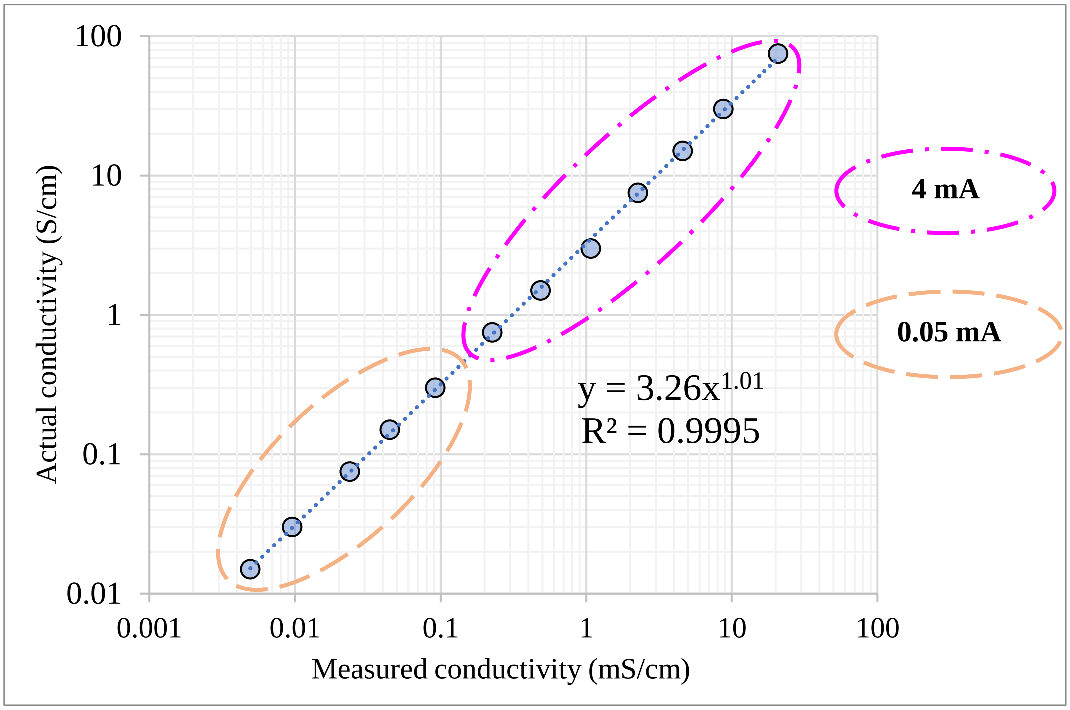

Figure 2.4. The calibration of the setup for conductivity test.

2.3.2 Procedure for testing water distribution in hcp

We designed an easily implementing procedure for determination of the evaporable and nonevaporable water content in pastes (see Figure 2.5). The pastes were mixed with the same procedure as in section 2.2.2. They were casted in a petri dish and cured in a sealed box with about 97% RH at 20 °C. The hcps were broken into pieces after a certain curing time. Particles with the selective size (D=1–2.5 mm) were collected for the treatment in the next step. To ensure the validity of data, the weight of particles should be ≥10 g, and the precision of analytical scale is at least 0.001 g.

The mass of dry empty crucible was weighed and recorded as m_0. The crucible filled with particles was weighed and recorded as m_1 and then particles were transferred into a small strainer with a hole size smaller than the particles. The mass of particles immersed in water was weighed (as m_v) by an analytical scale that was zero setting with the empty strainer. Thereafter, the particles were washed with isopropanol (IPA) before transferred back to the crucible. Samples were immersed with IPA with a liquid/solid ratio of 1.5 and sealed with cling film. The above procedure was finished within 30 min from sample crushing to the final sealing.

IPA exchange method is recommended as the preferred way for stopping the hydration and drying the paste [6], but this method also has an impact on the microstructure and chemical structure of hydration products. This effect is dependent on the sample size, exchange duration and IPA removal method. Zhang and Scherer [50] asserted that the exchange duration should be sufficient to reach ~99% IPA at the sample center. This exchange degree can be reached after 5-hour immersing for sample with the longest side of 1 mm. For a complete exchange of evaporable water, the immersing duration is at least 24 h for samples in this study (see Figure 2.5). We changed the solvent once at the middle immersing age.

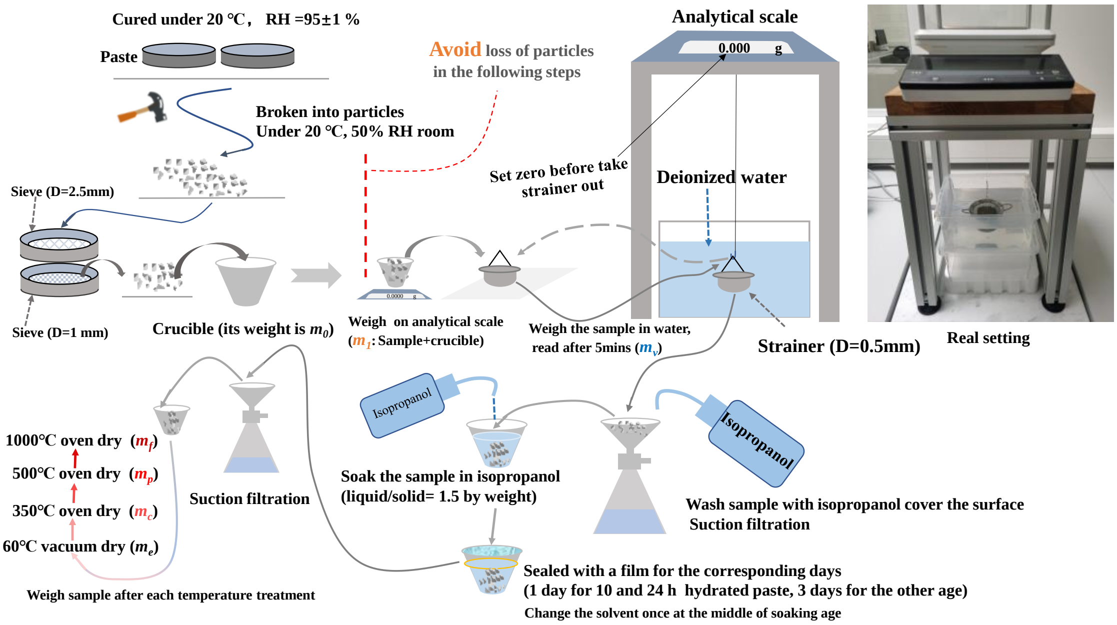

Figure 2.5. The invented procedure for the measurement of water distribution in hcp.

Samples were filtered, moved back to the crucible, and then followed with a vacuum drying at 60 °C (V60) for 24 h. After that, the mass of vacuum dried crucible with sample was weighed and recorded as m_e. The following step was that the crucible was immediately put into a furnace which was pre-heated to 105 °C. It was heated up to 350 °C with a rate of 5 °C/min and this temperature was maintained as constant for 2 h. After it was cooled down to 105 °C, we took it out with the heat-resistant gloves and weighed it on the analytical scale with an insulation layer between crucible and scale. The same step was repeated for the other temperatures, starting again at 105 °C to the target temperature (500 and 1000 °C, respectively) with a holding time of 2 h and weighing at the cooled temperature of 105 °C. The weight of crucible with sample at V60, 350, 500 and 1000 °C was recorded as m_c, m_p and m_f, respectively.

2.3.3 Procedure for moisture diffusivity test

The tubes were wet cut from the top by an electric diamond saw with a constant water flow. Firstly, a thin layer from the top (~3 mm) was cut to make an even sample surface. Afterwards, three discs with a thickness about 7 mm were cut for the vapor diffusion measurement (shown in Figure 2.6). The actual thickness and diameter of discs were measured at 4 different places to take an average value. The rest part of the sample was used for the semi-infinite drying measurement.

Both the discs and rest parts were conditioned under RH=97.6% for 14 days at 20 °C. A layer of moisture tight tape (double side, Stokvis VST397F1210) was adhered around the side of the discs before the discs were gently pressed in the tubes with the saturated salt solution for different RH control. The head and tail of the tape was connected without any gap in between or overlapping.

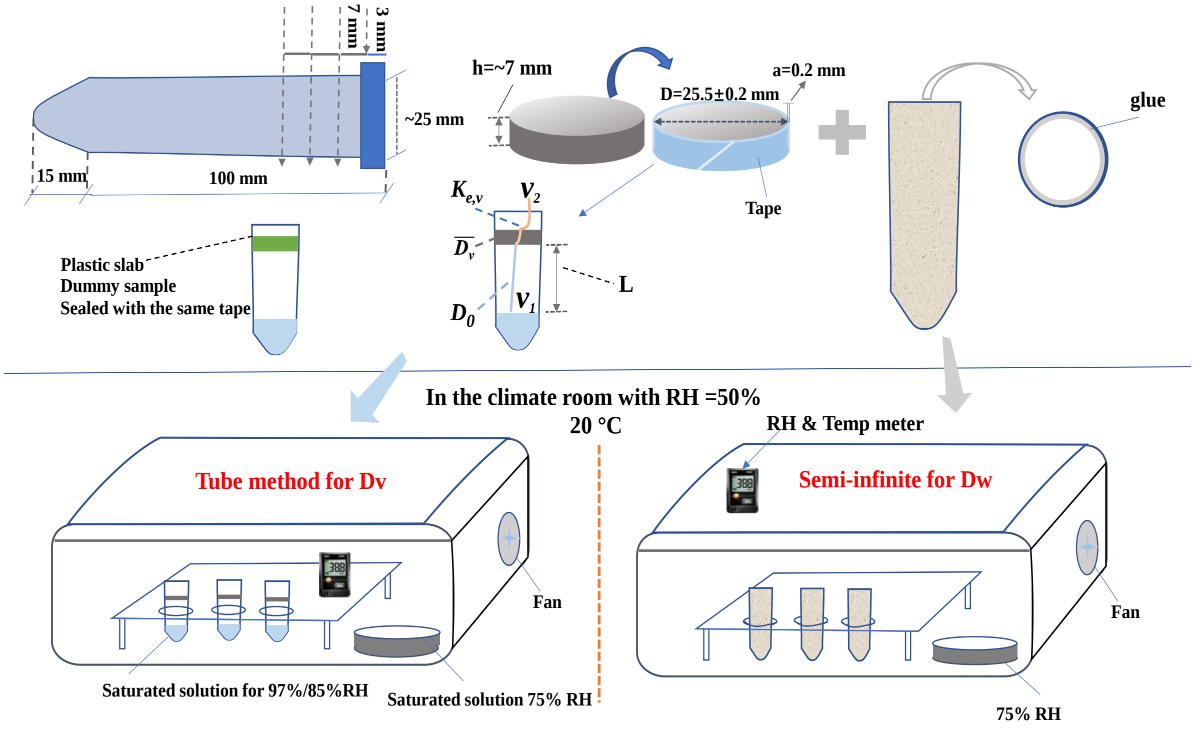

Figure 2.6. A sketch of the new method for measuring the moisture transport in the pastes.

We measure the distance between the surface of salt solution and disc (*L*) after it was mounted into the tube. RH in the tubes and conditioning boxes was controlled by different saturated salt solutions: NaCl (75.5%), KCl (85.1%) and K_2SO_4 (97.6%) at 20 °C [32]. Vapor diffusion in pastes was measured under 4 different RH intervals, 97.6–75.5% (RH97–75), 85.1–75.5% (RH85–75), 97.6–50% (RH97–50) and 75.5–50% (RH75–50). The semi-infinite drying tests were conducted under two different RH conditions (75.5% in the box and 50% in the climate room). To avoid any leakage from the edge of tubes, a thin circle of moisture tight glue (LOCTITE® 60 Seconds Universal glue) was applied around the edge. All the tubes were weighed at a series of conditioning times. We took 3 parallel measurements for each sample and some of original data is presented in Figure A1 and A2 (in Appendix).

2.3.4 Determination of evaporable and bound water

With the measured weights in section 2.3.2, we can calculate the weight loss at the corresponding temperature range, the evaporable water (Epw or epw as subscript) percent with respect to binder (φ_{epw}) is stated as:

$$\varphi_{epw} = \frac{m_1 - m_e}{m_{ub}} \tag{2.1}$$

where m_{ub} is the mass of dry binder, given that the carbonation of samples during early age can be neglected, the m_{ub} for paste without limestone can be calculated by Eq. 2.2.

$$m_{ub} = (m_f - m_0)/(1 - LOI_b) \tag{2.2}$$

The weight loss at the temperature range of V60–350 °C, 350–500 °C and 500–1000 °C can be determined by Eq. 2.3, 2.4 and 2.5, respectively.

$$\varphi_{\sim 350} = \frac{m_e - m_c}{m_{ub}} \tag{2.3}$$

$$\varphi_{350\text{–}500} = \frac{m_c - m_p}{m_{ub}} \tag{2.4}$$

$$\varphi_{500\text{–}1000} = \frac{m_p - m_f}{m_{ub}} - LOI_b \tag{2.5}$$

For limestone blended paste, tCO_2 from limestone needs to be subtracted within the temperature range 500–1000 °C. Hence, the actual weight of binder is m_{ub}' by Eq. 2.6.

$$m_{ub}' = (m_f - m_0)/(1 - 44\% \times P_{lm} - LOI_b) \tag{2.6}$$

where P_{lm} is the replacement percentage of limestone, and it is 16% in this study. In addition, the weight loss from nonevaporable water between 500 and 1000 °C for limestone blended is:

$$\varphi_{500\text{–}1000} = \frac{m_p - m_f}{m_{ub}'} - 44\% \times P_{lm} - LOI_b \tag{2.7}$$

Theoretically, according to the law of conservation of mass, we can get the mass balance in Eq. 2.8. This will help to check the accuracy of the water test procedure.

$$\varphi_{epw} + \varphi_{\sim 350} + \varphi_{350\text{–}500} + \varphi_{500\text{–}1000} \equiv w/b \tag{2.8}$$

2.4 Methods

2.4.1 X-ray diffraction

The XRD of the hydration products was determined by a Rigaku International Corporation D/max 2550 VB3+/PC diffractometer (Cu Kα radiation). The measurements were conducted in the range of 5–45° (2θ) with a step of 0.05°, a counting time of 1 s/step, a tube voltage of 40 kV and a current of 100 mA.

2.4.2 Scanning electron microscopy

The Au-plated particles were detected by a Nova NanoSEM 450 scanning electron microscope. The accelerating voltage and beam current for the images were 10 kV and 0.5 nA, respectively.

2.4.3 Isothermal calorimeter

The hydration heat release was tested by the TAM Air Isothermal Calorimeter from TA Instruments (TAM air C80, Thermometric, Sweden). The sample was only stirred within the initials 30 s and then measure in quiescence.

2.4.4 Moisture content

The pastes were also crashed into particles (<2 mm) and then conditioned in the box with different RHs (97.6%, 75.5% and 50%, respectively). Calcium hydroxide was put in the RH box as a sacrifice to absorb CO_2. After 1-year conditioning, the particles were used to measure the evaporable water content by vacuum drying at 60 °C for 3 days.

2.4.5 Rapid chloride migration

Pastes were mixed by following the same protocols described in section 2.2.2 and then casted into a rubber cylinder mould (D_{inside}=50 mm, h=110 mm). After the sealed curing for 1 day, specimens were demoulded and moist cured until the age of 28 days and 90 days, respectively. At the specified age, two samples with a thickness of 50 mm were cut from each specimen for the RCM test. The test was performed according to NT BUILD 492 but without the vacuum saturation procedure owing to the fact that the specimens were moist cured before the test.

2.4.6 MIP measurement

After crushing, the pieces with size 3–8 mm were selected by sieving. Then the hydration was stopped by immersing the pieces into isopropanol for 3 days, which duration is appropriate for a full solvent exchange [33]. The pieces were then dried with a continuous pumping under vacuum at 40 °C for 3 days. The pore size was measured by a MicroActive AutoPore V 9600 Version 2.03 machine. The pressure was initiated at 0.003 Pa and increased up to 250 MPa, and this allows intrusion of pore entries from initially 373 μm down to about 6 nm (contact angle 138°).

3 Hydration of C_3S in solutions at early age

This chapter will focus on how the interfacial nucleation of C-S-H occurs. The size of etch pits on C_3S surface was counted to verify the dissolution theory. A new hypothesis is proposed to provide a holistic explanation for the hydration process from water contact to the end of the induction period in the discussion section. This hypothesis also reveals the mechanism of the bottom-up structure building process during the early hydration. The hydration heat evolution was monitored by an isothermal calorimetry test. The composition and morphology of hydration products were determined by X-ray diffraction (XRD) and scanning electron microscopy (SEM).

3.1 Theories for the early hydration

During the past decades, there were many investigations on revealing the hydration mechanism of cement. Although so many efforts were paid to this topic, some problems remain unsolved or under argument even for the hydration of minerals. Because C_3S is the main constituent of ordinary Portland cement, a better understanding of its hydration is a critical step to unveil the mechanism of the cement hydration. A majority of the previous studies classified C_3S hydration into 5 regions as in [34]. Scrivener et al. [35] simplified this into 3 periods: I- up to the end of the induction period (IP); II- the main hydration peak; and III- hydration after the main peak. Whether the reaction in period I is controlled by the formation of a protective layer covering the surface [36] or only the dissolution rate [37] is still hotly debated. The duration of period I and the reaction rate at this period would be affected by many factors, including intrinsic properties and external factors (inorganic salts, organic compounds and temperature).

The two most popular theories for explaining the rapid decrease in heat release during IP are the protective membrane and the dissolution controlled by undersaturation. These theories are well summarized and distinguished in [35]. The dissolution theory may be better for explaining the emerge of the IP than the protective membrane, but it seems to be inapplicable for explaining the retarding effect of organic admixtures by only considering the relationship between dissolution rate and thermodynamic properties of bulk pore solution. This theory tries to explain the retarding effect by the reason that the ions or molecules adsorbed on the particle surface passivate the active sites and block the dissolution of defects, like dislocations outcropping on the surface, or point defects [37,38].

However, the dissolution rate is increased by some organic retarders [11]. Moreover, it is doubtful that the longer IP of the annealed C_3S can be explained by the dissolution theory because the surface defects may have little effect on the dissolution rate of minerals. Therefore, it is more reasonable to ascribe the long duration of the IP to the inhibition of the nucleation and growth of hydration products (Portlandite or C-S-H) induced by the admixtures [39–42]. This inhibiting effect will delay the starting time of the acceleration period to increase the IP. The underlying relation between the nucleation process or dissolution process with the hydration heat release is about how the initial structure builds at the early age, and this is the basic structure of the hydration products.

3.2 Hydration of C_3S with KOH and K_2SO_4 solution

Alkali salts have large influences on the hydration of C_3S during IP as well as the morphology of hydration products in acceleration period. Figure 3.1 presents the hydration heat flow of C_3S with deionized water, KH and KS, respectively. The measured results are also compared with the data in published paper. Herein, to distinguish the start and end of IP, we define the IP as a time interval during which the first derivative of the heat flow is between -0.5 mW/(g·h) and 0.5 mW/(g·h).

The analysis focuses on the hydration period from the starting point to the end of the IP (from 0 to 2.5 h). A temperature of 25 °C brings an earlier starting point for samples with deionized water or KS compared with 20 °C. The IP ends up earlier in the hydration of samples at a higher temperature. This effect is so evident for samples with KH and KS, decreasing from 1.75 to 0.50 h and 2.28 to 1.15 h, respectively. K_2SO_4 has a great increasing effect on the main peak that is even larger than that effect of KOH, but its duration of IP is still longer than the sample with KOH. This effect is similar to the influence from sodium salts in the previous research [43].

The differences in the effect from KOH and K_2SO_4 may relate to the nucleation and growth of hydration products. This requires a focus on the early precipitated phases. Figure 3.2 shows the surface of C_3S hydrated in deionized water. It should be noted that the surface was treated with isopropanol, so the nature of the original surface is different from what is detected in the image. There is no distinguishable dissolution pit on the surface. However, many strips can be observed and they were called needles in other published studies [43–45]. The enlarged image presents a clearer feature for the strips, and it shows that the strips consist of many globule flocs. According to Jenning's model [22], these globule flocs with a size about 50 nm are built by the packing of globules with a smaller size of 4–10 nm. It shows that the mean diameter of the globule flocs is about 63 nm in deionized water from the Gaussian distribution in the counted flocs.

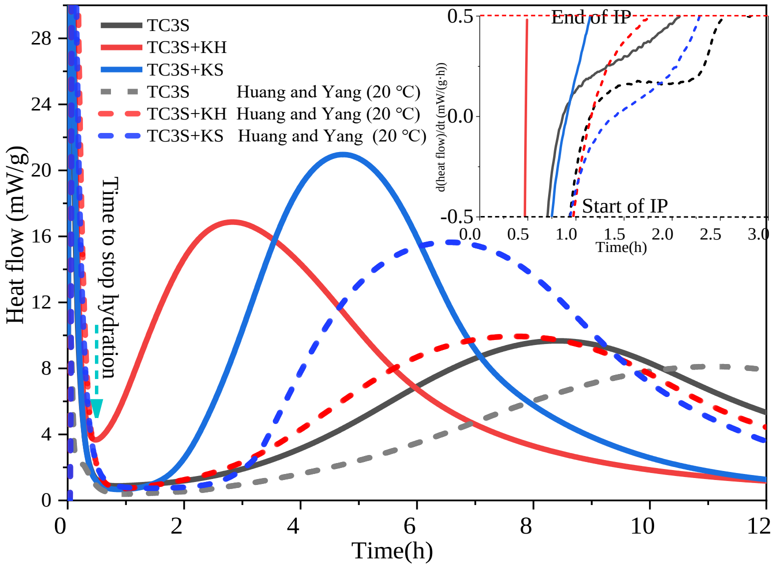

Figure 3.1. Hydration heat flow of TC_3S with deionized water, KH and KS. The solid line is hydration data with a w/c = 0.5 at 25 °C [11], and the dash line is hydration data with a w/c = 2 at 20 °C, adopting from [10].

The strips on the surface of C_3S in the KH (Figure 3.3a) is much thinner than those in the deionized water (Figure 3.2), and many strips even pack together to form a dense cluster. The previous research paid attention to the needle length without considering the thickness of the needles, which represents the diameter of the primary globule size. The mean thickness of the strips in KH is about 18 nm. Whereas the strips in KS have a thickness about 49 nm, and this size is much larger than the products in the KH. Moreover, portlandite on the surface is well nucleated in large crystal with some sizes larger than 500 nm. The correlations between the duration of IP and the size of globule floc will be further analyzed in the discussion section.

The morphology of globule floc indicates that the precipitation of C-S-H is a nonclassical nucleation process. C-S-H precipitates through the crystallization by particle attachment (CPA), which means a crystallization process by the addition of particles, ranging from multi-ion complexes to the fully formed nanocrystals [46]. The classical theory for nucleation process is crystallization through monomer by monomer addition [47]. As summarized in [46], particle attachment is influenced by the structure of the solvent and ions at solid-solution interfaces and in confined regions of the solution between solid surfaces. This is the actual reaction that happens during the hydration of C_3S. It also has been proven in the nucleation of many other minerals, such as gypsum [48], iron oxyhydroxide nanoparticles [49], $CaCO_3$ [50], and silicates [51].

It shows that nucleation of C-S-H in the IP firstly comes with a formation of the primary globule flocs (Figure 3.2), which may be formed from polymerization of mono silicic complexes into dimeric structures [52]. This happens within a confined region between the surface and solution, due to a higher concentration of ions or complexes in this local region compared with the bulk solutions. The dissolution equilibrium may build up within the interfacial regions instead of between the solid and bulk pore solution. Some correlations may exist between the thermodynamics of the interfacial region and bulk solution, but it is ambiguous to connect the hydration kinetic in the IP directly with the ion concentration in the bulk pore solution when the correlation is not clearly revealed.

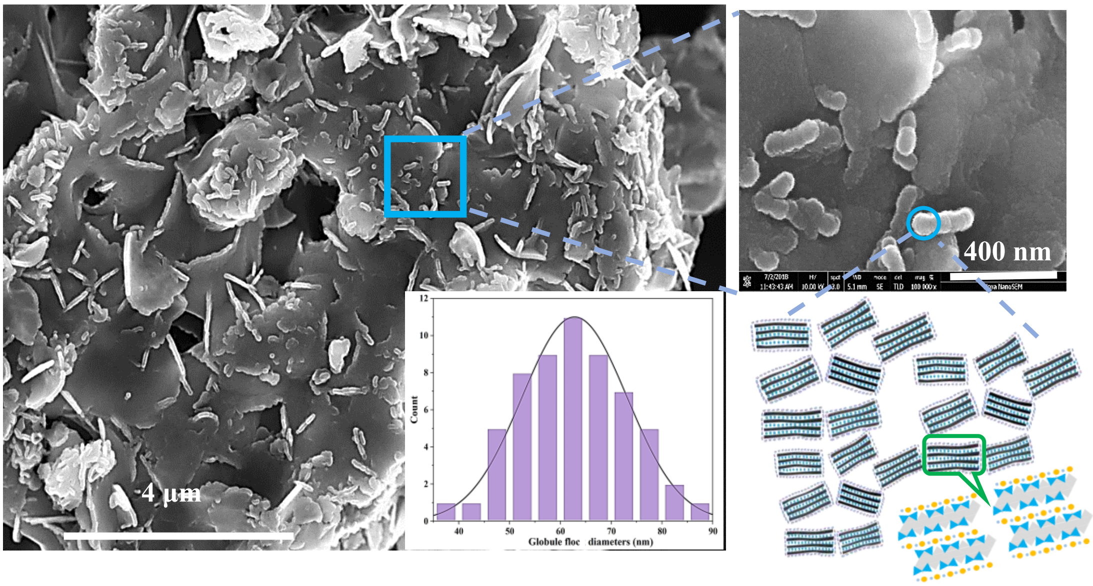

Figure 3.2. SEM image of TC_3S hydrated with deionized water. The hydration was stopped at 0.5 h after water addition by isopropanol exchange. An enlarged image was provided to give a clearer picture of the particles on the surface. The diameter of the globule flocs was counted with the Nano measurer software. The structure of the globule flocs was illustrated based on Jennings model, refer to [11] for high resolution figure.

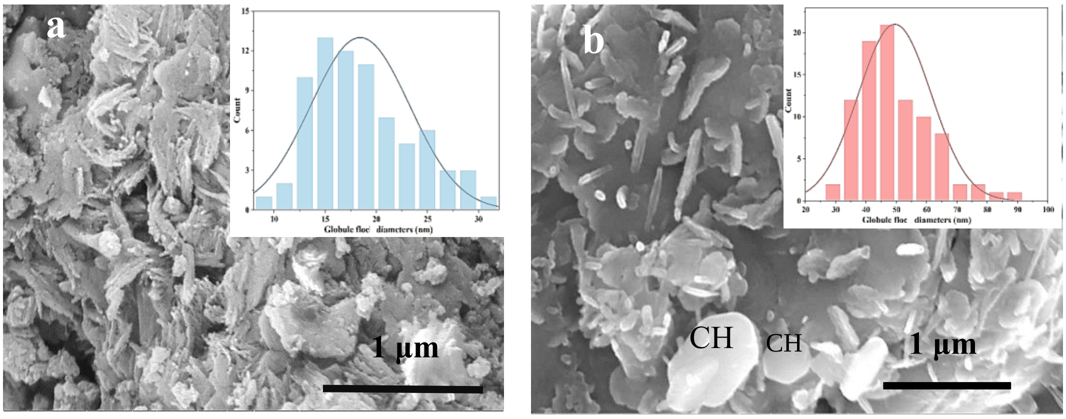

Figure 3.3. SEM images of TC_3S hydrated in KOH (a) and K_2SO_4 (b) solutions, respectively. The hydration was stopped at 0.5 h after water addition by isopropanol exchange.

3.3 Hydration of C_3S mixed with C_3A

The hydration of cement is a much more complex process than the hydration of C_3S due to the involving of other minerals. Calcium aluminates affect the hydration of process of C_3S as well as the structure of C-S-H. Figure 3.4 presents the SEM images of C_3S hydrated with deionized water. The hydration was stopped at 4 h by freeze-drying, which is different from the treatment of samples in Figure 3.2 and 3.3. The pristine feature of the surface is better preserved by freeze-drying than IPA exchange, as many etch pits can be observed on the surface of the particles. The mean diameter (width) of the etch pits is about 24 nm by counting 38 sites. The length of C-S-H strips is about 117 nm from Gaussian distribution.

The image (Figure 3.4II) with a higher magnification presents a clear feature of the particle surface. It offers the evidence for the nucleation of a primary mono floc (0), formation of a dimer floc (1), a single strip from the nearly oriented attachment (2), and the clusters from a strip attachment (3) or the single particle attaching to strips. The findings further confirm that the precipitation of C-S-H initiates with the nucleation of the primary mono flocs: the poorly crystalline nanoparticles or colloidal, which is similar to the crystallization process of some other polymers or minerals [46,53]. The mono floc seems to be the intermediate C-S-H phase during the precipitation process as highlighted in some previous investigations [54,55]. Due to its metastable state, the globule flocs will aggregate into strips by the oriented attachment in the local region. With the increasing nucleation of mono floc and strips, the mono floc can also attach to the strip. Meanwhile, the strips may attach to each other to form a more stable cluster.

A linear grey level distribution in Figure 3.4a–e indicates that there is a special layer between the undissolved surface and precipitated C-S-H. Ca accumulates in the etch pit according to some experimental research in the dissolution of β-C_2S [56]. This phenomenon may also happen during hydration of C_3S, so the layer would be portlandite that precipitates from the Ca ions absorbed on the colloidal surface in solution. In SEM images, the thickness of this layer is approximately 8–11 nm. Provided that both the surface of dissolved C_3S and nucleated C-S-H are colloidal structure, the stable distance between these two colloids is about 8–14 nm under the condition when the colloids have a charged surface (10–100 mV) in a solution with ion concentration in a range of 10–100 mmol/L [57]. Because there is no stirring of the paste after the initial mixing, the layer probably precipitates from a quick accumulation of Ca ions between two colloidal surfaces during the sudden freeze-drying. Figure 3.5 demonstrates the surface of C_3S hydrating with the presence of C_3A. We can detect the etch pits the surface as well. The mean size of the etch pits is about 28 nm, and this is a little larger than the size of etch pit in the pure C_3S with deionized water (see Figure 3.2).

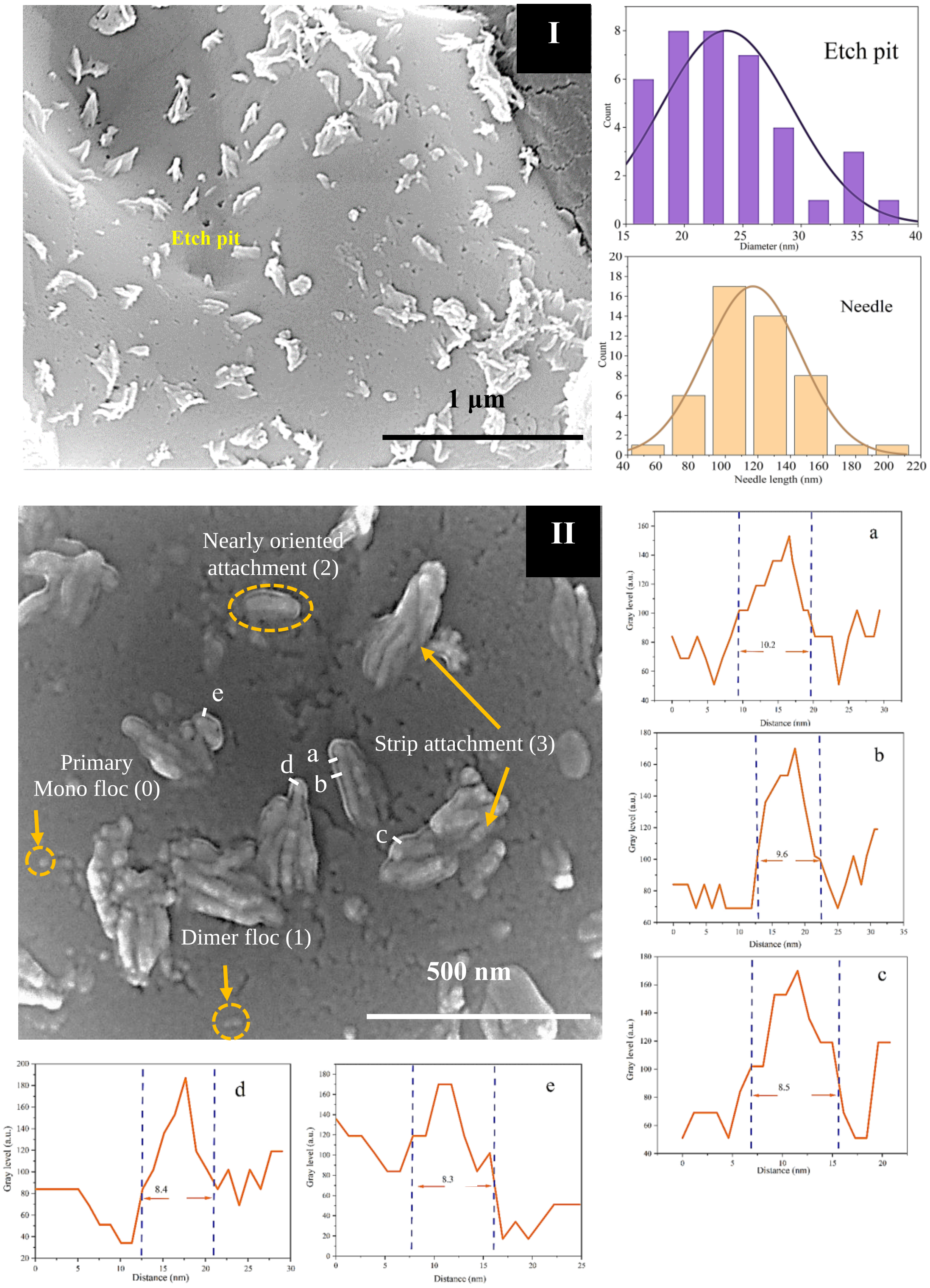

Figure 3.4. SEM images of TC_3S hydrated in deionized water. The hydration was stopped at 4 h after water addition by freeze-drying. An image with a higher magnification was provided to give a clear picture of the particles on the surface (II). Nucleation of primary mono-flocs and dimer flocs were detected above or near the etch pit. C-S-H grows by nearly oriented attachment and block attachment. A layer of portlandite with a thickness of approximately 8–11 nm was detected between the undissolved surface and globule.

According to the dissolution theory based on the saturation state of the bulk solution [58], the low reaction plateau (low heat release in Figure 3.1 before 4 h) is controlled by the step retreat. However, the presence of etch pits in both Figure 3.2 and Figure 3.5a implies that the reaction in this period is indeed controlled by the etch pit opening. The transition occurs from the step retreat to dislocation control (etch pit opening) during the IP. To compare the dissolution rate of C_3S and C_3S with C_3A, we performed a further analysis based on the dissolution rate determining equation in [58].

$$|R_d| = \frac{A_1(1-SI)|\ln(SI)|}{1+A_2|\ln(SI)|} \tag{3.1}$$

$$SI = \frac{Q}{K_{SP}} \tag{3.2}$$

where A_1 and A_2 are constants in the situation with the same minerals. R_d is the dissolution rate controlled by the etch pit opening. SI is the saturation index, Q is the ion product, and K_{sp} is the ion-product equilibrium constant. It can be concluded that the dissolution rate of C_3S particles with similar distribution of etch pit only relates to the saturation index of the solution referring to Eq. 3.2. Nonetheless, the data from the previous articles [59,60] showed that there was no significant difference in the main ions concentration in the squeezed pore solution from C_3S with and without C_3A in IP.

The big difference in heat flow at the end of IP can hardly be explained by the different dissolution rate of C_3S. However, the nucleation and growth rate of the hydration products on the particle surface gives a reasonable explanation for the much lower heat release rate. It shows that the needle length of C-S-H in the mixture system is about 94 nm (see Figure 3.5a2), which is much shorter than it is in pure C_3S (116 nm). The diameter of the globule flocs in C_3S with C_3A is even smaller than that in pure C_3S. Al ions in the solution induce the nucleation of the primary globule in a smaller size, but it suppresses the growth of strips from the attachment of primary particles. KH and KS can eliminate the inhibiting effect from Al ions. The growth of C-S-H in KH and KS was much faster than it in the deionized water, so the surface was covered by the hydration products as shown in Figure 3.5b and c. Figure 3.5d presents that KH and KS can decease the globule floc size to about 20 nm. It is interesting that the presence of C_3A almost erases the differences in the effects from KH and KS on the flocs size. With this observation, it is obvious that the long duration of IP from C_3S with KS (Figure 3.1) is due to the nucleation of larger primary globule compared with KH. C_3A can weaken the effect from KS on the nucleation of globule flocs, so that it reduces the duration of IP of mixture system in KS compared to the pure C_3S.

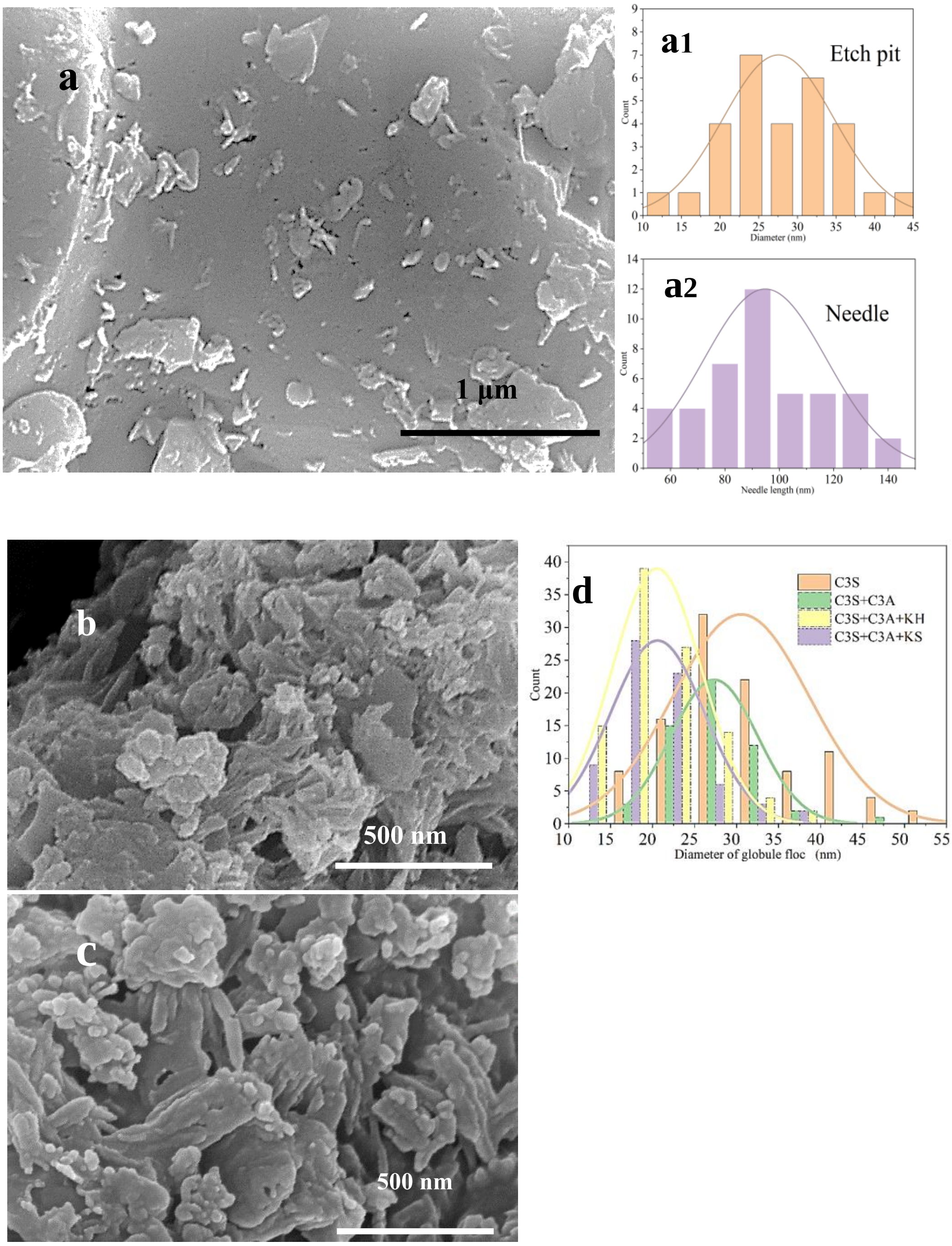

Figure 3.5. SEM images of TC_3S hydrated with deionized water (a), KOH solution (b), and K_2SO_4 solution (c) in the presence of C_3A. The hydration was stopped at 4 h after water addition by freeze-drying. The diameter of the etch pit (a1) and needle length (a2) were counted for samples in deionized water. The diameter of the globule floc is summarized in d.

3.4 Discussion

3.4.1 Correlation between the duration of IP and size of globule flocs

The size of the primary C-S-H globule flocs correlates to the duration of IP as mentioned in the previous section. The globule in solution will agglomerate into globule flocs with a colloidal structure. The initial nucleation of the globule floc can be considered a classical nucleation process, so the surface nucleation rate is given by [61–63]:

$$J = J_n e^{-\Delta G_{crit}/\mathrm{k}T} \tag{3.3}$$

where J is the steady-state surface nucleation rate (number of nucleation events per surface area per second), ΔG_{crit} denotes the thermodynamic barrier to form a molecular cluster with the critical size, and k represents the Boltzmann constant. J_n is a pre-exponential factor that can be considered a kinetic constant. The thermodynamic barrier is given with Eq. 3.4 by assuming the spherical nucleus:

$$\Delta G_{crit} = \frac{4\pi\gamma_{sl}r_{crit}^2}{3} \tag{3.4}$$

where γ_{sl} denotes the surface energy and r_{crit} is the critical radius of the nuclei. A certain number of nuclei should be formed to reach the sufficient probability for attachment between the primary nuclei. We can assume that the required density of nuclei for C-S-H growth by attachment is n during the hydration of C_3S. The duration of nucleation at IP then can be expressed as:

$$t_{ind} = \frac{n}{J} = \frac{n}{J_n} e^{\frac{\Delta G_{crit}}{kT}} \tag{3.5}$$

A combination of Eq. 3.4 and 3.5 can obtain Eq. 3.6,

$$ln t_{ind} = ln\frac{n}{J_n} + \frac{\Delta G_{crit}}{kT} = A + \frac{4\pi\gamma_{sl}r_{crit}^2}{3kT} \tag{3.6}$$

Figure 3.6 shows the curve fitting between the duration of IP from hydration heat flow and the radius of globule flocs from the counting in the SEM images. The duration of IP has a good correlation with the globule size, especially in pure C_3S hydration stopped at 30 min with solvent exchange. The size of flocs in the hydration products stopped by freeze-drying is much smaller than the products from solvent exchange, so the slope of the two fitted lines are significantly different. The triangle for pure C_3S deviates from the sample with C_3A, which implies the presence of Al will affect the kinetic of C-S-H nucleation.

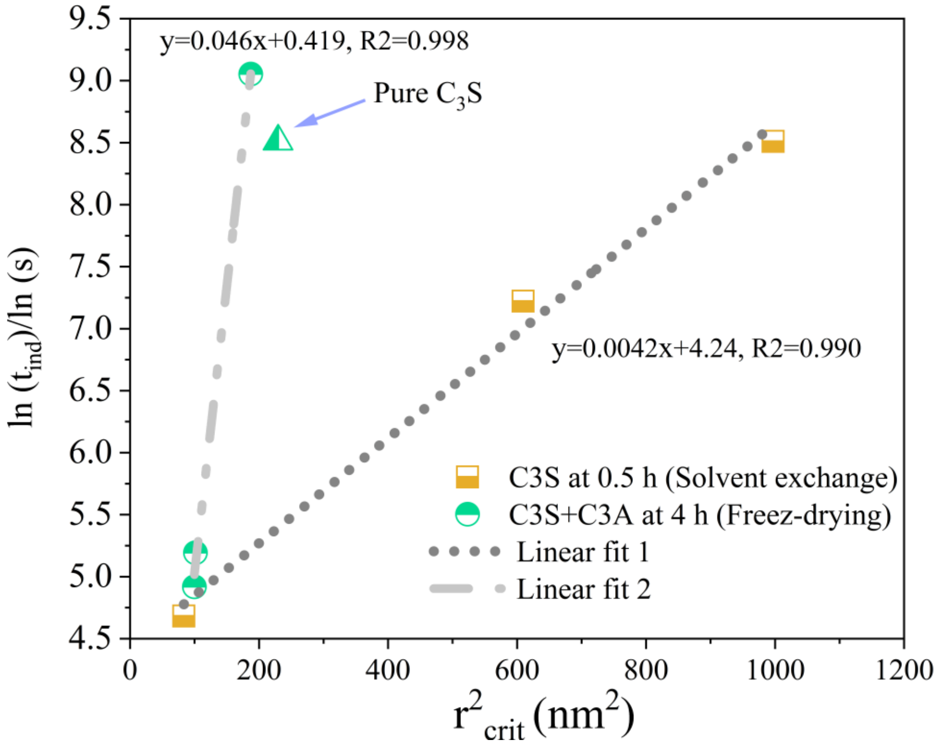

Figure 3.6. The linear fitting data between ln (t_{ind}) and r_{crit}^2 based on Eq. 3.6.

3.4.2 The hypothesis for early hydration

The precipitation of C-S-H during the early structure building process can be classified into 5 stages as shown in the Figure 3.7.

Stage I: Fast dissolution. This process is the initial stage after minerals contact with water. There is a high superficial undersaturation state for the dissolution of C_3S, so it has an ultra-fast dissolution rate. As the quick initial dissolution proceeds, the increased pH and ion species in the solution increase the reverse reaction of the dissolution process. This brings forth the Stage II: Approaching dissolution equilibrium. Under this condition, the thermodynamic state in the near surface region determines the actual reaction rate. After a certain degree of dissolution, the near region comes to an equilibrium state with respect to dissolution of C_3S under static condition (without strong stirring). In the meantime, the high local concentration of Si and Ca ions will create an oversaturated state with respect to precipitation of primary C-S-H globules or CH, so it comes to the Stage III: New surface equilibrium.

Stage IV: Surface nucleation. The primary C-S-H globules start to nucleate on the surface. The chemical structure of the globules could be with a Ca/Si ratio of 1.5, 2.0 [64], or even higher value because the deprotonated silanol needs cations to neutralize the charge. The globule in solution will agglomerate into globule flocs with a colloidal structure as illustrated in Figure 3.7. Stage V: Attachment to growth. This stage is dominated by growth of C-S-H through particle attachment, and the attachment of C-S-H is a colloidal assembly process similar to the other minerals. The attachment may happen on a selective orientation when there are alkali salts in the solution, so the morphology of C-S-H strip can be altered. The precipitation greatly consumes the Si and Ca ion species in the local region to reduce the near surface saturation state.

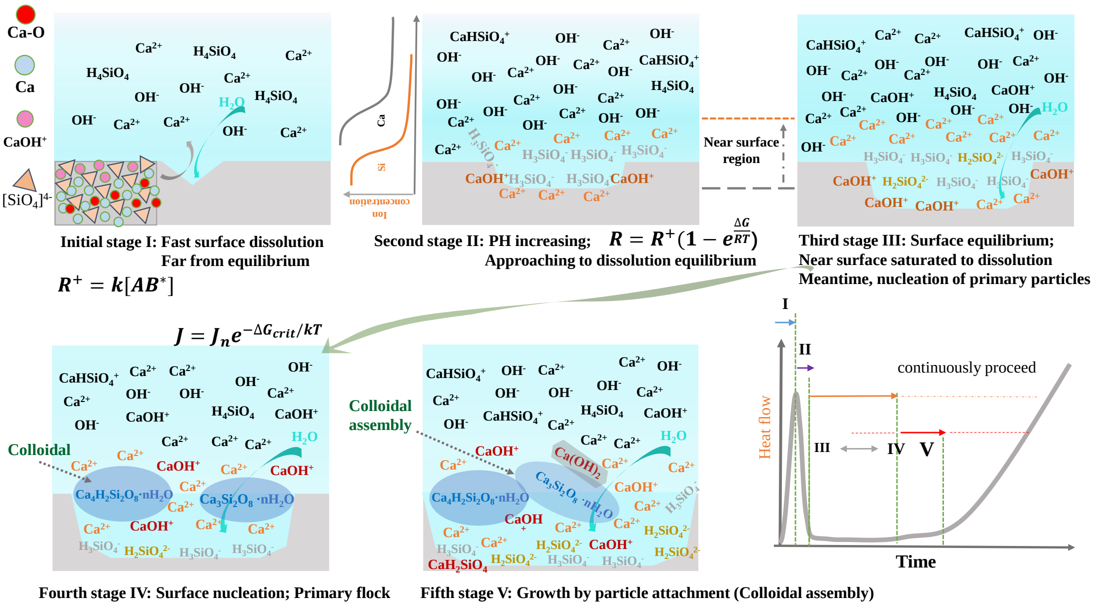

Initial stage I: Fast surface dissolution
Far from equilibrium

$R^+ = k[AB^*]$

Second stage II: PH increasing; $R = R^+(1 - e^{\frac{\Delta G}{RT}})$
Approaching to dissolution equilibrium

Third stage III: Surface equilibrium;
Near surface saturated to dissolution
Meantime, nucleation of primary particles

$J = J_n e^{-\Delta G_{crit}/kT}$

Fourth stage IV: Surface nucleation; Primary flock

Fifth stage V: Growth by particle attachment (Colloidal assembly)

Figure 3.7. Illustration of the hypothesis for hydration of C_3S up to the end of the low-rate period. The ion species in black are ions far from the double layer with high mobility (that can be detected by filtering) and other colored notations of ions represent the surface absorbed species (hard to be detected in the pore solution) [11].

3.5 Summary

The initial structure building at early age is a nonclassical nucleation process of C-S-H. It starts with nucleation of primary flocs and then followed by the growth from particle attachment. The attachment of C-S-H globule floc is a colloidal assembly process, which will be influence by the presence of Al ions, sulfate ions and alkali metal ions. A layer between the C-S-H flocs and C_3S surface would probably be the precipitation of CH between the two colloidal surfaces.

The decrease in the heat release rate at the start of IP is due to the slow nucleation rate of C-S-H instead of dissolution of the etch pit. KOH and K_2SO_4 have an impact on the size of primary flocs and growth of C-S-H strip, so that they change the duration of IP and the structure of hcp after long-term hydration. Al ion inhibits the dissolution of C_3S at a very early age before the start of IP, and it also suppresses the growth of C-S-H to increase the duration of IP.

Based on the dissolution and CPA theory, we proposed a five-stage hypothesis for the early hydration process by focusing on the nucleation and growth of C-S-H, that is: Stage I, Fast dissolution; Stage II, Approaching dissolution equilibrium; Stage III, New surface equilibrium; Stage IV, Surface nucleation, and Stage V, Attachment to growth.

4 Monitoring the hydration and structure evolution of pastes with electrical conductivity

This chapter presents the study results from the instantaneous conductivity monitoring by use of a simple setup. It mainly sheds light on the deep understanding of how electrical conductivity of paste relates to the hydration reaction and structure growth. The conductivity of pore solution was evaluated according to the chemical composition of binders and the content of evaporable water. Formation factor (*F*) of pastes was calculated to distinguish the effect from the pore solution and structure on the electrical conductivity. Its growth rate at different hydration time was discussed in detail by combining with chemical reaction. A good correlation has been found between the *F* and moisture content based on an extended percolation theory.

4.1 Introduction

The test of electrical conductivity was widely used as the qualitive way to indicate the hydration and structure of cement-based materials in the previous studies [65–69]. Because the conductivity in pastes is sensitive to many factors, it is really challenging to find a good quantitative correlation between the conductivity and hydration degree or other properties of cement-based materials. The electric current can be conducted through two components in hcp: one is ionic conductivity through pore solution, which depends on the temperature [64–66], type of ions and their concentration [73,74]; the other is electronic conduction through the gel, gel-water and unreacted cement particles, particularly compounds of iron and aluminum [75].

Some empirical functions were proposed to correlate the electrical properties in hcp with the hydration time, porosity, hydration degree [76], mechanical performance (compressive strength [77,78]) or ion diffusivity [79,80]. The conductivity evolution of paste during hydration will be determined by the change of intrinsic properties as shown in Figure 4.1. The reaction of minerals with water induces the change of phase assemblage and moisture content. In the meantime, it builds the early structure of hcp. The reduction in the availability of liquid water in paste, in turn, determines the rate and degree of later age hydration. The volume of pore solution and ionic concentration are related to the phase assemblage and moisture content through thermodynamic properties. The connectivity of pore solution (pore connectivity) is the other factor that controls the conductivity of paste. The mechanical performance and durability of paste are intrinsically determined by its phase assemblage, pore structure and saturation state. These properties can be qualitatively or empirically indicated by electrical properties, but there is no general description at present. It is of great significance to find a quantitative relation between the conductivity and structure properties in hcp during hydration process.

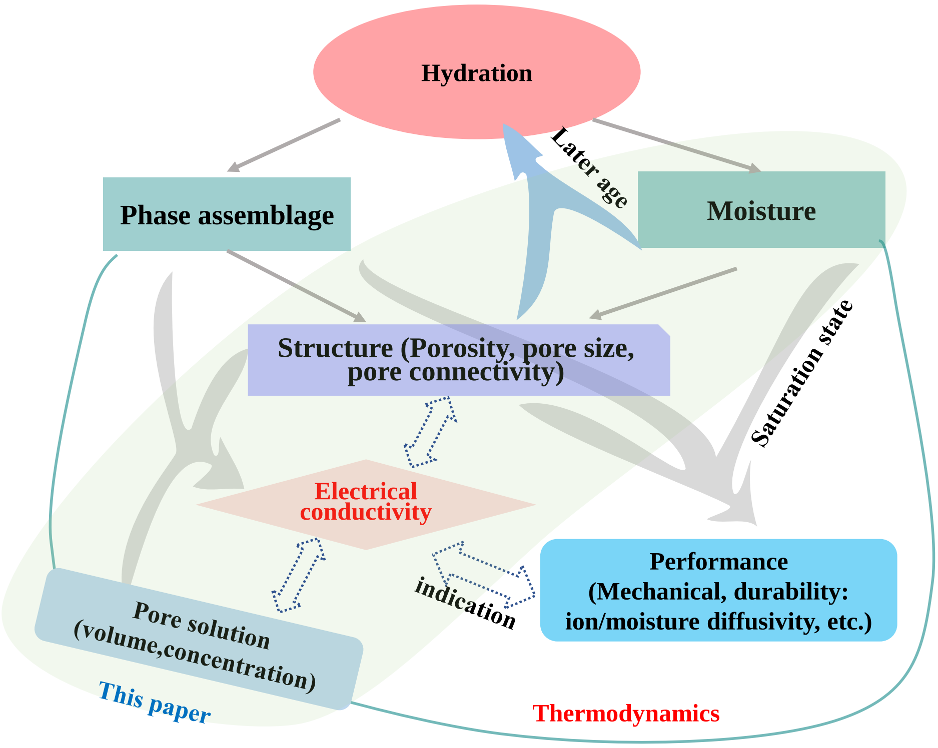

Figure 4.1. The relationship between the conductivity, hydration evolution and performance of hcp.

4.2 Real-time electrical conductivity of pastes

Figure 4.2 illustrates the measured conductivity of hydrating pastes. It shows that the evolution of it can be classified into four stages. A similar trend was found in conductivity development during hydration by other measurement methods [15,17,21]. In the first stage (Stage I), The conductivity shows a rapid increase after the start point at about 12 min and the value are very large at this initial point. This is mainly due to a quick dissolution of alkali metal ions and high reactive minerals (C_3A and C_3S). The fast dissolution brings a high alkali concentration with OH^-, K^+ or Na^+ in pore solution, whose actual concentration depends on the alkali content in the binders [22,44,45], leading to a high electrical conductivity of pore solution.

The second stage (Stage II) corresponds to the induction period in the heat release test. Ca concentration keeps almost constant and even has a little reduction, but Si concentration increases during this period. It has little influence on the conductivity of pore solution. *w/b* has few effects on the duration of this period, and this is consistent with calorimetry test that *w/b* had few effects on the heat release rate before 4 h [47]. The blending of fly ash, slag and limestone prolongs the transition time from stage II to III.

The growth of hydration products in the Stage III builds the rigid connection between the unhydrated particles. Although the main conductive ions (OH^-, Na^+ and K^+) have increased at the corresponding period [22,45], the conductivity of paste reduces due to decrease in the connectivity of pore solution caused by the structure growth. The higher *w/b* induces a longer stage III, and this influence is more apparent for the blended system.

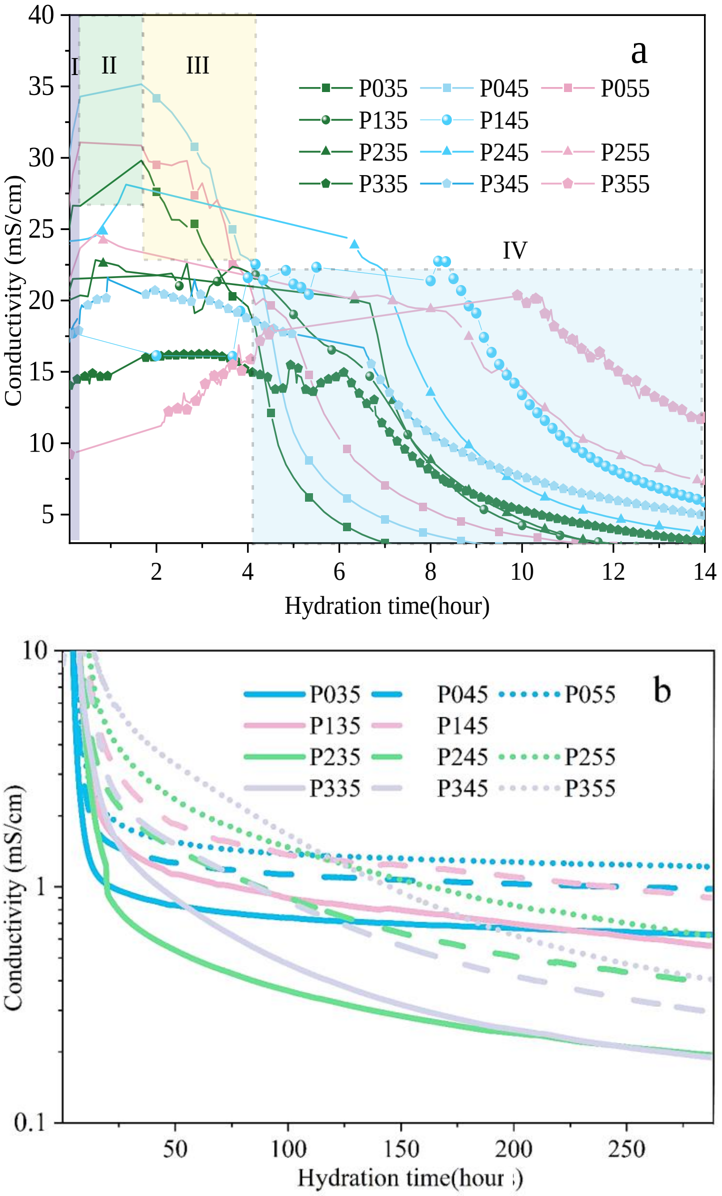

Figure 4.2. Electrical conductivity evolution of pastes during hydration: (a) detail data before 14 h; (b) data to 288 h (12 days).

The rapid growth of hydration products brings forth the stage IV. A further growth of hydration products mainly leads to the filling and blocking of pores in the rigid structure. Meanwhile, the consumption of free water reduces the volume of pore solution. These dual effects cause the tremendous decline in conductivity. *w/b* has no effects on the decreasing rate of conductivity in this stage. However, SCMs have impact on this rate as shown in Figure 4.2. Electrical conductivity of OPC paste falls into a rather stable stage after about 1 day where it has a slow decreasing rate. A similar time duration for rapid descend in conductivity is detected for OPC pastes with different *w/b*, but the value of conductivity in this period increases with the increase in *w/b*. Pastes blended with FA has the similar trend as OPC paste from 10 h to 12 days, but conductivity of FA pastes decreases a little faster than OPC. In the slag blended paste, conductivity has a continuous decease up to 12 days due to its latent hydraulic reactivity. This trend was also reported in many previous investigations [21,48,49], which implies that the electrical conductivity is an effective way to index the reactivity of SCMs.

4.3 Water distribution in hcp

The weight loss at 60 °C under vacuum includes not only the water in pore solution but also the interlayer water, and this is here classified as Epw in Figure 4.3. A higher *w/b* results in more content of Epw at any hydration ages, leading to a higher porosity. The nonevaporable water (Nw) denotes the weight loss after the vacuum dried to oven dried at 1000 °C. For the pastes with *w/b* of 0.35 and 0.45, the carbonation is weak. It can be induced from the fact that the measured total water to binder ratio is close to the original proportion value.

OPC with *w/b* of 0.35 shows a slow growth in the amount of Nw at V60–500 °C after 3 days, while the water at 500–1000 °C shows an evident increase. Pastes with *w/b* of 0.45 and 0.55 have a higher Nw content in hcp than pastes with *w/b* of 0.35 after 1 day. This confirms that the water availability is critical for the later age hydration. Nw of FA blended pastes has a rather stable value after 7 days. Nw in FA pastes at V60–500 °C is much lower than that in OPC pastes due to the dilution effect from FA. However, Nw of FA pastes at 500–1000 °C is not lower than that of OPC paste, since SCMs will accelerate the hydration of clinker [81]. The *w/b* has a weaker effect on the bound water in FA hcp than OPC paste.

The content of Nw in SL pastes at V60–500 °C is lower than that in OPC. An enhancement effect on bound water can be observed if we normalized the bound water content to the weight of OPC and this is similar to Escalante-Garcia's investigation [82]. With a *w/b*=0.35 or 0.45, the weight loss of SL pastes at V60–1000 °C is close to that of FA pastes, but the amount of Nw in SL pastes at V60–500 °C is apparently higher than FA pastes from 7 to 12 days. The Nw content increases with w/b after 10 h, and this increasing effect on the blended paste is much weaker than that on OPC paste. The ternary system with limestone has a similar trend as SL binary pastes in the change of bound water content.

Figure 4.3b shows the bound water content in the well hydrated paste (particles with D<1 mm curing under moisture condition for 390 days at 20 °C). The bound water in OPC, FA, SL and ternary pastes is 0.245, 0.188, 0.204 and 0.164 g/g dry binder respectively. The bound water in pastes with different binders at V60–350 °C has a similar value except for a lower amount in ternary paste.

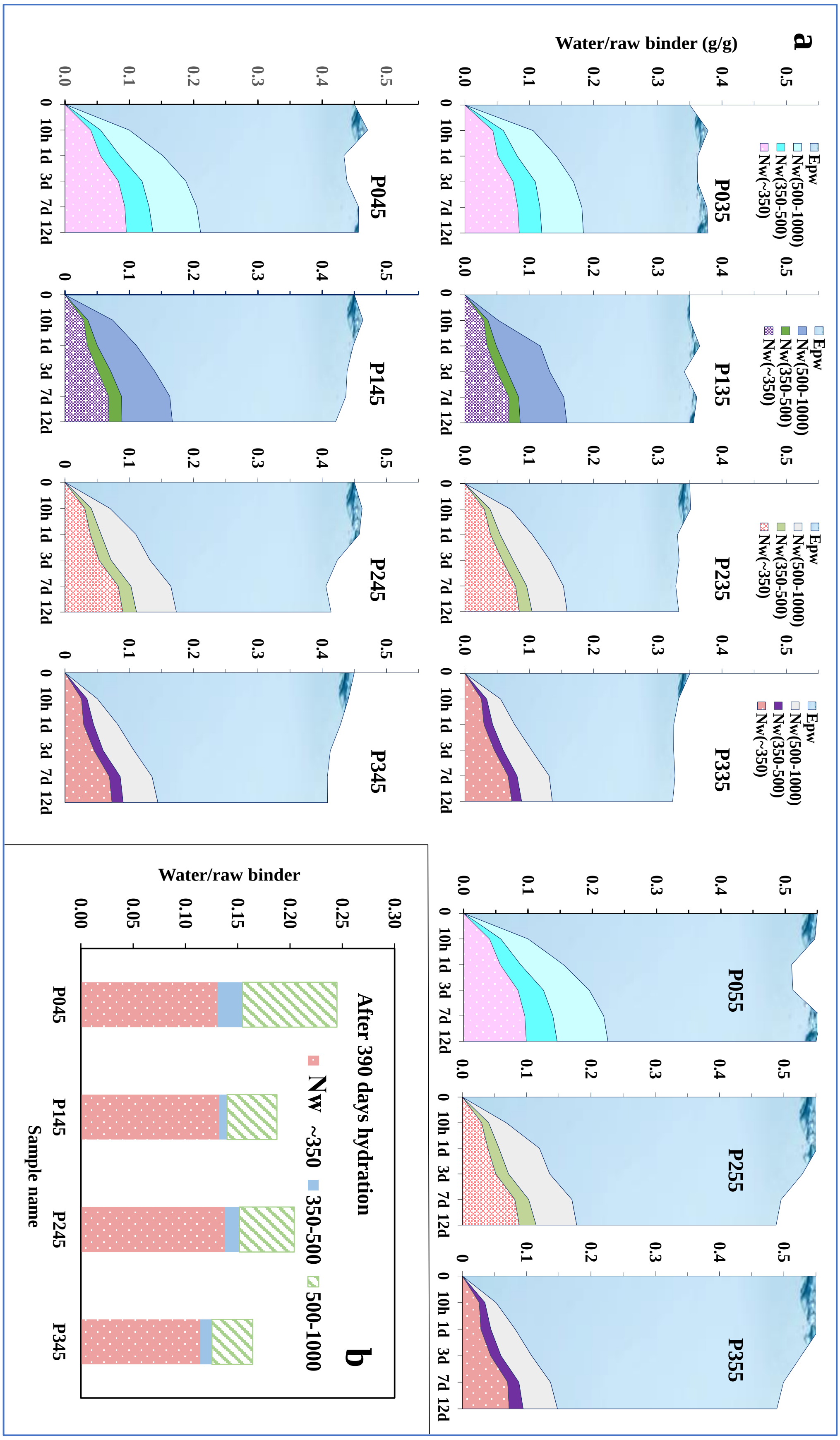

Figure 4.3. Water distribution in pastes at different hydration times.

4.4 Conductivity of pore solution versus time

Ions in the pore solution is the main conductive component in the hcp. The apparent ionic conductivity of the dilute solution is determined by the concentration of ions with high diffusivity in solution. The concentration of the highly soluble alkali ions can be calculated with the volume of Epw from the last section. The volume of Epw can be calculated by:

$$V_{epw} = \frac{m_{epw}}{\rho_{epw}} = m_b \times \varphi_{epw} \tag{4.1}$$

where *Vepw* is the volume of Epw in the paste, m_{epw} is the mass of Epw, ρ_{epw} is the density of water (0.998 g/cm^3 at 20 °C) and m_b is the mass of binder in paste.

The concentration of K^+ and Na^+ in pore solution of OPC pastes can be calculated by Eq. 4.2 based on these two assumptions: The alkalis in clinker completely dissolve into pore solution within the first few minutes after mixing with water; and the solvent exchanged water, including interlayer water, is classified as the conductive "pore solution". The latter assumption is reasonable because Lothenbach and Nonat [61] proposed that a part of alkalis was absorbed in the interlayer space.

$$C_i = \frac{m_b \times \delta_{ic}}{V_{epw}} = \frac{\delta_{ic}}{\varphi_{epw}} \tag{4.2}$$

where C_i denotes the concentration of alkalis, *i* represents alkali ions K^+ or Na^+, and δ_{ic} is the mole concentration of chemical composition in binder as presented in Table 2.1. Because the alkalis in slag is not as soluble as them in OPC clinker, the effective mole concentration of alkali ions was used for the SL pastes ($\delta_{iblended}$) and it needs to be modified by the Eq. 4.3 [83].

$$\delta_{iblended} = \left(1 - 1.8 \times \left(\frac{m_s}{m_b}\right)^2\right) \times (\delta_{is} \times \frac{m_s}{m_b} + \delta_{ic} \times \frac{m_c}{m_b}) \tag{4.3}$$

where m_s and m_c represents the weight of SCMs and cement in the proportion respectively, δ_{is} is the mole concentration of alkalis in SCMs. K_2O and Na_2O in FA are hardly soluble during the early hydration, so the contribution of alkalis from FA is negligible (m_s=0). In addition to K^+ and Na^+, the highly conductive ions in the pore solution consist of OH^-, Ca^{2+}, SO_4^{2-} and Cl^-. The concentration of sulfate ions can be roughly approximated by Eq. 4.4 according to [84], and the value of α is 0.06 L/mol. Because of the low content of Cl in binder (see Table 2.1), its concentration in pore solution is negligible. Ca^{2+} concentration was assumed to be constant with 25 mmol/L which is the typical saturated concentration during the early hydration [85]. OH^- concentration was then calculated from charge balance by Eq. 4.5. The conductivity of electrolyte in the pore solution (σ_{ps}) can be expressed as a sum of molar conductivity of each ionic species (*i*) as Eq. 4.6 [86].

$$c_{{SO_4}^{2-}} \approx \alpha(c_{K^+} + c_{Na^+})^2 \tag{4.4}$$

$$c_{OH^-}{=}c_{K^+} + c_{Na^+} + 2c_{Ca^{2+}} - 2c_{SO_4{}^{2-}} \qquad (4.5)$$

$$\sigma_{ps} = \sum_i z_i \lambda_i c_i \qquad (4.6)$$

where z_i and c_i are the valence and molarity of "*i*" species, respectively. λ_i is the equivalent conductivity that is related to the ionic strength (I_M) and conductivity coefficients (G_i) in the solution with high concentration level [73]:

$$\lambda_i = \frac{\lambda_i^0}{1+G_i \times I_M^{1/2}} \qquad (4.7)$$

λ_i^0 is the equivalent conductivity of ionic species in infinite dilution condition. This value for the relevant ions at 20 °C was obtained from the literature [87] by interpolation. G_i of specific ions refers to the value in [73]. The I_M is defined as follow:

$$I_M = \frac{1}{2}\sum_i z_i^2 \, c_i \qquad (4.8)$$

The conductivity of pore solution was calculated by use of Eq. 4.1-4.8 with the chemical composition in Table 2.1 and Epw content in hcp at corresponding hydration time. The ion concentration in the squeezed pore solution form [88,89] was applied into Eq. 4.6–4.8 to calculate the conductivity of pore solution in the corresponding mixture from the published papers. The evolution of conductivity of pore solution with time was fitted by the Hill function, and the optimized parameters and function expressions are presented in Table 4.1.

Table 4.1. The fitting results of conductivity of pore solution versus time by the Hill function.

Sample	Expression ($\sigma_{ps}(t)$)	End value(mS/cm)	R^2
P035	$\sigma_{ps}=95.6+(165.9-95.6)\times\tau^{1.86}/(\tau^{1.86}+144.4)$	165.9	0.998
P045	$\sigma_{ps}=76.9+(131.3-76.9)\times\tau^{2.25}/(\tau^{2.25}+512.0)$	131.3	0.998
P055	$\sigma_{ps}=65.2+(102.9-65.2)\times\tau^{2.25}/(\tau^{2.38}+503.0)$	102.9	0.987
P135	$\sigma_{ps}=63.1+(104.4-63.1)\times\tau^{1.5}/(\tau^{1.5}+108.8)$	104.4	0.996
P145	$\sigma_{ps}=51.6+(96.0-51.6)\times\tau^{0.75}/(\tau^{0.75}+27.0)$	96.0	0.995
P235	$\sigma_{ps}=75.2+(149.6-75.2)\times\tau^{0.96}/(\tau^{0.96}+31.4)$	149.6	0.990
P245	$\sigma_{ps}=61.7+(114.5-61.7)\times\tau^{1.13}/(\tau^{1.13}+116.9)$	114.5	0.992
P255	$\sigma_{ps}=52.4+(111.6-52.4)\times\tau^{0.75}/(\tau^{0.75}+60.3)$	111.6	0.96
P335	$\sigma_{ps}=61.4+(133.3-61.4)\times\tau^{0.60}/(\tau^{0.60}+16.7)$	133.3	0.998
P345	$\sigma_{ps}=50.6+(86.9-50.6)\times\tau^{0.88}/(\tau^{0.88}+35.8)$	86.9	0.995
P355	$\sigma_{ps}=43.8+(78.0-43.8)\times\tau^{0.86}/(\tau^{0.86}+84.9)$	78.0	0.994

Figure 4.4a presents the conductivity of pore solution and the fitted line of 11 samples. The conductivity decreases as the increase of *w/b* and the blending of SCMs lowers the conductivity of pore solution. This is consistent with the data from the squeezed pore solution (see Figure 4.4b). Shi [90] also found that SCMs would reduce the calculated conductivity of pore solution. Although the FA in [89] has a high alkali content (3.9% K_2O and 0.9% Na_2O), the concentration of K^+, Na^+ and OH^- in the pore solution of FA pastes is similar to that in the paste replaced with an identical mass of quartz. Therefore, it confirms our assumption that alkalis in FA is hardly dissolvable.

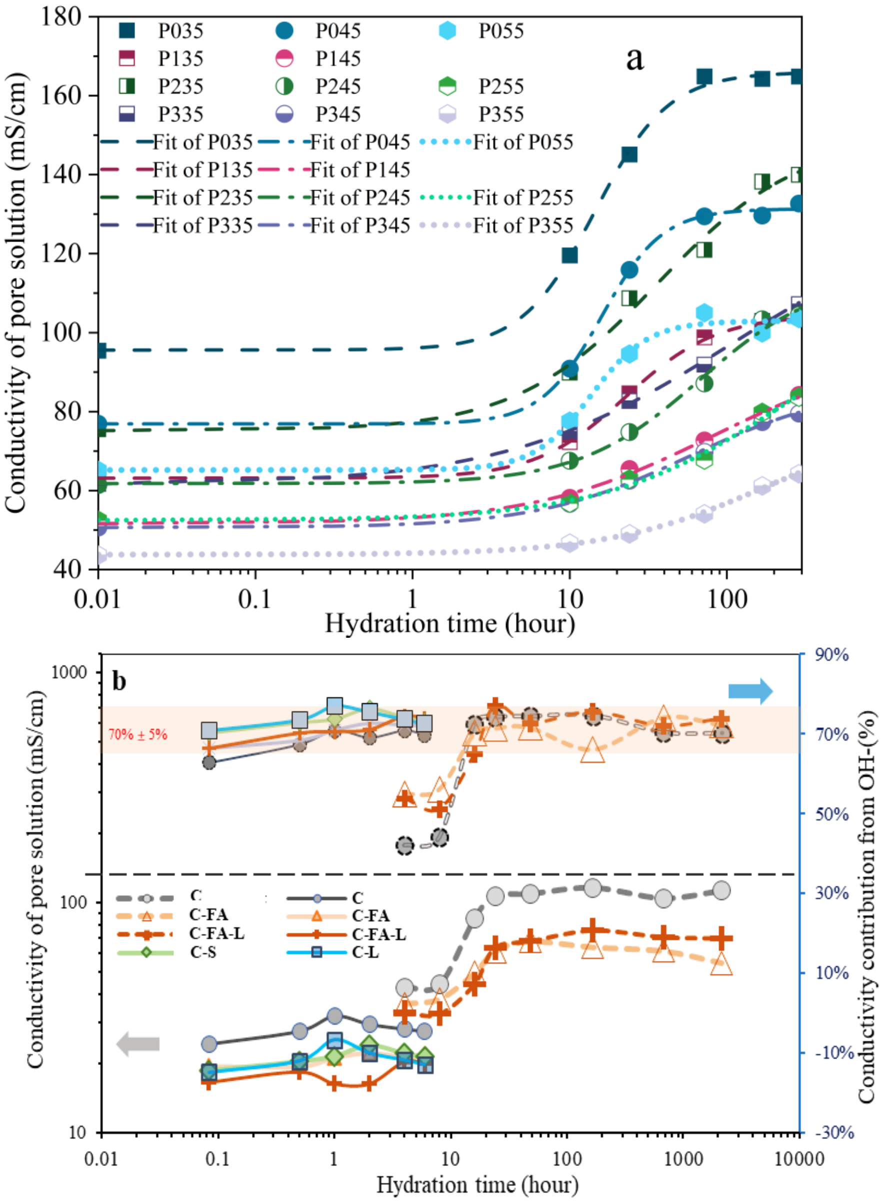

Figure 4.4. Calculated conductivity of pore solution. (a)- the values in this paper. (b)-the conductivity value calculated based on tested concentration of squeezed pore solution from literatures (solid line from [88] with *w/b*=0.75 , dash line from [89] with *w/b*=0.5, C: OPC; FA: fly ash; S: slag; L: limestone).

The initial conductivity from experiments in Figure 4.2 is lower than the calculated conductivity of pore solution, because the presence of cement particles breaks the connectivity of pore solution. The chemical composition of OPC in this study is highly similar to OPC used in [89], so the calculated conductivity evolution of P055, based on chemical composition and Epw, is close to that of OPC with *w/b*=0.5 based on the squeezed pore solution (see light blue hexagon in Figure 4.4a and dashed line sphere in Figure 4.4b). The main contribution to the conductivity of pore solution is from the OH^-, which accounts for around 70%. The conductivity of pore solution stays almost constant before it has a sharp increase after approximately 6 h. The fitted line of data in this study has the similar trend as the evolution of value calculated from the squeezed pore solution. It implies that Eq. 4.1–4.8 can effectively quantify the electrical conductivity of pore solution with no need to squeeze pore solution from hcp or operate the further test of ion concentration with the expensive equipment (ICP-OES, IC, AAS [85]).

4.5Index for structure evolution

4.5.1 Evolution of *F*

The formation factor (*F*) was initially defined by Archie [91] as a fundamental property to describe the correlation between the electrical conductivity of sandstone and the permeability or porosity. hcp has the same porous nature as sandstone, so *F* is widely used in the cement-based materials to indicate the diffusivity of ions in hcp by the definition of [92,93]:

$$F = \sigma_{ps}(t)/\sigma_p(t) \tag{4.9}$$

where $\sigma_p(t)$ is the conductivity of bulk paste or concrete, and it is the conductivity of natural saturated hcp in this study. $\sigma_{ps}(t)$ is the conductivity of pore solution, and t is the hydration time.

F of hcp was calculated with the real-time electrical conductivity of paste (Figure 4.2) and the fitted line of pore solution (Table 4.1). Figure 4.5 displays evolution of *F* in all 11 pastes up to 12 days. *F* has a near constant value from 2 to 9 h, and the constant duration varies due to different *w/b* and the blending of SCMs. The initial *F* is larger than 1 and it generally deceases with the increase in *w/b*. It enters a sharp increasing stage after the constant period, which is related to setting and hardening of paste. A similar critical point was found in the ultrasound test due to the percolation of solid [94,95]. The effect of *w/b* on *F* is magnified as the hydration proceeds into the fast growth period. The ratio of *F* at 24 h between paste with *w/b* of 0.35 and 0.45 is 1.90, 2.57, 3.90 and 2.05 for OPC, FA, SL and ternary system, respectively.

Figure 4.5b illustrates the comparison of hcp with *w/b* of 0.35. OPC paste has the highest *F* before 36 h, but its increase slows down earlier than the blended paste. Therefore, *F* of SL blended paste exceeds that of OPC after 36 h and the difference between them become larger as the hydration goes on. LL reduces the growth rate of *F* before 36 h, but *F* of ternary pastes climbs up to exceed that of OPC at 110 h. It goes close to the *F* of SL binary pastes at 12 days. The *F* of FA pastes is lower than that of other pastes due to the low pozzolanic reactivity at early age, but the differences between FA paste and OPC narrow down after 36 h.

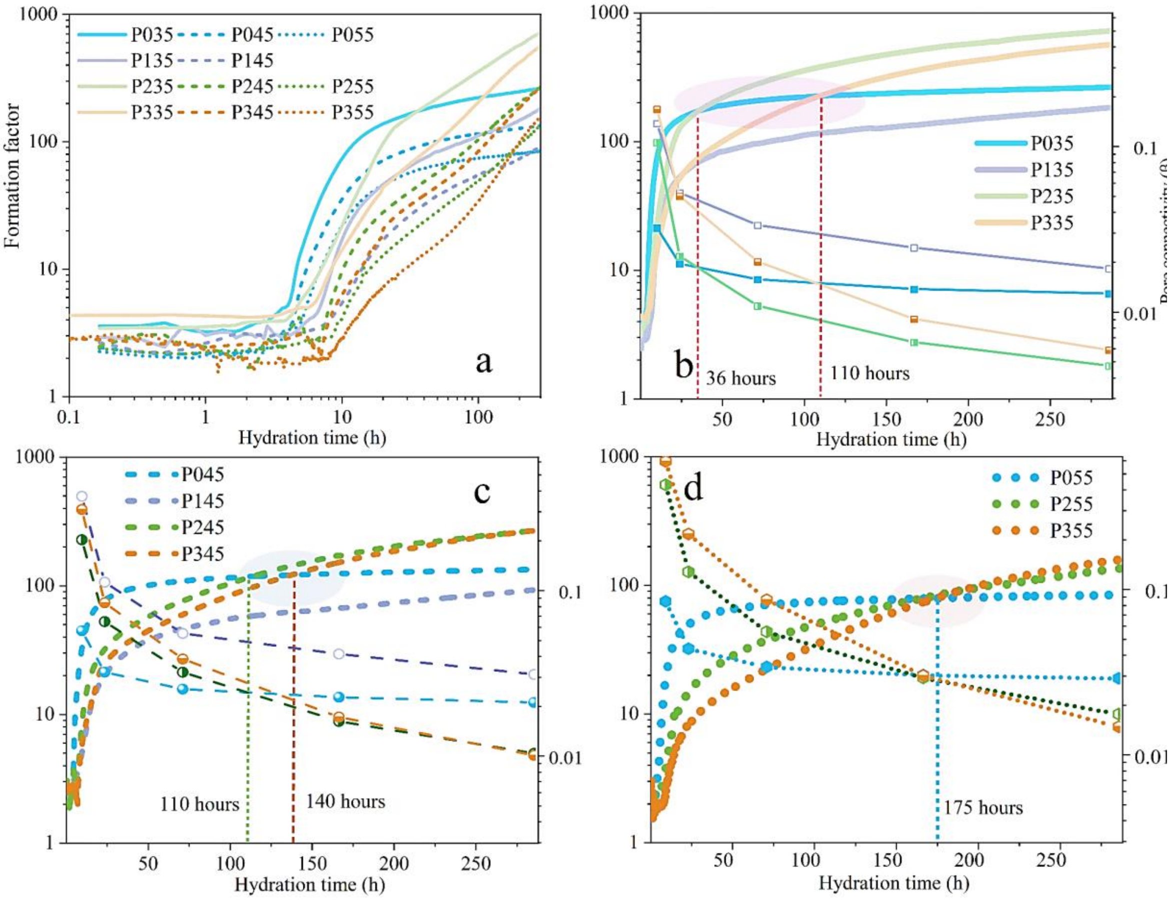

Figure 4.5. Evolution of formation factor and pore solution connectivity with hydration time.

The differences between OPC and SL paste were magnified before 24 h when the *w/b* increases to 0.45. The overlapping points of P045 with P245 and P345 are at 110 and 140 h, respectively, which time is much longer than that in paste with *w/b* of 0.35. LL has a weaker effect on the growth of *F* in pastes with *w/b* of 0.45 than 0.35. An increment of *w/b* to 0.55 intensifies the inhabitation effect of SL and LL on the growth of *F* before 24 h. The *F* of P255 and P355 exceed that of P055 at the same time of 175 h. *F* also relates to the pore connectivity as the following equation [92,96]:

$$F = \frac{1}{\Phi\beta} \tag{4.10}$$

where Φ is the porosity of paste and β is the index of pore connectivity. Herein, the water porosity was used to calculate the pore connectivity, and it is defined as:

$$\Phi_e = \frac{V_{epw}}{V_p} = \frac{m_1 - m_e}{m_1 - m_0 - m_v} \tag{4.11}$$

V_p is the volume of hcp. The pore connectivity (β) was deduced with the water distribution in Figure 4.3 and F. The evolution of β is presented in Figure 4.5b–d as well. An increment in *w/b* increases the pore connectivity in hcp. The pore connectivity decease dramatically from water addition to 24 h, and this period also corresponds to the main peak in the heat release during hydration of cement-based pastes [97]. A comparison of connectivity between OPC, SL and ternary paste implies that the differences in *F* of the various binder system mainly derives from the discrepancies in pore connectivity.

4.5.2 Correlation between the setting time and *F*

The setting of cement paste is generally understood as a percolation process in which intersection of hydration products on particles surface leads to the formation of clusters, and which eventually builds a continuous elastic network [94]. In pastes with normal amount of aluminates in clinker, the setting is mainly controlled by a formation of sufficient C-S-H on particles surface [98,99]. The increasing precipitation of C-S-H results in the percolation of the links that are created by the packing of C-S-H on the surfaces of particles. Many previous researches [100–102] found a reduction in conductivity of paste during setting. However, it lacks a mathematical relation between electrical properties and setting time.

Table 4.2. Setting time and inflection points of *F* form all pastes.

Sample	Time/h		
	Initial setting	Final setting	Inflection time of F
P035	2.82	4.37	4.07
P045	3.62	5.02	4.38
P055	4.14	6.80	5.04
P135	4.06	6.65	6.35
P145	4.85	7.17	7.30
P235	2.99	5.72	4.60
P245	4.20	7.92	7.50
P255	4.49	9.50	8.80
P335	3.08	6.12	6.25
P345	4.13	7.97	7.33
P355	5.82	10.23	9.30

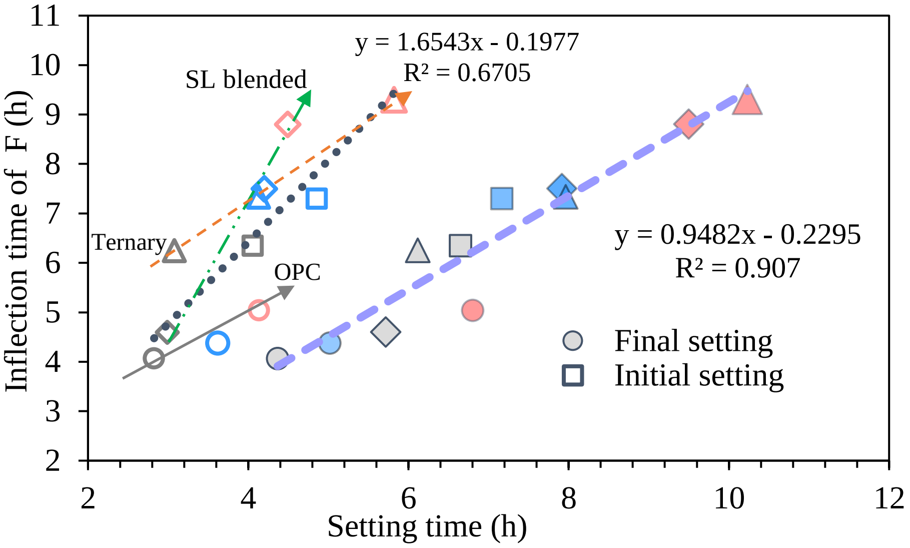

Figure 4.6. Correlations between setting time and inflection point of *F*. The data of OPC, FA, SL and ternary paste are presented with circle, square, rhombus and triangle respectively. The gray, blue and rose color correspond to *w/b* of 0.35, 0.45 and 0.55, respectively.

Table 4.2 and Figure 4.6 show that the inflection point of *F* has a good linear correlation with the final setting time regardless of binder types or *w/b*. The linear correlation between the inflection points and initial setting time is not so strong, but they have a good correlation with respect to binder types (see the arrow line in Figure 4.6). This may be due to the differences of particles size distribution (or surface nature in solution) between cement and SCMs. It should be noted that the points for calculation of setting time, more or less, is arbitrary chosen in the standard for setting test (ASTM C191-08, Vicat). Therefore, the change of *F* during hydration is a good index for setting of pastes.

4.6 Discussion

4.6.1 Hydration process and the evolution of conductivity

Hydration of cement can be mainly classified into two simplified processes: the dissolving of solid minerals in water to increase the ion concentration in the liquid pore solution; from that it follows the precipitation of solid hydration products. Figure 4.7 illustrates the two phases in the freshly mixed paste. It consists of the solid particles and liquid pore solution. The conductivity of solid particles is about 1×10^{-8} mS/cm [103], which is far less than the typical ionic conductivity of pore solution (σ_s=10–200 mS/cm from [103], also see Figure 4.4). Therefore, the dry solid part can be treated as the insulative component ($\sigma_s \rightarrow 0$).

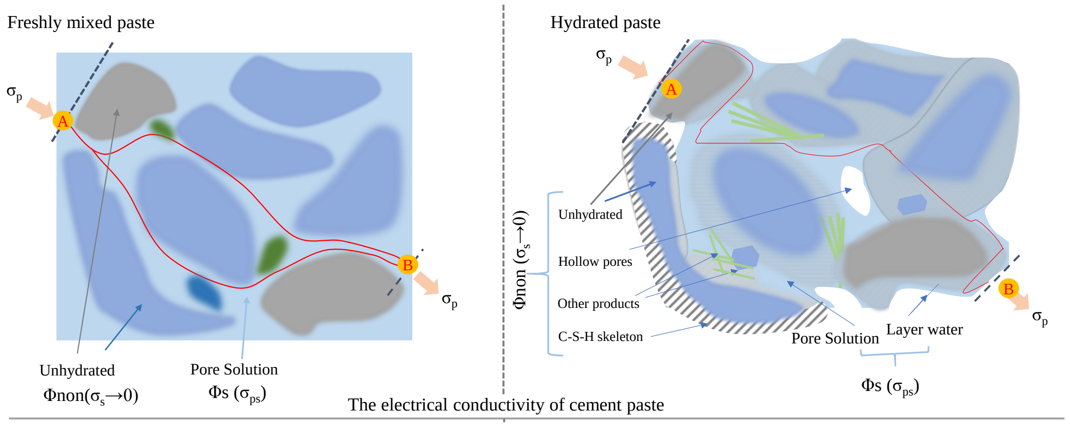

Two phases system (neglect the entrained air)
☐ unhydrated particles: $\sigma_s \rightarrow 0$ mS/cm
☐ Unhydrated particles distribute dispersedly (due to the double layer)
☐ Sufficient pore solution continuously connect together (red line)
☐ The electrical conductivity of paste is from the ions in pore solution and ions on the particle surface

Three phases system (neglect the entrained air)
➢ unhydrated particles, C-S-H skeleton, other products and hollow pore $\sigma_s \rightarrow 0$ mS/cm
➢ Consumption of free water reduces the volume of pore solution
➢ The decrease of pore solution and connection of hydration products increase tortuosity of paste
➢ The electrical conductivity of paste is determined by the ions in pore solution ,ions on the particle surface and layer water.

Figure 4.7. A schematic of electrical conductivity evolution during hydration.

The current transmission through paste mainly depends on the diffusion/migration of ions in pore solution and near the surface between solid and solution [104,105]. Although the particles at early age turn to disperse due to the similar surface charge, it makes the current route tortuous other than a straight conduction through paste (see red line in Figure 4.7). This explains that the *F* of freshly mixed paste is larger than 1. The increasing precipitation of hydration products (mainly C-S-H) will build links between the particles, so the current route becomes much more tortuous (red line in the hydrated paste) than in the fresh paste. The decrease in Epw induces an increase in alkalinity of pore solution after about 10 h [89], so it activates the reactivity of SCMs. The further hydration of SCMs will decrease the connectivity of pore solution to reduce the *F*. The growth rate of *F* implies the growth rate of hydration products indirectly but effectively.

4.6.2 *F* and water content

The electrical conductivity shows a general relationship with the volume of pore solution as a format similar to Archies' law (see Eq. 4.12) after an extension of the percolation theory in networks to the continuum cases [106,107],

$$\sigma_p = \mathrm{a} \times \sigma_{ps} \times (\phi - \phi_c)^{\mathrm{m}} \tag{4.12}$$

where a is non-uniform constant, m is the shape factor. After the substitution of conductivity with formation factor *F*, the new equation reads:

$$F = 1/\mathrm{a} \times (\phi - \phi_c)^{-\mathrm{m}} \tag{4.13}$$

where ϕ is the volume fraction of Epw (ϕ_{epw}). ϕ_c is the critical value for the percolation of conductive component.

Table 4.3 shows the optimum parameters after the regression of *F* and water porosity of hcp. The *F* correlates perfectly with the volume of Epw through a general percolation theory with respect to binder type (see R^2 in Table 4.3). The values of percolation threshold for pore solution in plain OPC, fly ash, slag and ternary blended pastes are 0.157, 0.242, 0.223 and 0.256 respectively. This implies that OPC paste requires the lowest volume of pore solution to form a percolation of liquid phase, which means that it has the highest pore connectivity compared with blended system after setting. Gui et al. [79] found that FA and SL have refined the pore structure to decrease the pore connectivity in pastes, thus reducing the gas permeability. SL and FA has the declining effect on the chloride migration in hcp as well [107,108], and the refinement in the pore structure is one of the principal reason. The site threshold values for face centered cubic and body centered cubic is 0.198 and 0.245 respectively, according to lattice model for percolation [109]. Therefore, blending of SL and FA may refine the spatial distribution of pores, which is worthy of consideration in the future modelling of ions or moisture transport in the hcp.

Table 4.3. The regressed parameters based on Eq. 4.13.

Sample	Expressions	a	Φ_c	m	R^2
P0	$F=1/0.246\times(\Phi_{epw}-0.157)^{-2.11}$	0.246	0.157	2.11	0.98
P1	$F=1/0.498\times(\Phi_{epw}-0.242)^{-1.52}$	0.498	0.242	1.52	0.93
P2	$F=1/0.806\times(\Phi_{epw}-0.223)^{-2.35}$	0.806	0.223	2.35	0.99
P3	$F=1/0.578\times(\Phi_{epw}-0.256)^{-1.82}$	0.578	0.256	1.82	0.97
PA	$F=1/0.129\times(\Phi_{epw}-0.279)^{-0.98}$	0.129	0.279	0.98	0.74

4.7 Summary

The evolution of conductivity in the hydrating pastes closely relates to the chemical reaction process. It can be classified into four stages during early hydration. It shows that the differences in *F* of pastes with various binders are mainly derived from the discrepancies in the pore connectivity.

The *w/b* has impact on the electrical conductivity and *F* of pastes. The increase in *w/b* lowers the alkali concentration in pore solution, resulting in the reduction in conductivity of pore solution. However, it increases the connectivity of pore solution to reduce the *F* of hcp. The reduction magnitude of *F* due to the increase of *w/b* in each binder system keeps near constant after a certain age. The growth rate of *F* value can effectively indicate the reactivity of different binders.

SCMs reduce the initial conductivity of pastes mainly due to decrease in alkali concentration in pore solution. SL has a weaker reduction effect on the conductivity of pore solution than FA. Blending of SCMs refines the pore structure, causing a decrease in the connectivity of pores. LL increases the connectivity of pore solution compared with SL and FA. However, its filling effect is evident after a certain hydration age. FA induces a reduction in the *F* of hcp before 12 days due to its low reactivity at early age.

The relation between volume of Epw and *F* can be well demonstrated by the extended percolation theory. This enables an in-situ monitoring of Epw by the measurement of conductivity. This study provides the methods for monitoring moisture, concentration of alkali ions in pore solution, *F* and pore connectivity of pastes. It can provide the data for the prediction and simulation of moisture transport and chloride migration in concrete during its service life with the continuous long-term hydration.

5 Moisture and ion transport properties and their relationship to pore structure

This chapter demonstrates the moisture transport properties in hcp measured by the new procedure and setup shown in Figure 2.6. Both the vapor diffusion coefficient (D_v) and the total moisture transport coefficient (D_w) of the sample were measured in one procedure. The chloride migration coefficient in hcp was tested by the rapid chloride migration method (RCM). The pore size distribution in the hcp was detected by the mercury intrusion porosimeter (MIP) to reveal the relation between pore structure and the moisture transport properties. The refinement effect of SCMs on the pore structure in pastes was deeply discussed by the interpretation of different parameters. The differences in moisture and chloride transport in pastes were comprehensively compared to the pore structure parameters.

5.1 Introduction

The effect of SCMs on the chloride migration in cement-based materials have been generally investigated from both experimental and modeling aspect [110–115]. However, a limited number of published papers was found to reveal the effect of SCMs on the moisture transport properties in hcp. Baroghel-Bouny [29] reported that 8%–10% silica fume reduced the apparent moisture diffusion coefficient of concrete when the saturation degree of hcp is higher than 50 %. Saeidpour and Wadsö [116] investigated the differences in the vapor diffusion coefficient of the blended mortar during adsorption and desorption processes by use of a new cup method. They found that silica fume and slag induced one magnitude reduction in the vapor transport coefficient in both adsorption and desorption processes. This effect was ascribed to the higher amount of gel pores and lower volume of capillary pores in the blended system. Olsson et. al [26] reported the same reducing effects from silica fume and slag on vapor diffusion coefficient, and it is more evident at the higher RH levels. The authors tried to correlate the difference in vapor diffusivity with the change of C-S-H structure, but no plausible correlation was concluded.

The high moisture resistance in the blended system are mainly due to the refinement on the pore structure, which was also mentioned in many published papers [26,27,116]. However, a correlation between the pore structure and moisture transport yet to be clarified. Berodier and Scrivener [15] found that slag reduced the critical pore size (CP) of hcp cured in water for 28 days, so CP was considered as the main controlling factor for the vapor transport in hcp [26,27]. The FA blended hcp normally has the similar and even larger CP compared to OPC paste before 90 days [15,117], but its vapor diffusion coefficient is much smaller than OPC. Therefore, CP is not the main controlling factor in this situation. There are many parameters for pore structure in hcp, which includes porosity, pore size distribution, pore connectivity, tortuosity, the critical entry pore size (CP) and formation factor (*F*). This study will present a clear correlation between moisture/chloride transport properties with the pore structure parameters in hcp.

5.2 Calculation of moisture transport properties

The gradient of moisture content was considered as the driving force for moisture transport in non-steady-state conditions during the semi-infinite drying process, so its distribution inside the paste follows Eq. 5.1 [118,119].

$$\frac{(C-C_1)}{(C_0-C_1)} = \mathrm{erf}\frac{x}{2\sqrt{D_w t}} \tag{5.1}$$

where C_0 and C_1 (kg/m^3) are the initial moisture content in the pastes (moisture content at RH=97% in this study) and moisture content on the drying surface (moisture content at RH=50% or 75%), respectively. The x is the distance from the surface to the inside position where the moisture content is C. D_w (m^2/s) is the total moisture transport coefficient and t (sec) is the duration of drying time. The loss of substance from the semi-infinite medium is given by:

$$\left(D_w \frac{\partial C}{\partial x}\right)_{x=0} = \frac{D_w(C_0-C_1)}{\sqrt{\pi D_w t}} \tag{5.2}$$

Hence, an integral of Eq. 5.2 from zero time to t can get

$$M_t = 2(C_0 - C_1)\sqrt{\frac{D_w t}{\pi}} = k_w\sqrt{t} \tag{5.3}$$

M_t (kg/m^2) is the moisture loss of samples drying to time t. We can furtherly get the drying coefficient k_w by the regression of moisture loss (M_t) and $\sqrt{t}$ (shown in Figure A3 in Appendix). Thereafter, the total moisture transport coefficient D_w can be obtained by Eq. 5.4.

$$D_w = \frac{\pi k_w^2}{4(C_0-C_1)^2} \tag{5.4}$$

The vapor diffusion coefficient $D_{v,s}$ (m^2/s) during semi-infinite drying was defined as [120]:

$$D_{v,s} = \frac{D_w}{v_s} \times \frac{dW}{d\varphi} \tag{5.5}$$

where $dW/d\varphi$ is the moisture capacity of pastes. Herein, the average moisture capacity was adopted, and it was calculated by Eq. 5.6. W_1 *and* W_2 are the moisture content in hcp under φ_1 and φ_2, respectively. They can be calculated by Eq. 5.7.

$$\frac{dW}{d\varphi} = \frac{W_2 - W_1}{\varphi_2 - \varphi_1} \tag{5.6}$$

$$W_i = \frac{m_i - m_0}{\frac{m_0}{\rho_0}} = \frac{\rho_0(m_i - m_0)}{m_0} \tag{5.7}$$

where m_i is the weight of pastes at RH=φ_i, m_0 is the weight of pastes vacuum dried at 60 °C and ρ_0 is the bulk density of the vacuum dried pastes.

The vapor diffusion through the disc obeys the Fick's first law at the steady state.

$$j_{v,t_i} = \overline{D_{v,t_i}}\frac{\Delta v}{h} \tag{5.8}$$

where j_{v,t_i} is the vapor flux during the diffusion from time $t_{i\text{-}1}$ to t_i. t_i corresponds to the latest time weighing the tubes. Δv (kg/m^3) is the difference of vapor content between the upper and lower surfaces of specimens and h (m) is the thickness of disc. The leakage of dummy sample, Δm_{dt} (kg), was included in the calculation of vapor flux from $t_{i\text{-}1}$ to t_i so j_{v,t_i} can be calculated by Eq. 5.9.

$$j_{vt} = \frac{\Delta m_{st} - \Delta m_{dt}}{A\Delta t} \tag{5.9}$$

where $\overline{D_{v,t_i}}$ (m^2/s) is the average vapor diffusion coefficient between $t_{i\text{-}1}$ and t_i. Δm_{dt} is the weight loss of tubes with discs of pastes from $t_{i\text{-}1}$ to t_i. The surface vapor content is not so easy to measure, but the vapor content on the surface of the saturated salt solution and in the climate box (room) can be calculated by

$$v_i = v_s \times \varphi_i \tag{5.10}$$

where v_i is the moisture content in air at corresponding RH and v_s is the saturation moisture content in air (17.28 g/m^3 at 20 °C). Therefore, considering the surface moisture resistance ($K_{e,v}$) and moisture transport in tube air, the mass flux from the saturated salt solution to climate box reads

$$j_{v,t_i} = \frac{v_2 - v_1}{\frac{h}{D_{v,t_i}} + \frac{L}{D_0} + \frac{1}{K_{e,v}}} \tag{5.11}$$

$K_{e,v}$ is approximately 0.007 m/s for the specimens with size in this investigation [116]. By substituting the weight change (as shown in Figure A2 in Appendix) into Eq. 5.9, we can use Eq. 5.10 and 5.19 to calculate the average vapor diffusion coefficient from the tube method.

5.3 Moisture transport coefficient

5.3.1 Vapor diffusion coefficient

Figure 5.1 shows the typical data collected in the experiments for measuring vapor diffusion coefficient (D_v). It shows that both the temperature and RH were under well control. The assessed leakage from dummy samples stayed in a percentage range within 0–7% after 90 days (Figure 5.1c). The evolution of $\overline{D_{v,t_i}}$ for hcp with *w/b*=0.35 in two RH intervals was shown in Figure 5.1a. Samples reached a steady state flux after 32 days except for P035RH97–75. $\overline{D_v}$ of P035RH97–75 keep rising until 183 days, and this phenomenon exists in all the three parallel measurements (see the decreasing slope of weight loss in Figure A2-a in Appendix).

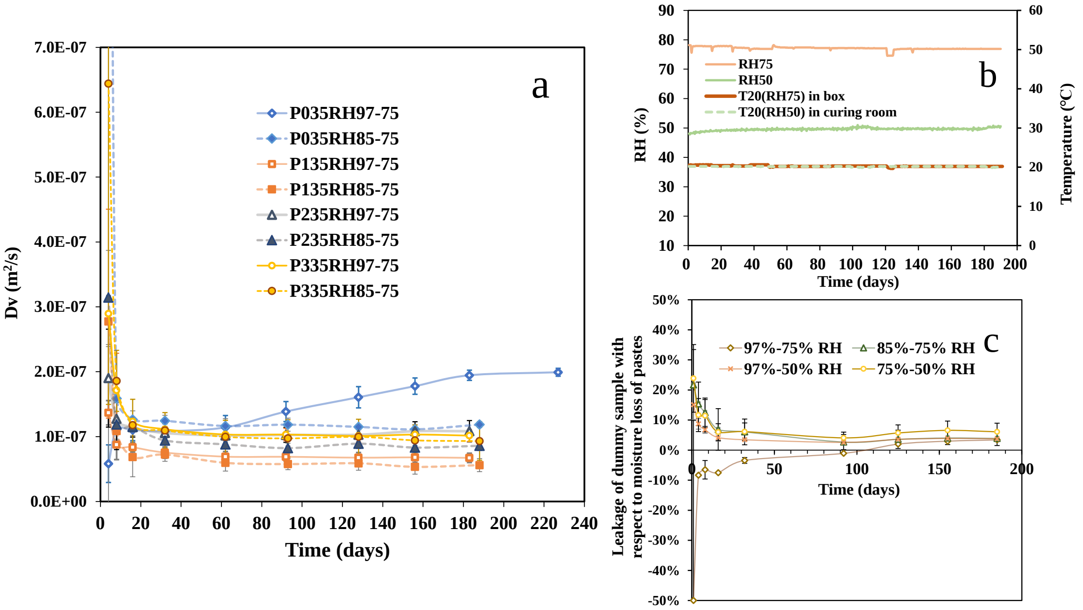

Figure 5.1. Some typical data during vapor diffusion coefficient test. a is the typical evolution of vapor diffusion coefficient versus time. b shows the conditioning temperature and RH monitored by testo 174H sensor. c is the leakage of dummy samples with respect to the weight loss of P1 sample at corresponding time. Note that D_v in figure is $\overline{D_v}$ in the text.

$\overline{D_v}$ of hcp at about 182 days is plotted in Figure 5.2 as the indication of the steady-state diffusion. The increase in RH intervals tend to increase the deviation within the 3 parallel tests. However, the deviation level in the tube method is lower than the traditional cup method. It is due to not only the better sealing of tube method but also the differences in mixtures and disc size compared to the results in [116]. Overall, the tube method for measuring D_v is at least as valid as the cup methods.

Figure 5.2a shows that FA binary paste (P135) has the lowest $\overline{D_v}$ with only half of that in OPC pastes (P035) before 80% RH interval (85% to 75%). SL binary paste has the highest $\overline{D_v}$ at RH75–50. Ternary and OPC pastes have the similar value staying in the middle of all the pastes. Because $\overline{D_v}$ of OPC pastes has an evident increase as RH increases, the differences between the OPC and blended pastes grows after this RH interval. This phenomenon is similar to the results reported in some previous investigations [26,27,116]. The $\overline{D_v}$ of the blended pastes seems to be moisture independent with only minor changes as RH increases. However, it is not completely RH independent given that we focus on the detail change of D_v of the blended pastes.

$\overline{D_v}$ of ternary hcp with a *w/b*=0.35 slightly decreases with the increase in RH intervals, and this of SL binary pastes has an increase after RH85–75 instead of keeping constant. Figure 5.2b presents that the decreasing trend is still observed in FA and ternary hcp with *w/b*=0.45 as the RH moves to the higher value. The reduction effect from SCMs on the D_v is more significant at the higher *w/b*. For instance, the $\overline{D_v}$ of SL blended paste normalized to OPC paste is 0.52, 0.29 and 0.14 in pastes with *w/b* of 0.35, 0.45 and 0.55, respectively. The further replacement by LL increases the diffusivity of pastes below RH97–50, but the differences in SL binary and ternary pastes are negligible in the high interval.

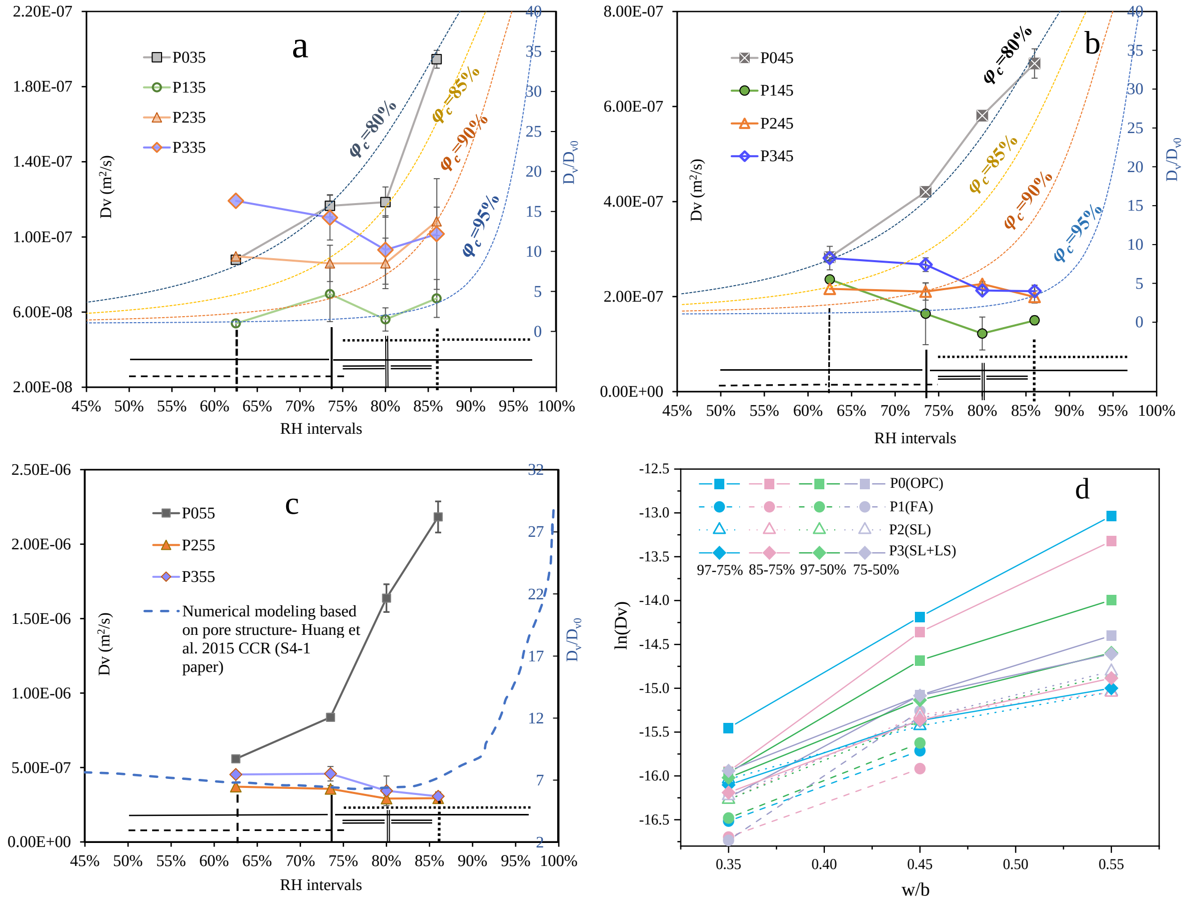

Figure 5.2. $\overline{D_v}$ of all the pastes in 4 RH intervals. a-pastes with *w/b*=0.35; b-pastes with *w/b*=0.45; c-pastes with *w/b*=0.55; d-comparison between pastes with different *w/b*. The evolution of D_v/D_{v0} calculated with Eq. 5.1 is also plotted in a and b with 4 different critical RH (φ_c=80%, 85%, 90% and 95%). A typical numerical modeling result is adopted in c from [121].

The logarithm of $\overline{D_v}$ almost has a linear correlation with *w/b*. An increase of *w/b* from 0.35 to 0.55 induces an increase factor about 2.5 and 10 in the coefficient of SL blended and OPC hcp respectively (Figure 5.2d). To describe the dependency of vapor diffusion coefficient on the RH condition, an empirical formula was proposed by Bazant and Najjar [122] and it was modified into Eq. 5.12 by Sakata [123]. This empirical function was supported by the simulation results based on the pore network model [124].

$$\frac{D_v}{D_{v0}} = 1 + \frac{\frac{D_S}{D_{v0}} - 1}{1 + (\frac{1-\varphi}{1-\varphi_C})^n} + (\varphi - 1)\frac{\frac{D_S}{D_{v0}} - 1}{1 + \left(\frac{1}{1-\varphi_C}\right)^{\mathrm{n}}} \quad (5.12)$$

where D_v,D_s and $D_{v0}$are the vapor diffusion coefficient in the cement-based materials with RH= φ, 1 and 0 respectively and n is an empirical exponent constant. Eq. 5.12 was applied to explain the difference in the dependency of D_v on RH condition. D_s/D_{v0} =50 was selected as the typical value for the OPC-based concrete with *w/b* about 0.45, based on both experimental results and simulations [26,116,121,124]. n=2 was used as the general exponent constant based on the previous percolation analysis in section 4.6.1 (see Table 4.3). The evolution of $^{D_v}/_{D_{v0}}$ in hcp with RH is illustrated in Figure 5.2a and b with different critical percolation RH (φ_c= 80%, 85%, 90% and 95%).

It shows that the modelled evolution with φ_c=80%–85% is close to the change of D_v in OPC hcp with RH, whereas and the evolution of D_v in blended pastes follows the modelled results with φ_c=95%. This implies that the percolation of pore solution in OPC hcp occurs under a much lower RH condition than that of the blended pastes, which is consistent with lower critical volume for the percolation of liquid in OPC than the blended pastes as found in the electrical conductivity test (see Table 4.3). The different percolation point of liquid in hcp may be the main reason for the big discrepancies in dependency of D_v on RH for different binder systems. Figure 5.2c shows that the mild decrease in D_v with the elevated RH may be due to the blocking of vapor transport without percolation of liquid flow according to the modeling results in [121].

5.3.2 Moisture transport during semi-infinite drying

Figure 5.3 shows the total moisture transport coefficient (D_w) and vapor diffusion coefficient ($D_{v,s}$) determined by the semi-infinite drying method. Pastes dried at 75% RH have a lower D_w than those dried at 50% RH. The D_w of cement-based materials showed a decrease as the saturation degree increase from zero and it reached the minimum value in some middle saturation degree (0.5–0.8) [29,125], so the D_w was also saturation dependent. After the liquid reached a percolation at the critical saturation point, D_w increased with the increase of moisture content. D_w of the blended hcp has a larger difference in 50% and 75% RH compared with OPC hcp and this effect is similar to the effect from silica fume [29].

The increase in *w/b* brings an increase in D_w. Blending of SCMs presents a significant reduction in the D_w in both 50% and 75% RH drying. The normalized factor of D_w at 75% RH stays in a range of 0.05–0.18, and the normalized factor has a decreasing trend toward the high *w/b* except for the ternary paste (see solid markers in Figure 5.3c). The ternary paste has the lowest D_w among hcp with *w/b*=0.35. SL binary pastes have the lowest D_w compared with the other pastes with *w/b* of 0.45 and 0.55. The further replacement of LL enhances the moisture transport in hcp. The blended pastes drying at RH=50% have a higher normalized factor compared with those dried at 75% RH. The normalized factors of FA or SL binary pastes are in a range of 0.18–0.27, and the FA blended hcp with *w/b*=0.45 has the lowest factor with 0.18. A further blending of LL increases the factor to 0.38–0.54, so that the factors of ternary hcp are almost twice as much as the factor of SL binary hcp.

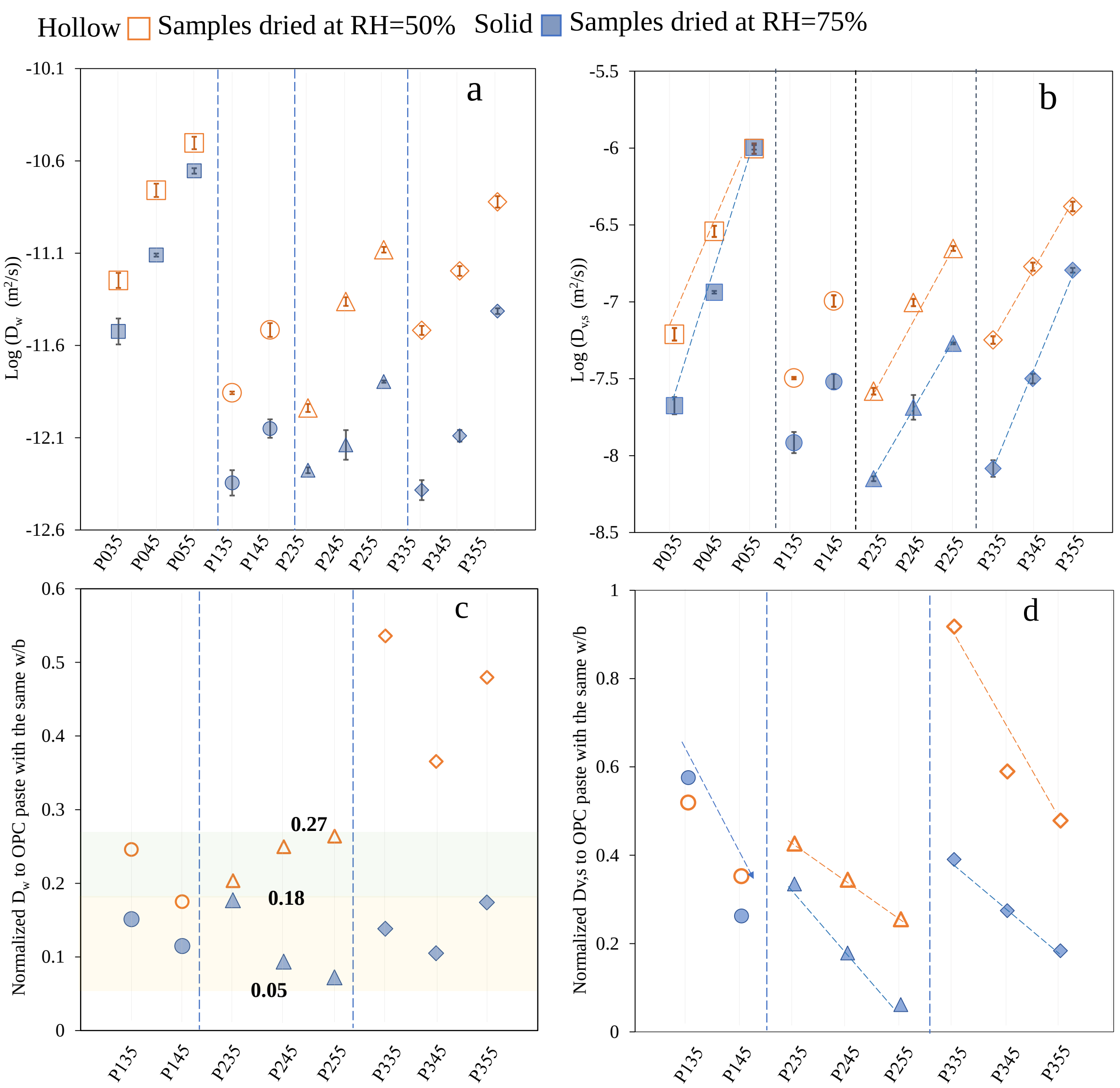

Figure 5.3. The D_w and $D_{v,s}$ of pastes during drying at RH=50% and 75% (20 °C): a-D_w of all pastes; b-$D_{v,s}$ of all pastes; c-D_w of the blended pastes normalized to the OPC pastes with the same *w/b*; d-$D_{v,s}$ of the blended pastes normalized to the OPC pastes with the same *w/b*.

Figure 5.3b and d show the $D_{v,s}$ and its normalized factor of hcp respectively. The discrepancy in $D_{v,s}$ at different RH is smaller than that in D_w. This phenomenon is more evident in the blended hcp mainly due to the higher moisture capacity ($dW/d\varphi$) in blended pastes compared with OPC (see Table A1 and A2 in Appendix). The logarithm of $D_{v,s}$ shows an almost linear correlation with *w/b*. The normalized factor of FA hcp has a value in the rage 0.26–0.58. The SL binary hcps have the lowest normalized factor in a range of 0.06–0.33 in 50% RH and 0.25–0.43 in 75% RH compared with the other hcps with the same *w/b*. The factor for ternary pastes is around 0.18–0.39 in 50% RH which is a little higher than SL binary. An increase in the drying RH induces a large increase in the normalized factor up to 0.92 (close to OPC) in P335. This value declines to 0.47 as the *w/b* increases to 0.55. The decrease in the normalized factor occurs as the *w/b* increases in the blended hcp. It is consistent with the findings in vapor diffusion coefficient. A further comparison between $D_{v,s}$ and $\overline{D_v}$ will be discussed in the final section.

5.4 MIP

MIP measurement was generally used to investigate the pore structure in the hardened cement-based materials. It should be noted that the pore size measured by MIP is not the actual size of pores in hcp, since size in MIP refers to the threshold diameter at the intruded pressure rather than a real size. The pore size calculated based on MIP pressure will underestimate the size of big pores within “ink-bottle” shape [126,127]. However, the threshold diameters and intrudable pore space from MIP provides comparative information between hcp with different proportions [117,126]. Figure 5.4 displays comparison of the differential pore size distribution in the hcp different proportions. The critical entry pore size (CP) corresponds to the size of pores at peak value in dV/dlog(D) curve [117]. It is the inflection point on the curve of intruded volume versus pore size.

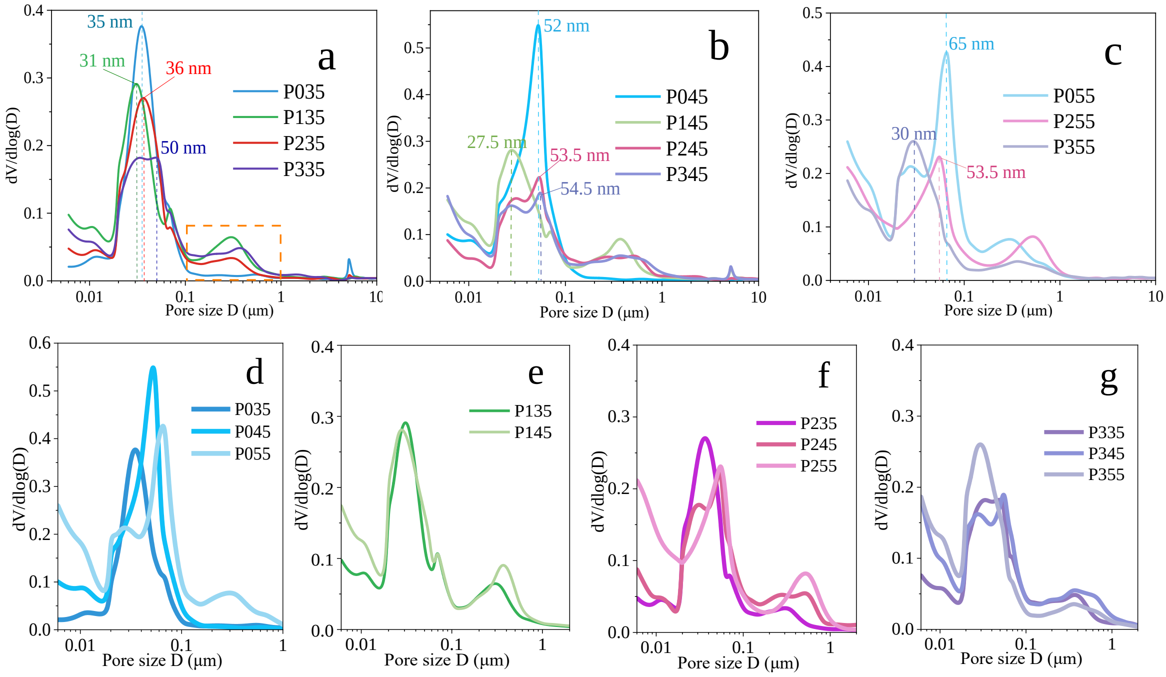

Figure 5.4. Pore size distribution of pastes measured by MIP: the comparison between pastes with *w/b* of 0.35 (a), 0.45 (b) and 0.55 (c); comparison between different *w/b* for OPC (d), the FA blended (e), the slag binary (f) and ternary (g).

FA decreases CP in pastes with *w/b* of 0.35 and 0.45 even under the sealed curing condition after 390 days. This is different to the reported results of the FA blended pastes cured up to 90 days in water [15,117]. However, SL increases the CP of pastes with *w/b* of 0.35 and 0.45. Therefore, the much lower D_v (Figure 5.2 and 5.3) of the blended pastes can hardly be ascribed to the reduction in CP compared with OPC, which was mentioned as the main reason for the low moisture diffusivity in the blended hcp [26,27]. SL might decrease the CP in pastes at later age when hcp was cured in water [15], since water curing can supply the sufficient water in the big capillary pores. The precipitation of hydration products can fill these big capillaries during later hydration of SL. However, the inner RH of the pastes is no more than 95% after 7 days even with the dilution effect from 50% SCMs [128] during the sealed curing condition.

When the effect from alkali ions on the equilibrium RH has been considered, vapor can only condense in the pores with diameter smaller than 70 nm in 95% RH at 20 °C [129] according to the Kelvin's equation. Consequently, the later age hydration of FA and SL can only occur in the mesopores (<50 nm) and middle capillary pores (50–100 nm) under the sealed curing condition. The filling effect from the hydrates at later age only happens in these small pores. This may explain the phenomenon that although the volume of small capillary pores (<100 nm) in the blended pastes is significantly lower than that in OPC (see Figure 5.4), there still exists a certain amount of large capillary pores (>100 nm) in the blended pastes due to the lack of liquid water. It might also be the reason to the differences in the effect of SL on the CP between water curing in [15] and sealed curing in this study. Although the total porosity in FA binary pastes is higher than that in OPC pastes, the main differences stay in the intrudable pores smaller than 100 nm.

5.5 Electrical properties of hcp

Table 5.1 presents the measured electrical conductivity of hcp, the conductivity of pore solution and inverse of F ($1/F$) of hcp after sealed curing for 1 year. The conductivity of pore solution was calculated by the empirical function in Table 4.1. The conductivity of pore solution in hcp stays in a wide range from 165 to 78 mS/cm due to the dilution effect from SCMs. It is apparent that the blending of SCMs decreases the conductivity of pore solution mainly due to the lower content of dissolvable alkali in SCMs compared with OPC. The increase of *w/b* from 0.35 to 0.55 in OPC paste induces the highest increment in the $1/F$ with a factor about 8 times compared with the blended pastes with the maximum factor about 3 times.

Table 5.1. the measured electrical conductivity of pastes, the calculated conductivity of pore solution and inverse of F in pastes at 1 year.

Sample	Electrical conductivity (mS/cm)		$1/F$
	Paste	Pore solution	
P035	0.251	165.9	1.52×10^{-03}
P045	0.701	131.3	5.34×10^{-03}
P055	1.249	102.9	1.21×10^{-02}
P135	0.019	104.4	1.78×10^{-04}
P145	0.026	96.0	2.71×10^{-04}
P235	0.075	149.6	4.98×10^{-04}
P245	0.128	114.5	1.12×10^{-03}
P255	0.167	111.6	1.50×10^{-03}
P335	0.070	133.3	5.26×10^{-04}
P345	0.085	86.9	9.75×10^{-04}
P355	0.111	78.0	1.42×10^{-03}

The evolution of pore connectivity index (β) in hcp follows the same trend as $1/F$ with respect to the change of *w/b* or binder type (see Figure 5.5). The blending of FA induces a large reduction in the $1/F$ with a normalized factor about 1/8.5 and 1/20 in paste compared with OPC with *w/b* of 0.35 and 0.45, respectively (see Table 5.1). SL blended hcps have a normalized factor about 1/3, 1/5 and 1/8 in the $1/F$ of hcp compared to OPC pastes with *w/b* of 0.35. 0.45 and 0.55, respectively. The ternary pastes with LL (P3-series) have the similar $1/F$ or β as the SL (P2-series) binary hcp. A significant increase in both $1/F$ and β can be observed as the *w/b* increases.

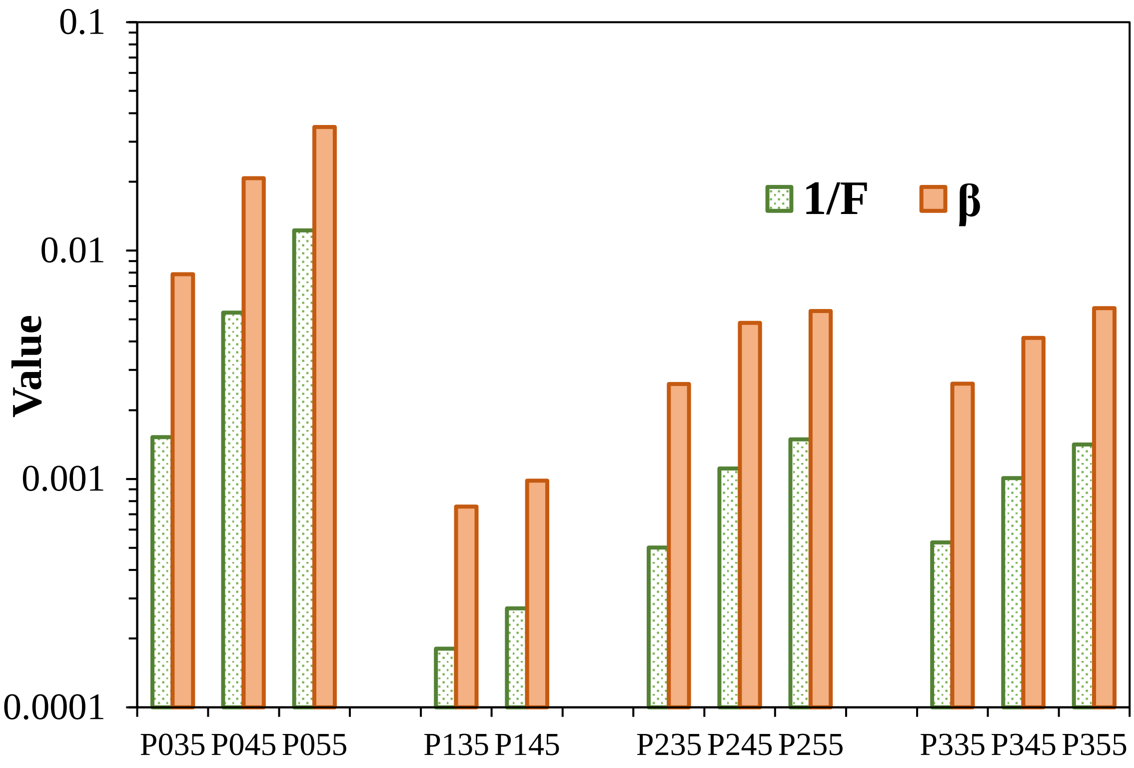

Figure 5.5. The inverse of *F* and pore connectivity index (*β*) of pastes cured for 1 year.

5.6 Discussion

5.6.1 Correlation between D_v and $D_{v,s}$

The cup method for measuring the D_v requires a long time to get the equilibrium for a constant flux (almost 6 months see Figure 5.1). The semi-infinite drying method is much faster than the cup method, but it relies heavily on the initial humidity control of the sample [130]. D_v from cup method may be comparable with the value calculated by using moisture content and the moisture transport coefficient (D_w) from semi-infinite drying method in certain RH intervals.

Figure 5.6 presents the correlation between D_v from the steady-state vapor diffusion test and $D_{v,s}$ from semi-infinite drying. D_v in the RH97–50 has a good linear correlation with the $D_{v,s}$ during drying at 50% RH with a line slope of 0.92 and R^2=0.96. However, the difference in the dependency on RH is evident when D_v and $D_{v,s}$ at the high RH condition is compared in Figure 5.6b. The correlation becomes weaker in the blended pastes (see the enlarged part) and the slope of the regression line goes much steeper compared with the data in Figure 5.6a. In one report from Nilsson [119], it is indicated that the D_v in the RH interval of 85–60% is comparable with $D_{v,s}$ during drying at 50% RH, which is consistent with our result in RH97–50 and drying at 50% RH. However, the difference in D_v and $D_{v,s}$ of the same hcp grows largely at the high moisture level (>75%).

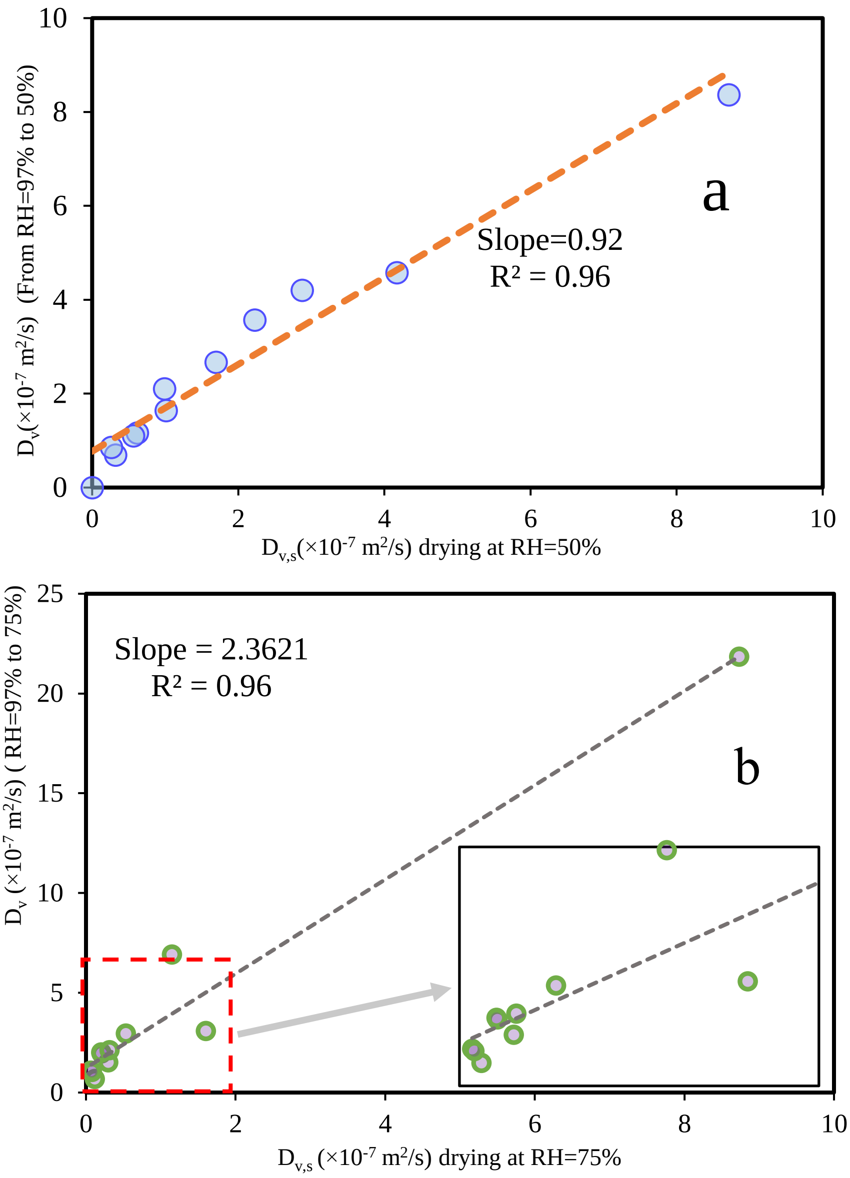

Figure 5.6. The correlation between average vapor diffusion coefficient (D_v) and $D_{v,s}$ from semi-infinite drying at 50% RH (a) and 75% RH (b).

5.6.2 Correlation between D_v and F

The correlation between D_v in different RH intervals and $1/F$ of hcp is separately plotted in Figure 5.7a–f, since the D_v in hcp is moisture dependent. It shows that there is a good linear correlation between D_v at RH97–75 with $1/F$ of hcp (see Figure 5.7a). This confirms that D_v at a high RH interval is determined by the pore connectivity instead of porosity. The enlarged plot shows that this linear correlation is general in both OPC and the blended pastes with R^2=0.985. Because the pore connectivity in the blended pastes is much lower than OPC pastes, the vapor diffusivity in the blended pastes is much lower than that in OPC pastes at the high RH intervals.

The linear correlation still exists between the $1/F$ and D_v at RH85–75 as shown in Figure 5.7c and d, but the blended pastes deviate from the general trend with a higher slope than the general line. The modelling results in Figure 5.2 indicates that the critical RH (φ_c) for the percolation of liquid in the blended pastes is much higher than that for OPC due to the differences in pore structure and alkali concentration in pore solution [24]. φ_c of OPC pastes is about 80–85%, so the volume of water in hcp at RH85–75 is sufficient to reach a percolation of liquid in OPC pastes. As the RH intervals decreases to RH97–50, the connectivity of liquid phase in the pores evidently declines so that the liquid can not reach a percolation condition. Therefore, the moisture transport process seems to be mainly determined by the porosity (see Figure A5-c) instead of F.

The blended pastes have the D_v close to OPC with the same *w/b* in RH75–50 (see Figure 5.2), even though the 1/F or β of the blended pastes is much lower than that of OPC (Figure 5.5). The slope of the regression line in the blended hcp increases with the decrease of RH, as the major determinant of D_v transits from pore connectivity to porosity. FA pastes with *w/b* of 0.45 even deviates from the fitting line of the blended pastes due to its much lower pore connectivity compared with the SL blended hcp.

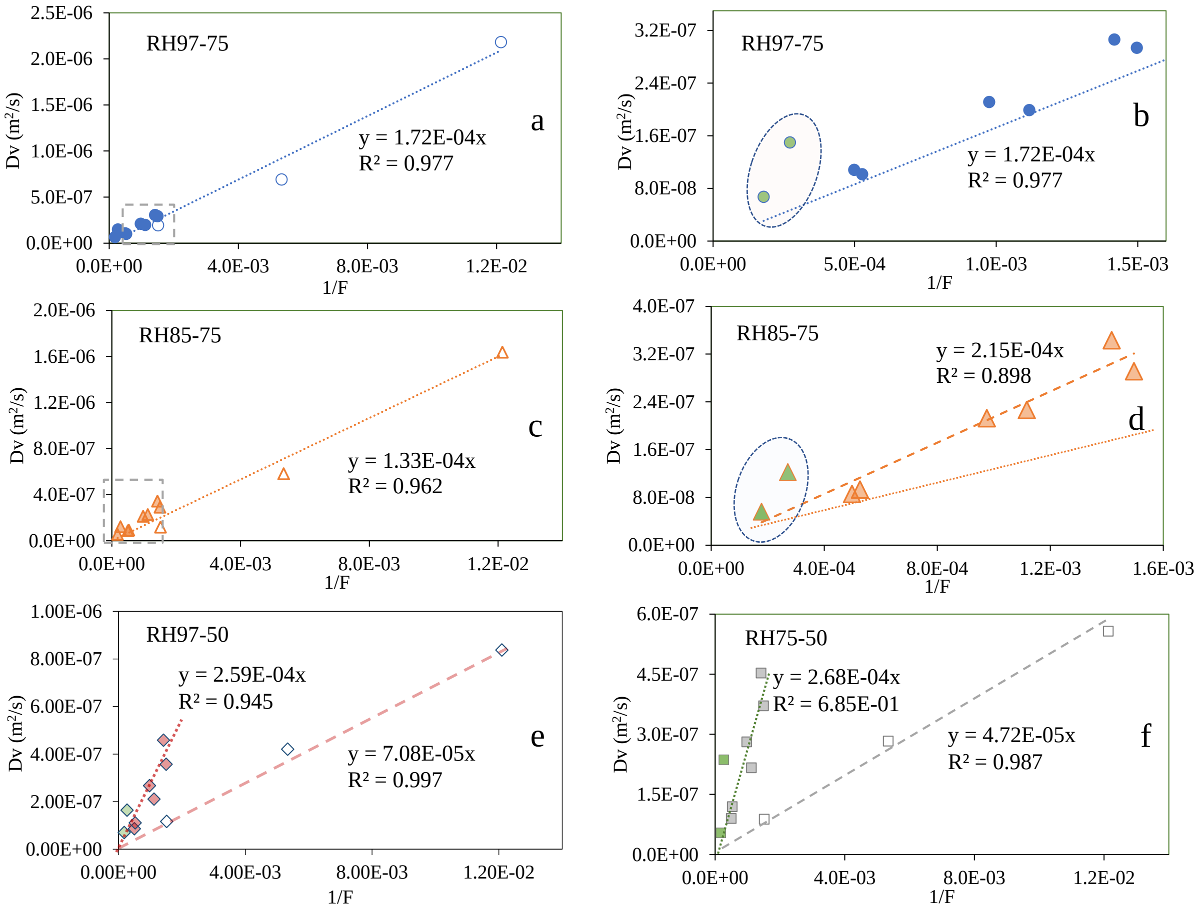

Figure 5.7. The correlation between average vapor diffusion coefficient and 1/F: a and b-D_v in RH97–75; c and d-D_v in RH85–75; e- D_v in RH97–50; f- D_v in RH75–50. The hollow scatters are the data of OPC, the solid scatters are the data of the blended pastes and the scatters filled with green color is FA blended pastes.

5.6.3 Relationship between D_{RCM}, D_v and 1/F

Although the D_{RCM} and D_v of hcp was measured at different curing ages, we can still observe a correlation between D_v in hcp cured for 390 days and D_{RCM} of hcp cured for 90 days in Figure 5.8. There is no general correlation in OPC and the blended pastes, but the linear correlation is clear between D_{RCM} and D_v in OPC pastes in different RH intervals. The enlarged window shows that a good linear correlation between D_v at RH 97–50 and D_{RCM} in the blended pastes. It implies that some further hydration may occur after 90 days, but the differences in the pore connectivity or F of the blended and OPC pastes may maintain in the same magnitude.

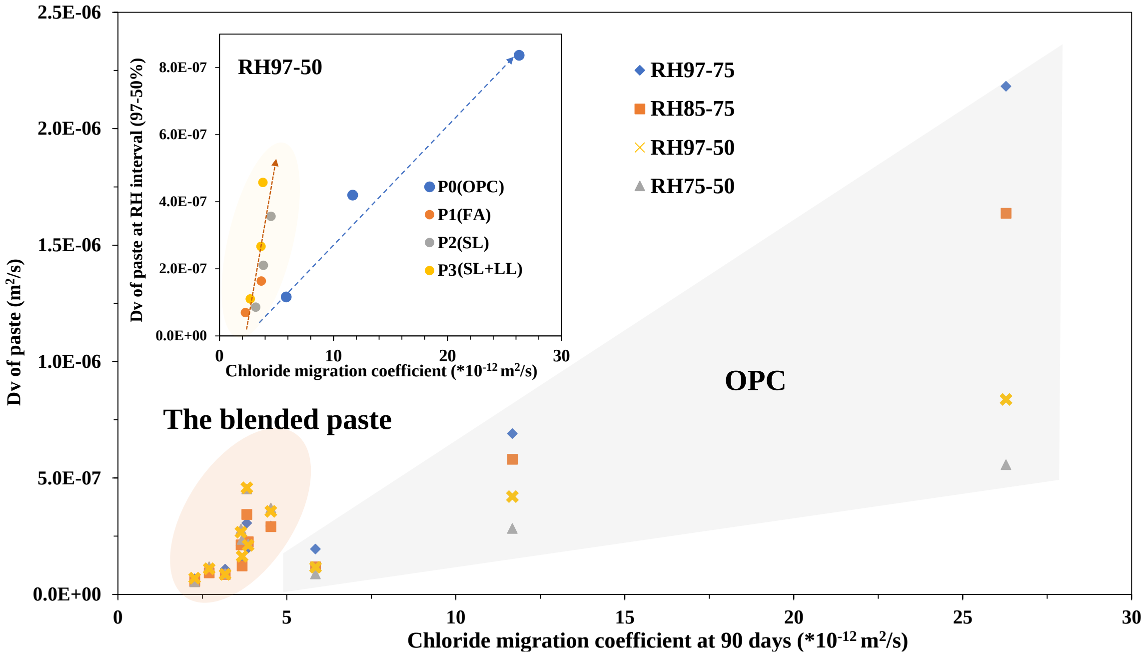

Figure 5.8. The correlation between D_v in hcp cured for 390 days and D_{RCM} of hcp cured for 90 days.

Given that the binding capacity of Cl in the hydration products can be neglected during the non-steady-state migration test under the applied electric field, Eq. 5.13 can be used to estimate the D_{RCM} based on F. D_0 is the chloride migration coefficient in the bulk pore solution, which was often assumed to be 2.03×10^{-9} (m²/s) [110], but it could be smaller than this value due to the interaction with other ions in the pore solution.

$$D_{RCM} = \frac{D_0}{F} \tag{5.13}$$

Chidiac and Shafikhani [24] developed an similar model to estimate the chloride migration coefficient based on the measured electrical conductivity of concrete and the calculated conductivity of pore solution. Figure 5.9 shows the relationship between the D_{RCM} and the 1/F (calculated from data in Table A3) and the data in [24] normalized to the volume of mortar. D_{RCM} of all the pastes generally locates close to the modelled line (dash line in Figure 5.9a), but the data of hcp with *w/b* of 0.35 deviate from the modelled line when we focus on the low D_{RCM} region (see Figure 5.9b). The hcp with *w/b* of 0.35 is far from the saturation state under this curing condition. The conductivity of hcp was measured under the sealed curing condition, but D_{RCM} was tested under the nearly saturated condition which might result in a deeper chloride penetration depth or higher value of D_{RCM} compared to the sealed curing condition. The data from [24] at 84 days and 1 year also locate close to the modelled line. Therefore, the pore connectivity or *F* of hcp should be a key controlling factor on the chloride migration in the OPC-based materials under an applied electric field.

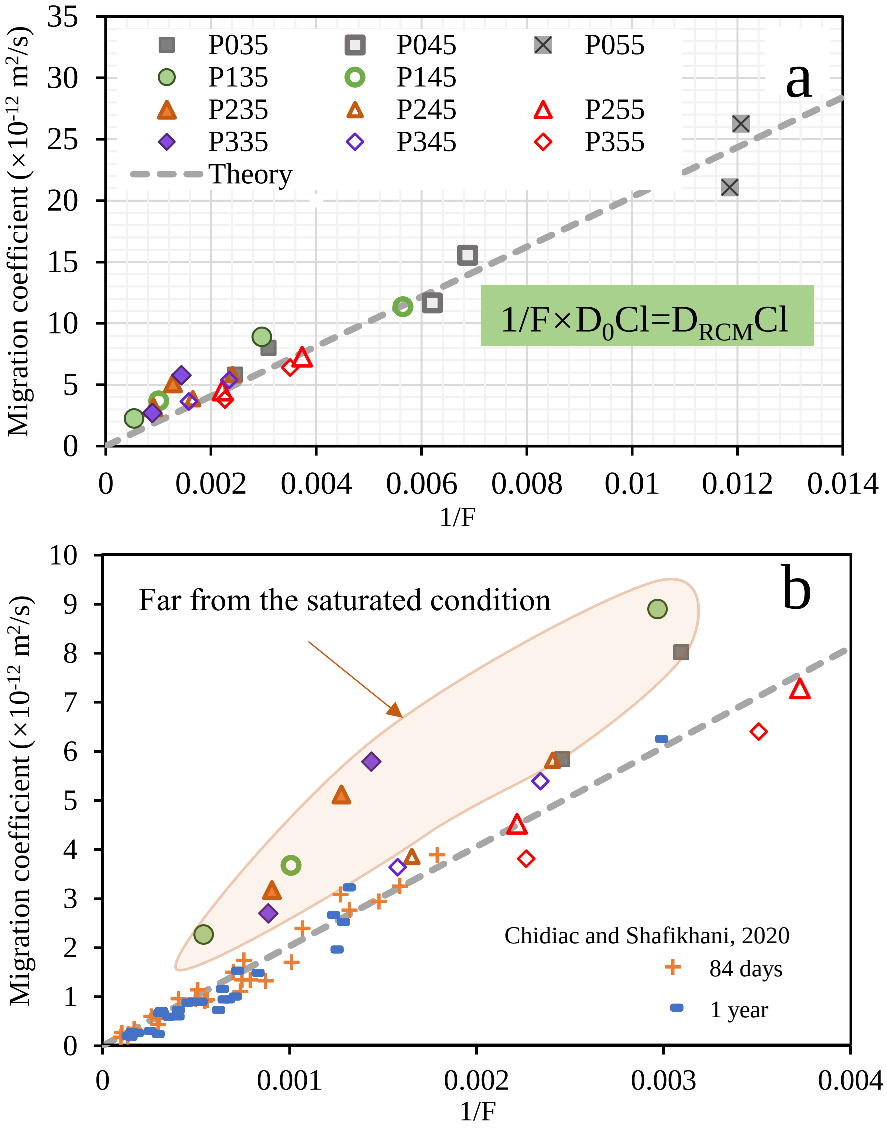

Figure 5.9. The correlation between chloride migration coefficient and 1/*F*: a- data in this study at curing time of 28 and 90 days; b- data in [24] was used and adopted after some calculation.

5.7 Summary

D_v of hcp is dependent on moisture content due to the condensation of water in the porous structure of hcp. The φ_c for the percolation of liquid in blended pastes is almost 95%, which is much higher than that of OPC with about 80%. Because the blended pastes have a more complex pore structure and the lower alkali ions in pore solution than OPC pastes. This causes a relatively stable D_v of the blended pastes in the RH lower than 85%.

FA lowers the CP of pastes after 390-day curing, but SL have no reducing effect on the CP of the pastes. Both FA and SL have a great reducing effect on the pore connectivity in the pastes after a long-term curing. The ternary pastes with LL have the similar F with the SL blended pastes after 1 year. The higher w/b produces more water for the later age hydration of FA and SL, so that their refinement effect on pore structure becomes more evident. Therefore, an increase in w/b augments the effect of SCMs on the moisture transport and chloride migration coefficient in hcp.

D_v is comparable with $D_{v,s}$ of hcp drying at the low RH condition (~50%), but the difference largely expand at a high RH. Both F and porosity of small pores (middle capillary and mesopores) determine the moisture transport properties in the hcp. However, F is the major determinant for the moisture transport process at a high RH interval. The porosity of small pores stands for the major determinant at a low RH interval. A highly simplified model was developed to estimate the chloride migration coefficient with only one measurable parameter F of hcp. This model is valid to calculate the D_{RCM} of both plain and the blended pastes/mortars.

6 Conclusions and future research work

6.1 Conclusions

The presences of alkali salts and SCMs in binders influence the bottom-up structure building process during hydration. The effect of SCMs on water accessible porosity and pore connectivity in hcp can be detected in the change of electrical conductivity hcp. Therefore, an in-situ monitoring of electrical conductivity in pastes is an effective way to determine the structure growth in hcp during hydration. The moisture and chloride transports are mainly controlled by the pore structure in hcp. The formation factor (*F*) calculated based on the conductivity test provides a more effective index for estimation of the moisture transport properties at high RH conditions than the parameters of pore structure by MIP.

The precipitation of hydration products for building up the initial structure is a nonclassical nucleation of C-S-H. It starts with nucleation of primary globule flocs and is then followed by the growth from particle attachment. The presence of Al ions and alkali salts influence the attachment of flocs. KOH and K_2SO_4 have an impact on the size of primary flocs and growth of C-S-H strips, so that they change both the chemical structure and pore structure in hcp after long-term hydration. A five-stage hypothesis can clarify the mechanism for the early hydration process, that is: Stage I, Fast dissolution; Stage II, Approaching dissolution equilibrium; Stage III, New surface equilibrium; Stage IV, Surface nucleation; and Stage V, Attachment to growth.

The electrical conductivity in pastes is determined by the change of ion concentration in pore solution and structure build-up during the chemical reaction process. The *w/b* has a large effect on the conductivity of pastes. The results indicate that the differences in *F* of hcp mainly derive from the huge differences in the pore connectivity. The conductivity of pore solution in hcp can effectively be calculated based on the chemical composition of binders and content of Epw in pastes. An increase in *w/b* reduces the conductivity of pore solution, but it increases the connectivity of pore solution to reduce the *F*. The growth rate of *F* is a good index for indicating the reactivity of SCMs. SCMs reduce the conductivity of paste at the early age mainly due to its dilution effect. SL has a weaker reduction in conductivity of pore solution than FA. SCMs refine the pore structure to lower the connectivity of pores in hcp. LL increases the connectivity of pores, but its filling effect is evident after a certain age.

An extended percolation theory is effective to describe the relationship between volume of evaporable water (Epw) and *F*. It provides the theory support for analyzing the data from a real-time monitoring of electrical conductivity in cement-based materials. his study provides a cheap but valid method to detect the meaningful data for the prediction and simulation of moisture and chloride transports in concrete during its service life with a continuous long-term hydration.

The moisture transport properties in hcp are RH dependent due to the gradual condensation of water with the increase of RH. The critical RH (φ_c) for the percolation of liquid phase in blended pastes is much higher than that for OPC pastes. Because the blended pastes have a refined pore structure and the modified pore solution, D_v in the blended pastes keeps almost constant in the RH lower than 85%. The critical entry pore size from MIP (CP) is not the controlling factor for the vapor diffusion in hcp. Although FA decreases the CP in pastes after long-term curing, SL have no such effect on the CP of the pastes. Both FA and SL have a great reducing effect on the pore connectivity, so they bring huge decrease in the D_v of pastes at high RH condition. A further replacement of LL has no reducing effect on the pore connectivity in hcp. An increase in *w/b* supplies more content of water for the later age hydration of FA and SL, so the refinement effect on pore structure becomes more evident at the higher *w/b*. This phenomenon is also obvious in its effect on the moisture transport and chloride migration coefficient.

Both the tube method and the semi-infinite drying can test the moisture transport in hcp. D_v is comparable with $D_{v,s}$ when the hcp was dried at the low RH condition (~50%), but the differences between D_v and $D_{v,s}$ will expand at the high RH condition. The connectivity of pores is the major determinant for the moisture transport in hcp at a high RH, but the percentage of small pores controls the vapor diffusion at a low RH. The highly simplified model developed in this study is valid to model D_{RCM} of both plain and the blended pastes/mortars.

6.2 Future research work

The electrical conductivity test is a very effective method to measure the moisture distribution in hcp. The main purpose of the project is to develop a method for assessing the moisture transport in the blended concrete, and a device based on the conductivity monitoring may fulfill this target. Therefore, a clear correlation between the moisture content and conductivity in concrete is one main topic in further research based on the theory applied in this study.

The later age hydration of SCMs makes impact on their refinement effect on the pore structure in hcp, thus inducing different level of effect on the moisture and ion transport. Therefore, it is significant to perform a further investigation on the pore structure and spatial distribution of hydration products in hcp cured at different conditions. This will be studied by the experimental measurements (such as, SEM, BET and TGA) to reveal the differences in the phase assemblage and pore distribution in hcp with SCMs after different long-term curing.

Experimental results in this study provide the abundant data to build the model for moisture transport based on pore size distribution or pore network in the blended pastes. The moisture transport and fixation model based on pore structure is another topic for the future research, so that the moisture content and diffusion in modern concrete can be predicted based on pore structure.

One target of this project is to describe the chemically bound water and its stability in the main hydration products in the blended pastes, so the modelling of structure feature of C-A-S-H with different Ca/Si and H_2O/Si ratio is also one of the main future works from fundamental research aspect.

References

[1] M. Schneider, The cement industry on the way to a low-carbon future, Cem. Concr. Res. 124 (2019) 105792. https://doi.org/10.1016/j.cemconres.2019.105792.

[2] C. OECD/IEA, Low-carbon Transition in the Cement Industry: Technology Roadmap, Int. Energy Agency IEA Paris. (2019). https://webstore.iea.org/technology-roadmap-low-carbontransition-in-the-cement-industry. (accessed October 5, 2019).

[3] S.J. Davis, N.S. Lewis, M. Shaner, S. Aggarwal, D. Arent, I.L. Azevedo, et al., Net-zero emissions energy systems, Science. 360 (2018) eaas9793. https://doi.org/10.1126/science.aas9793.

[4] R.M. Andrew, Global CO2 emissions from cement production, Earth Syst Sci Data. 10 (2018) 195–217. https://doi.org/10.5194/essd-10-195-2018.

[5] L. Huang, W. Song, H. Li, H. Zhang, Z. Yang, Effects of aphthitalite on the formation of clinker minerals and hydration properties, Constr. Build. Mater. 183 (2018) 275–282. https://doi.org/10.1016/j.conbuildmat.2018.06.082.

[6] A. Chatterjee, T. Sui, Alternative fuels – Effects on clinker process and properties, Cem. Concr. Res. 123 (2019) 105777. https://doi.org/10.1016/j.cemconres.2019.105777.

[7] P.J.M. Monteiro, S.A. Miller, A. Horvath, Towards sustainable concrete, Nat. Mater. 16 (2017) 698–699. https://doi.org/10.1038/nmat4930.

[8] S. Joseph, R. Snellings, Ö. Cizer, Activation of Portland cement blended with high volume of fly ash using Na2SO4, Cem. Concr. Compos. 104 (2019) 103417.

[9] L. Huang, W. Song, H. Li, H. Zhang, Z. Yang, Effects of aphthitalite on the formation of clinker minerals and hydration properties, Constr. Build. Mater. 183 (2018) 275–282.

[10] L. Huang, Z. Yang, Early hydration of tricalcium silicate with potassium hydroxide and sulfate from pore solution and solid view, Constr. Build. Mater. 230 (2020) 116988.

[11] L. Huang, L. Tang, H. Gu, Z. Li, Z. Yang, New insights into the reaction of tricalcium silicate (C_3S) with solutions to the end of the induction period, Cem. Concr. Res. 152 (2022) 106688. https://doi.org/10.1016/j.cemconres.2021.106688.

[12] I. Jawed, J. Skalny, Alkalies in cement: A review, Cem. Concr. Res. 8 (1978) 37–51. https://doi.org/10.1016/0008-8846(78)90056-X.

[13] S. Adu-Amankwah, M. Zajac, C. Stabler, B. Lothenbach, L. Black, Influence of limestone on the hydration of ternary slag cements, Cem. Concr. Res. 100 (2017) 96–109. https://doi.org/10.1016/j.cemconres.2017.05.013.

[14] B. Mota, T. Matschei, K. Scrivener, The influence of sodium salts and gypsum on alite hydration, Cem. Concr. Res. 75 (2015) 53–65.

[15] E. Berodier, K. Scrivener, Evolution of pore structure in blended systems, Cem. Concr.

Res. 73 (2015) 25–35.

[16] P. Duan, Z. Shui, W. Chen, C. Shen, Effects of metakaolin, silica fume and slag on pore structure, interfacial transition zone and compressive strength of concrete, Constr. Build. Mater. 44 (2013) 1–6.

[17] V.Z. Zadeh, C.P. Bobko, Nanoscale mechanical properties of concrete containing blast furnace slag and fly ash before and after thermal damage, Cem. Concr. Compos. 37 (2013) 215–221.

[18] C. Hu, Z. Li, Property investigation of individual phases in cementitious composites containing silica fume and fly ash, Cem. Concr. Compos. 57 (2015) 17–26.

[19] W. Wilson, L. Sorelli, A. Tagnit-Hamou, Unveiling micro-chemo-mechanical properties of C–(A)–S–H and other phases in blended-cement pastes, Cem. Concr. Res. 107 (2018) 317–336.

[20] H.M. Jennings, A model for the microstructure of calcium silicate hydrate in cement paste, Cem. Concr. Res. 30 (2000) 101–116. https://doi.org/10.1016/S0008-8846(99)00209-4.

[21] A.J. Allen, J.J. Thomas, Analysis of C–S–H gel and cement paste by small-angle neutron scattering, Cem. Concr. Res. 37 (2007) 319–324. https://doi.org/10.1016/j.cemconres.2006.09.002.

[22] H.M. Jennings, Refinements to colloid model of C-S-H in cement: CM-II, Cem. Concr. Res. 38 (2008) 275–289. https://doi.org/10.1016/j.cemconres.2007.10.006.

[23] P. Mehta, P. Monteiro, Concrete: microstructure, properties, and materials, McGraw-Hill Education, 2014.

[24] S.E. Chidiac, M. Shafikhani, Electrical resistivity model for quantifying concrete chloride diffusion coefficient, Cem. Concr. Compos. 113 (2020) 103707. https://doi.org/10.1016/j.cemconcomp.2020.103707.

[25] P. Halamickova, R.J. Detwiler, D.P. Bentz, E.J. Garboczi, Water permeability and chloride ion diffusion in portland cement mortars: Relationship to sand content and critical pore diameter, Cem. Concr. Res. 25 (1995) 790–802. https://doi.org/10.1016/0008-8846(95)00069-O.

[26] N. Olsson, L.-O. Nilsson, M. Åhs, V. Baroghel-Bouny, Moisture transport and sorption in cement based materials containing slag or silica fume, Cem. Concr. Res. 106 (2018) 23–32. https://doi.org/10.1016/j.cemconres.2018.01.018.

[27] O. Linderoth, P. Johansson, L. Wadsö, Development of pore structure, moisture sorption and transport properties in fly ash blended cement-based materials, Constr. Build. Mater. 261 (2020) 120007. https://doi.org/10.1016/j.conbuildmat.2020.120007.

[28] E. Astm, Standard test methods for water vapor transmission of materials, ASTM Int. West Conshohocken PA. (96).

[29] V. Baroghel-Bouny, Water vapour sorption experiments on hardened cementitious materials. Part II: Essential tool for assessment of transport properties and for durability prediction, Cem. Concr. Res. 37 (2007) 438–454. https://doi.org/10.1016/j.cemconres.2006.11.017.

[30] B. Sioulas, J.G. Sanjayan, The coloration phenomenon associated with slag blended cements, Cem. Concr. Res. 31 (2001) 313–320. https://doi.org/10.1016/S0008-8846(00)00371-9.

[31] J.D. Rhoades, P.A.C. Raats, R.J. Prather, Effects of liquid-phase electrical conductivity, water content, and surface conductivity on bulk soil electrical conductivity, Soil Sci. Soc. Am. J. 40 (1976) 651–655. https://doi.org/10.2136/sssaj1976.03615995004000050017x.

[32] L. Greenspan, Humidity fixed points of binary saturated aqueous solutions, J. Res. Natl. Bur. Stand. Sect. Phys. Chem. 81A (1977) 89. https://doi.org/10.6028/jres.081A.011.

[33] Z. Zhang, G.W. Scherer, Physical and chemical effects of isopropanol exchange in cement-based materials, Cem. Concr. Res. 145 (2021) 106461. https://doi.org/10.1016/j.cemconres.2021.106461.

[34] J. Bensted, Hydration of Portland Cement, in: Adv. Cem. Technol., Elsevier, 1983: pp. 307–347. https://doi.org/10.1016/B978-0-08-028670-9.50015-6.

[35] K. Scrivener, Advances in understanding cement hydration mechanisms, Cem. Concr. Res. 124 (2019) 105823. https://doi.org/10.1016/j.cemconres.2019.105823.

[36] H.M. Jennings, P.L. Pratt, An experimental argument for the existence of a protective membrane surrounding portland cement during the induction period, Cem. Concr. Res. 9 (1979) 501–506. https://doi.org/10.1016/0008-8846(79)90048-6.

[37] P. Juilland, L. Nicoleau, R.S. Arvidson, E. Gallucci, Advances in dissolution understanding and their implications for cement hydration, RILEM Tech. Lett. 2 (2017) 90–98. https://doi.org/10.21809/rilemtechlett.2017.47.

[38] D. Marchon, P. Juilland, E. Gallucci, L. Frunz, R.J. Flatt, Molecular and submolecular scale effects of comb-copolymers on tri-calcium silicate reactivity: Toward molecular design, J. Am. Ceram. Soc. 100 (2017) 817–841. https://doi.org/10.1111/jace.14695.

[39] J.F. Young, A review of the mechanisms of set-retardation in portland cement pastes containing organic admixtures, Cem. Concr. Res. 2 (1972) 415–433. https://doi.org/10.1016/0008-8846(72)90057-9.

[40] J.W. Bullard, R.J. Flatt, New insights into the effect of calcium hydroxide precipitation on the kinetics of tricalcium silicate hydration, J. Am. Ceram. Soc. 93 (2010) 1894–1903. https://doi.org/10.1111/j.1551-2916.2010.03656.x.

[41] X. Kong, S. Emmerling, J. Pakusch, M. Rueckel, J. Nieberle, Retardation effect of styrene-acrylate copolymer latexes on cement hydration, Cem. Concr. Res. 75 (2015) 23–41. https://doi.org/10.1016/j.cemconres.2015.04.014.

[42] C. Nalet, A. Nonat, Effects of hexitols on the hydration of tricalcium silicate, Cem. Concr. Res. 91 (2017) 87–96. https://doi.org/10.1016/j.cemconres.2016.11.004.

[43] B. Mota, T. Matschei, K. Scrivener, The influence of sodium salts and gypsum on alite hydration, Cem. Concr. Res. 75 (2015) 53–65. https://doi.org/10.1016/j.cemconres.2015.04.015.

[44] A. Ouzia, K. Scrivener, The needle model: A new model for the main hydration peak of alite, Cem. Concr. Res. 115 (2019) 339–360. https://doi.org/10.1016/j.cemconres.2018.08.005.

[45] E.M.J. Bérodier, A.C.A. Muller, K.L. Scrivener, Effect of sulfate on C-S-H at early age, Cem. Concr. Res. 138 (2020) 106248. https://doi.org/10.1016/j.cemconres.2020.106248.

[46] J.J. De Yoreo, P.U.P.A. Gilbert, N.A.J.M. Sommerdijk, R.L. Penn, S. Whitelam, D. Joester, et al., Crystallization by particle attachment in synthetic, biogenic, and geologic environments, Science. 349 (2015) aaa6760–aaa6760. https://doi.org/10.1126/science.aaa6760.

[47] V.I. Kalikmanov, Classical Nucleation Theory, in: V.I. Kalikmanov (Ed.), Nucleation Theory, Springer Netherlands, Dordrecht, 2013: pp. 17–41. https://doi.org/10.1007/978-90-481-3643-8_3.

[48] A.E.S. Van Driessche, L.G. Benning, J.D. Rodriguez-Blanco, M. Ossorio, P. Bots, J.M. García-Ruiz, The Role and Implications of Bassanite as a Stable Precursor Phase to Gypsum Precipitation, Science. 336 (2012) 69–72. https://doi.org/10.1126/science.1215648.

[49] D. Li, M.H. Nielsen, J.R.I. Lee, C. Frandsen, J.F. Banfield, J.J. De Yoreo, Direction-specific interactions control crystal growth by oriented attachment, Science. 336 (2012) 1014–1018. https://doi.org/10.1126/science.1219643.

[50] A.F. Wallace, L.O. Hedges, A. Fernandez-Martinez, P. Raiteri, J.D. Gale, G.A. Waychunas, ET AL., Microscopic evidence for liquid-liquid separation in supersaturated $CaCO_3$ solutions, Science. 341 (2013) 885–889. https://doi.org/10.1126/science.1230915.

[51] A.I. Lupulescu, J.D. Rimer, In situ imaging of silicalite-1 surface growth reveals the mechanism of crystallization, Science. 344 (2014) 729–732. https://doi.org/10.1126/science.1250984.

[52] E. Pustovgar, R.P. Sangodkar, A.S. Andreev, M. Palacios, B.F. Chmelka, R.J. Flatt, et al., Understanding silicate hydration from quantitative analyses of hydrating tricalcium silicates, Nat. Commun. 7 (2016) 10952. https://doi.org/10.1038/ncomms10952.

[53] G. Mirabello, A. Ianiro, P.H.H. Bomans, T. Yoda, A. Arakaki, H. Friedrich, et al., Crystallization by particle attachment is a colloidal assembly process, Nat. Mater. 19 (2020) 391–396. https://doi.org/10.1038/s41563-019-0511-4.

[54] N. Krautwurst, L. Nicoleau, M. Dietzsch, I. Lieberwirth, C. Labbez, A. Fernandez-

Martinez, et al., Two-Step Nucleation Process of Calcium Silicate Hydrate, the Nanobrick of Cement, Chem. Mater. 30 (2018) 2895–2904. https://doi.org/10.1021/acs.chemmater.7b04245.

[55] F. Bellmann, D. Damidot, B. Möser, J. Skibsted, Improved evidence for the existence of an intermediate phase during hydration of tricalcium silicate, Cem. Concr. Res. 40 (2010) 875–884. https://doi.org/10.1016/j.cemconres.2010.02.007.

[56] A.S. Brand, J.M. Gorham, J.W. Bullard, Dissolution rate spectra of β-dicalcium silicate in water of varying activity, Cem. Concr. Res. 118 (2019) 69–83. https://doi.org/10.1016/j.cemconres.2019.02.014.

[57] M. Boström, D.R.M. Williams, B.W. Ninham, Specific ion effects: Why DLVO theory fails for biology and colloid systems, Phys. Rev. Lett. 87 (2001) 168103. https://doi.org/10.1103/PhysRevLett.87.168103.

[58] P.M. Dove, N. Han, Kinetics of mineral dissolution and growth as reciprocal microscopic surface processes across chemical driving force, in: AIP Conf. Proc., AIP, Park City, Utah (USA), 2007: pp. 215–234. https://doi.org/10.1063/1.2751917.

[59] J. Nehring, D. Jansen, J. Neubauer, F. Goetz-Neunhoeffer, Hydration of C_3S in presence of CA : Mineral-pore solution interaction, J. Am. Ceram. Soc. 102 (2019) 3152–3162. https://doi.org/10.1111/jace.16197.

[60] F. Bellmann, H.-M. Ludwig, Analysis of aluminum concentrations in the pore solution during hydration of tricalcium silicate, Cem. Concr. Res. 95 (2017) 84–94. https://doi.org/10.1016/j.cemconres.2017.02.020.

[61] O. Galkin, P.G. Vekilov, Direct Determination of the Nucleation Rates of Protein Crystals, J. Phys. Chem. B. 103 (1999) 10965–10971. https://doi.org/10.1021/jp992786x.

[62] B. Fritz, C. Noguera, Mineral Precipitation Kinetics, Rev. Mineral. Geochem. 70 (2009) 371–410. https://doi.org/10.2138/rmg.2009.70.8.

[63] A.F. Wallace, J.J. DeYoreo, P.M. Dove, Kinetics of silica nucleation on carboxyl- and amine-terminated surfaces: insights for biomineralization, J. Am. Chem. Soc. 131 (2009) 5244–5250. https://doi.org/10.1021/ja809486b.

[64] E. Gartner, I. Maruyama, J. Chen, A new model for the C-S-H phase formed during the hydration of Portland cements, Cem. Concr. Res. 97 (2017) 95–106. https://doi.org/10.1016/j.cemconres.2017.03.001.

[65] G. Levita, A. Marchetti, G. Gallone, A. Princigallo, G.L. Guerrini, Electrical properties of fluidified Portland cement mixes in the early stage of hydration, Cem. Concr. Res. 30 (2000) 923–930. https://doi.org/10.1016/S0008-8846(00)00282-9.

[66] A. Princigallo, K. van Breugel, G. Levita, Influence of the aggregate on the electrical conductivity of Portland cement concretes, Cem. Concr. Res. 33 (2003) 1755–1763. https://doi.org/10.1016/S0008-8846(03)00166-2.

[67] M. Heikal, M.S. Morsy, M.M. Radwan, Electrical conductivity and phase composition of calcium aluminate cement containing air-cooled and water-cooled slag at 20, 40 and 60 °C, Cem. Concr. Res. 35 (2005) 1438–1446. https://doi.org/10.1016/j.cemconres.2004.09.027.

[68] N. Schwarz, M. DuBois, N. Neithalath, Electrical conductivity based characterization of plain and coarse glass powder modified cement pastes, Cem. Concr. Compos. 29 (2007) 656–666. https://doi.org/10.1016/j.cemconcomp.2007.05.005.

[69] A.L.G. Gastaldini, G.C. Isaia, T.F. Hoppe, F. Missau, A.P. Saciloto, Influence of the use of rice husk ash on the electrical resistivity of concrete: A technical and economic feasibility study, Constr. Build. Mater. 23 (2009) 3411–3419. https://doi.org/10.1016/j.conbuildmat.2009.06.039.

[70] T.M. Chrisp, G. Starrs, W.J. Mccarter, E. Rouchotas, J. Blewett, Temperature-conductivity relationships for concrete: An activation energy approach, J. Mater. Sci. Lett. 20 (2001) 1085–1087.

[71] M. Heikal, M.S. Morsy, I. Aiad, Effect of treatment temperature on the early hydration characteristics of superplasticized silica fume blended cement pastes, Cem. Concr. Res. 35 (2005) 680–687. https://doi.org/10.1016/j.cemconres.2004.06.012.

[72] W.J. Weiss, C. Qiao, B. Isgor, J. Olek, Implementing rapid durability measure for concrete using resistivity and formation factor, (2020) 25. (Joint Transportation Research Program Publication No. FHWA/IN/JTRP-2020/08). West Lafayette, IN: Purdue University. https://doi.org/10.5703/1288284317120.

[73] K.A. Snyder, X. Feng, B.D. Keen, T.O. Mason, Estimating the electrical conductivity of cement paste pore solutions from OH^-, K^+ and Na^+ concentrations, Cem. Concr. Res. 33 (2003) 793–798. https://doi.org/10.1016/S0008-8846(02)01068-2.

[74] R. Spragg, C. Villani, K. Snyder, D. Bentz, J.W. Bullard, J. Weiss, Factors that Influence Electrical Resistivity Measurements in Cementitious Systems, Transp. Res. Rec. J. Transp. Res. Board. 2342 (2013) 90–98. https://doi.org/10.3141/2342-11.

[75] H.W. Whittington, J. McCarter, M.C. Forde, The conduction of electricity through concrete, Mag. Concr. Res. 33 (1981) 48–60. https://doi.org/10.1680/macr.1981.33.114.48.

[76] L. Xiao, Z. Li, Early-age hydration of fresh concrete monitored by non-contact electrical resistivity measurement, Cem. Concr. Res. 38 (2008) 312–319. https://doi.org/10.1016/j.cemconres.2007.09.027.

[77] X. Wei, L. Xiao, Z. Li, Prediction of standard compressive strength of cement by the electrical resistivity measurement, Constr. Build. Mater. 31 (2012) 341–346. https://doi.org/10.1016/j.conbuildmat.2011.12.111.

[78] A. Lübeck, A.L.G. Gastaldini, D.S. Barin, H.C. Siqueira, Compressive strength and electrical properties of concrete with white Portland cement and blast-furnace slag, Cem. Concr. Compos. 34 (2012) 392–399.

https://doi.org/10.1016/j.cemconcomp.2011.11.017.

[79] Q. Gui, M. Qin, K. Li, Gas permeability and electrical conductivity of structural concretes: Impact of pore structure and pore saturation, Cem. Concr. Res. 89 (2016) 109–119. https://doi.org/10.1016/j.cemconres.2016.08.009.

[80] W. Wilson, F. Georget, K. Scrivener, Unravelling chloride transport/microstructure relationships for blended-cement pastes with the mini-migration method, Cem. Concr. Res. 140 (2021) 106264. https://doi.org/10.1016/j.cemconres.2020.106264.

[81] J.I. Escalante-García, J.H. Sharp, Effect of temperature on the hydration of the main clinker phases in portland cements: part ii, blended cements, Cem. Concr. Res. 28 (1998) 1259–1274. https://doi.org/10.1016/S0008-8846(98)00107-0.

[82] J.I. Escalante-Garcia, Nonevaporable water from neat OPC and replacement materials in composite cements hydrated at different temperatures, Cem. Concr. Res. 33 (2003) 1883–1888. https://doi.org/10.1016/S0008-8846(03)00208-4.

[83] F.W. Locher, Cement: principles of production and use, Verlag Bau$^+$ Technik, 2013.

[84] L.J. Struble, The influence of cement pore solution on alkali-silica reaction, Ph.D. thesis, Purdue University, 1987.

[85] A. Vollpracht, B. Lothenbach, R. Snellings, J. Haufe, The pore solution of blended cements: a review, Mater. Struct. 49 (2016) 3341–3367. https://doi.org/10.1617/s11527-015-0724-1.

[86] J. Bockris, Modern Electrochemistry: An Introduction to an Interdisciplinary Area Volume 1, Springer Science & Business Media, 2012.

[87] J. Johnston, The change of the equivalent conductance of ions with the temperature, J. Am. Chem. Soc. 31 (1909) 1010–1020. https://doi.org/10.1021/ja01939a003.

[88] A. Schöler, B. Lothenbach, F. Winnefeld, M.B. Haha, M. Zajac, H.-M. Ludwig, Early hydration of SCM-blended Portland cements: A pore solution and isothermal calorimetry study, Cem. Concr. Res. 93 (2017) 71–82. https://doi.org/10.1016/j.cemconres.2016.11.013.

[89] F. Deschner, F. Winnefeld, B. Lothenbach, S. Seufert, P. Schwesig, S. Dittrich, F. Goetz-Neunhoeffer, J. Neubauer, Hydration of Portland cement with high replacement by siliceous fly ash, Cem. Concr. Res. 42 (2012) 1389–1400. https://doi.org/10.1016/j.cemconres.2012.06.009.

[90] C. Shi, Effect of mixing proportions of concrete on its electrical conductivity and the rapid chloride permeability test (ASTM C1202 or ASSHTO T277) results, Cem. Concr. Res. 34 (2004) 537–545. https://doi.org/10.1016/j.cemconres.2003.09.007.

[91] G.E. Archie, The Electrical Resistivity Log as an Aid in Determining Some Reservoir Characteristics, Trans. AIME. 146 (1942) 54–62. https://doi.org/10.2118/942054-G.

[92] P.J. Tumidajski, A.S. Schumacher, S. Perron, P. Gu, J.J. Beaudoin, On the relationship

between porosity and electrical resistivity in cementitious systems, Cem. Concr. Res. 26 (1996) 539–544. https://doi.org/10.1016/0008-8846(96)00017-8.

[93] M.K. Moradllo, Relating formation factor of concrete to water absorption, ACI Mater. J. (2018) 13.

[94] G.W. Scherer, J. Zhang, J.A. Quintanilla, S. Torquato, Hydration and percolation at the setting point, Cem. Concr. Res. 42 (2012) 665-672.

[95] J. Zhang, E.A. Weissinger, S. Peethamparan, G.W. Scherer, Early hydration and setting of oil well cement, Cem. Concr. Res. 40 (2010) 1023–1033. https://doi.org/10.1016/j.cemconres.2010.03.014.

[96] E.J. Garboczi, Permeability, diffusivity, and microstructural parameters: A critical review, Cem. Concr. Res. 20 (1990) 591–601. https://doi.org/10.1016/0008-8846(90)90101-3.

[97] Z. Giergiczny, Fly ash and slag, Cem. Concr. Res. 124 (2019) 105826. https://doi.org/10.1016/j.cemconres.2019.105826.

[98] Y. Chen, I. Odler, On the origin of portland cement setting, Cem. Concr. Res. 22 (1992) 1130–1140. https://doi.org/10.1016/0008-8846(92)90042-T.

[99] R. Ylmén, U. Jäglid, B.-M. Steenari, I. Panas, Early hydration and setting of Portland cement monitored by IR, SEM and Vicat techniques, Cem. Concr. Res. 39 (2009) 433–439. https://doi.org/10.1016/j.cemconres.2009.01.017.

[100] R. Sriravindrarajah, R.N. Swamy, Development of a conductivity probe to monitor setting time and moisture movement in concrete, Cem. Concr. Aggreg. 4 (1982) 73–80.

[101] C. Villat, V.X. Tran, N. Pradelle-Plasse, P. Ponthiaux, F. Wenger, B. Grosgogeat, P. Colon, Impedance methodology: A new way to characterize the setting reaction of dental cements, Dent. Mater. 26 (2010) 1127–1132. https://doi.org/10.1016/j.dental.2010.07.013.

[102] İ.B. Topçu, T. Uygunoğlu, İ. Hocaoğlu, Electrical conductivity of setting cement paste with different mineral admixtures, Constr. Build. Mater. 28 (2012) 414–420. https://doi.org/10.1016/j.conbuildmat.2011.08.068.

[103] F. Rajabipour, J. Weiss, Electrical conductivity of drying cement paste, Mater. Struct. 40 (2007) 1143–1160. https://doi.org/10.1617/s11527-006-9211-z.

[104] D.L. Johnson, P.N. Sen, Dependence of the conductivity of a porous medium on electrolyte conductivity, Phys. Rev. B. 37 (1988) 3502–3510. https://doi.org/10.1103/PhysRevB.37.3502.

[105] A. Revil, P.W.J. Glover, Theory of ionic-surface electrical conduction in porous media, Phys. Rev. B. 55 (1997) 1757–1773. https://doi.org/10.1103/PhysRevB.55.1757.

[106] J.P. Straley, Critical phenomena in resistor networks, J. Phys. C Solid State Phys. 9 (1976) 783–795. https://doi.org/10.1088/0022-3719/9/5/017.

[107] I. Webman, J. Jortner, M.H. Cohen, Numerical simulation of continuous percolation conductivity, Phys. Rev. B. 14 (1976) 4737–4740. https://doi.org/10.1103/PhysRevB.14.4737.

[108] F. Leng, N. Feng, X. Lu, An experimental study on the properties of resistance to diffusion of chloride ions of fly ash and blast furnace slag concrete, Cem. Concr. Res. 30 (2000) 989–992. https://doi.org/10.1016/S0008-8846(00)00250-7.

[109] R.A. Meyers, Encyclopedia of physical science and technology, Academic, 2002.

[110] T. Luping, J. Gulikers, On the mathematics of time-dependent apparent chloride diffusion coefficient in concrete, Cem. Concr. Res. 37 (2007) 589–595. https://doi.org/10.1016/j.cemconres.2007.01.006.

[111] M.D.A. Thomas, P.B. Bamforth, Modelling chloride diffusion in concrete Effect of fly ash and slag, Cem. Concr. Res. (1999) 9.

[112] V. Elfmarkova, P. Spiesz, H.J.H. Brouwers, Determination of the chloride diffusion coefficient in blended cement mortars, Cem. Concr. Res. 78 (2015) 190–199. https://doi.org/10.1016/j.cemconres.2015.06.014.

[113] M. Shafikhani, S.E. Chidiac, A holistic model for cement paste and concrete chloride diffusion coefficient, Cem. Concr. Res. 133 (2020) 106049. https://doi.org/10.1016/j.cemconres.2020.106049.

[114] N. Olsson, F. Abdul Wahid, L.-O. Nilsson, C. Thiel, H.S. Wong, V. Baroghel-Bouny, Wick action in mature mortars with binary cements containing slag or silica fume – The relation between chloride and moisture transport properties under non-saturated conditions, Cem. Concr. Res. 111 (2018) 94–103. https://doi.org/10.1016/j.cemconres.2018.06.006.

[115] V. Baroghel-Bouny, M. Thiéry, X. Wang, Modelling of isothermal coupled moisture–ion transport in cementitious materials, Cem. Concr. Res. 41 (2011) 828–841. https://doi.org/10.1016/j.cemconres.2011.04.001.

[116] M. Saeidpour, L. Wadsö, Moisture diffusion coefficients of mortars in absorption and desorption, Cem. Concr. Res. 83 (2016) 179–187. https://doi.org/10.1016/j.cemconres.2016.02.003.

[117] Q. Zeng, K. Li, T. Fen-chong, P. Dangla, Pore structure characterization of cement pastes blended with high-volume fly-ash, Cem. Concr. Res. 42 (2012) 194–204. https://doi.org/10.1016/j.cemconres.2011.09.012.

[118] J. Crank, The mathematics of diffusion, Oxford university press, 1979.

[119] L.-O. Nilsson, Moistenginst AB Rapport 1922 (2019-10–03), http://moistenginst.se/files/Burkmetoden_RAPPORT_1922_Moisture_Engineering_Institute_2019-10-03.pdf

[120] G. Hedenblad, Moisture permeability of mature concrete, cement mortar and cement paste, PhD thesis, Lund University, 1993.

[121] Q. Huang, Z. Jiang, X. Gu, W. Zhang, B. Guo, Numerical simulation of moisture transport in concrete based on a pore size distribution model, Cem. Concr. Res. 67 (2015) 31–43. https://doi.org/10.1016/j.cemconres.2014.08.003.

[122] Z.P. Bažant, L.J. Najjar, Nonlinear water diffusion in nonsaturated concrete, Matér. Constr. 5 (1972) 3–20. https://doi.org/10.1007/BF02479073.

[123] K. Sakata, A study on moisture diffusion in drying and drying shrinkage of concrete, Cem. Concr. Res. 13 (1983) 216–224. https://doi.org/10.1016/0008-8846(83)90104-7.

[124] D. Quenard, H. Sallee, Water vapour adsorption and transfer in cement-based materials: a network simulation, Mater. Struct. 25 (1992) 515–522. https://doi.org/10.1007/BF02472447.

[125] B. Perrin, V.B. Bouny, L. Chemloul, Methods of determination of the hydric diffusivity of hardened cement pastes, Mater. Struct. 31 (1998) 235–241.

[126] S. Diamond, Mercury porosimetry An inappropriate method for the measurement of pore size distributions in cement-based materials, Cem. Concr. Res. (2000) 9.

[127] J. Zhou, G. Ye, K. Van Breugel, Characterization of pore structure in cement-based materials using pressurization–depressurization cycling mercury intrusion porosimetry (PDC-MIP), Cem. Concr. Res. 40 (2010) 1120–1128.

[128] F. Avet, K. Scrivener, Investigation of the calcined kaolinite content on the hydration of Limestone Calcined Clay Cement (LC3), Cem. Concr. Res. 107 (2018) 124–135. https://doi.org/10.1016/j.cemconres.2018.02.016.

[129] P. Lura, O.M. Jensen, K. van Breugel, Autogenous shrinkage in high-performance cement paste: An evaluation of basic mechanisms, Cem. Concr. Res. 33 (2003) 223–232. https://doi.org/10.1016/S0008-8846(02)00890-6.

[130] L.-O. Nilsson, A comparison between different methods to determine moisture transport properties of cementitious materials, Report TVBM 3168 Building Materials, LTH, Lund University (2013).

Appendix

Figure A1 presents the weight loss of FA blended pastes versus root of time during drying at 50% and 75.5%RH up to 64 days. Figure A2 shows the weight loss of all 11 samples during the vapor diffusion test in RH 97-75. We can observe that the slope of P035 keeps decreasing until it reached a rather stable constant from 156 to 227 days. Fig. A3 illustrates the typical fitting results of mass loss during drying.

Figure A4 shows the relationships between CP and $D_{v,s}$ of pastes and Figure A5 presents the correlation between porosity and D_w (a), $D_{v.s}$ and D_v respectively. Table A1 and A2 illustrates the calculated parameters of 3 parallel tubes of different samples during drying at 50% and 75% RH. Table A3 demonstrates the conductivity of pastes and pore solution at 28 and 90 days, respectively.

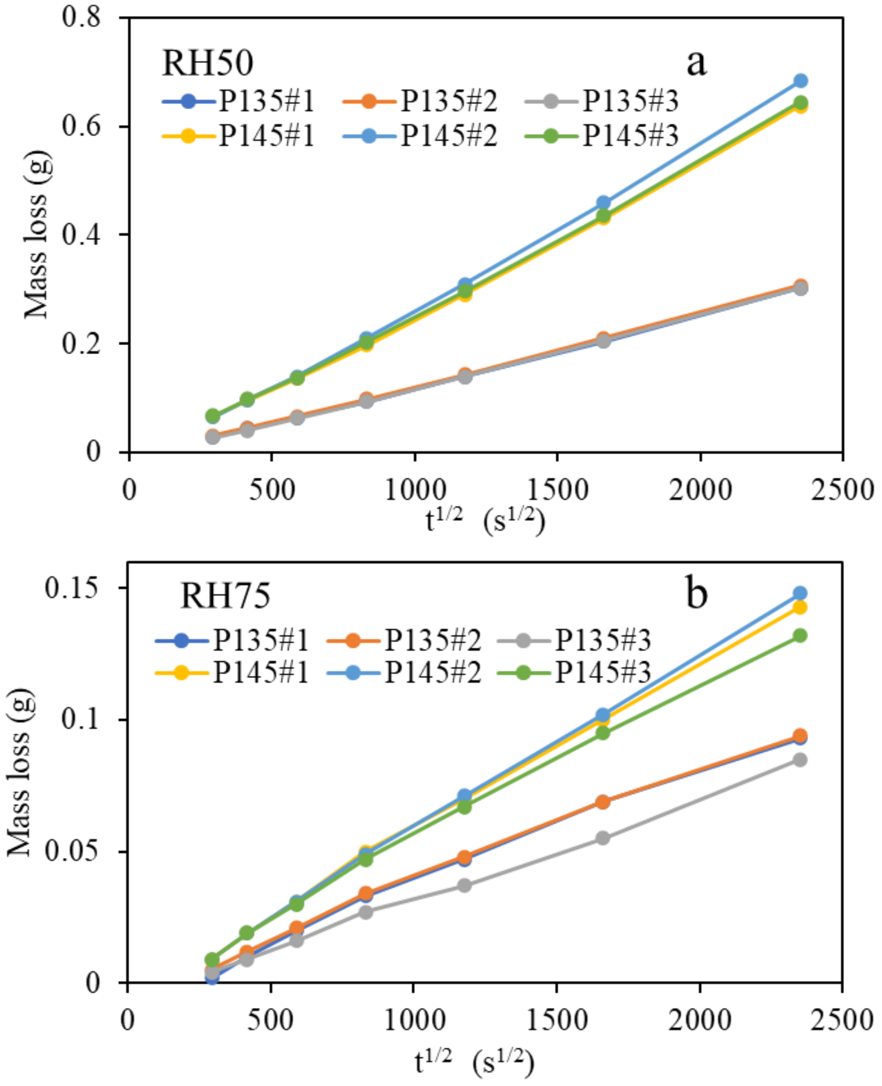

Figure A1. The weight loss of P1 tubes during its semi-infinite drying: a-under 50% RH; b-under 75% RH.

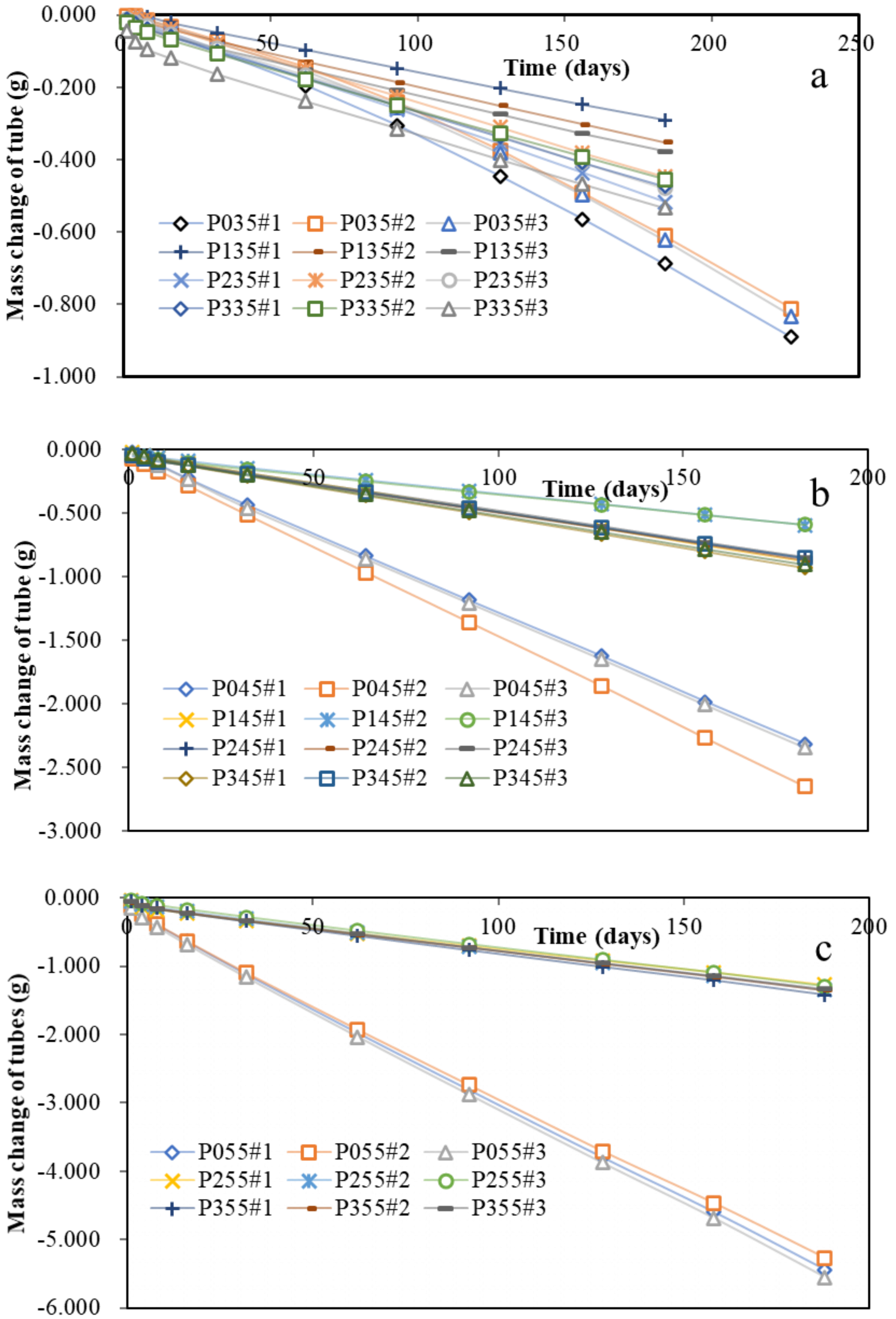

Figure A2. The weight change of 11 samples by tube method test in the RH interval from 97.6% to 75.5%: a-*w/b*=0.35; b-*w/b*=0.45 and c- *w/b*=0.55.

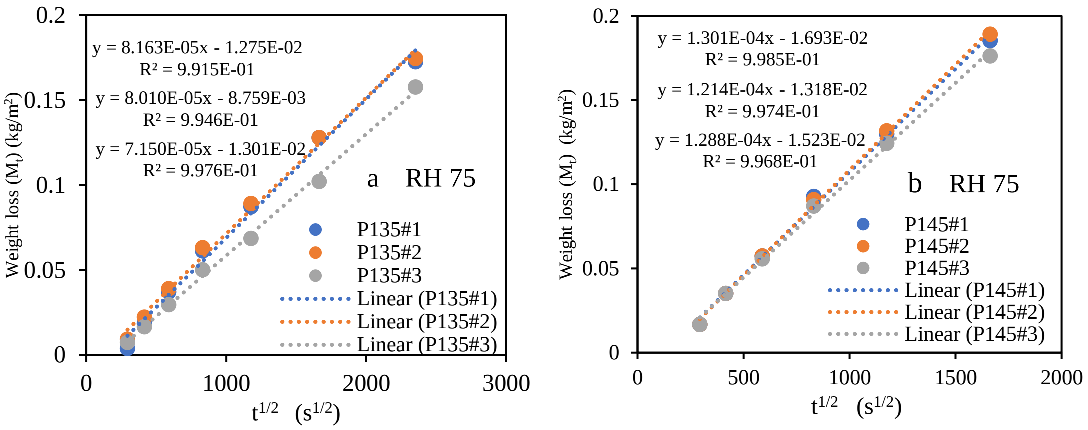

Figure A3. The typical fitting results of mass loss and square root of drying duration (P1 sample dried at 75.5% RH and 20 °C): a-*w/b*=0.35; b-*w/b*=0.45.

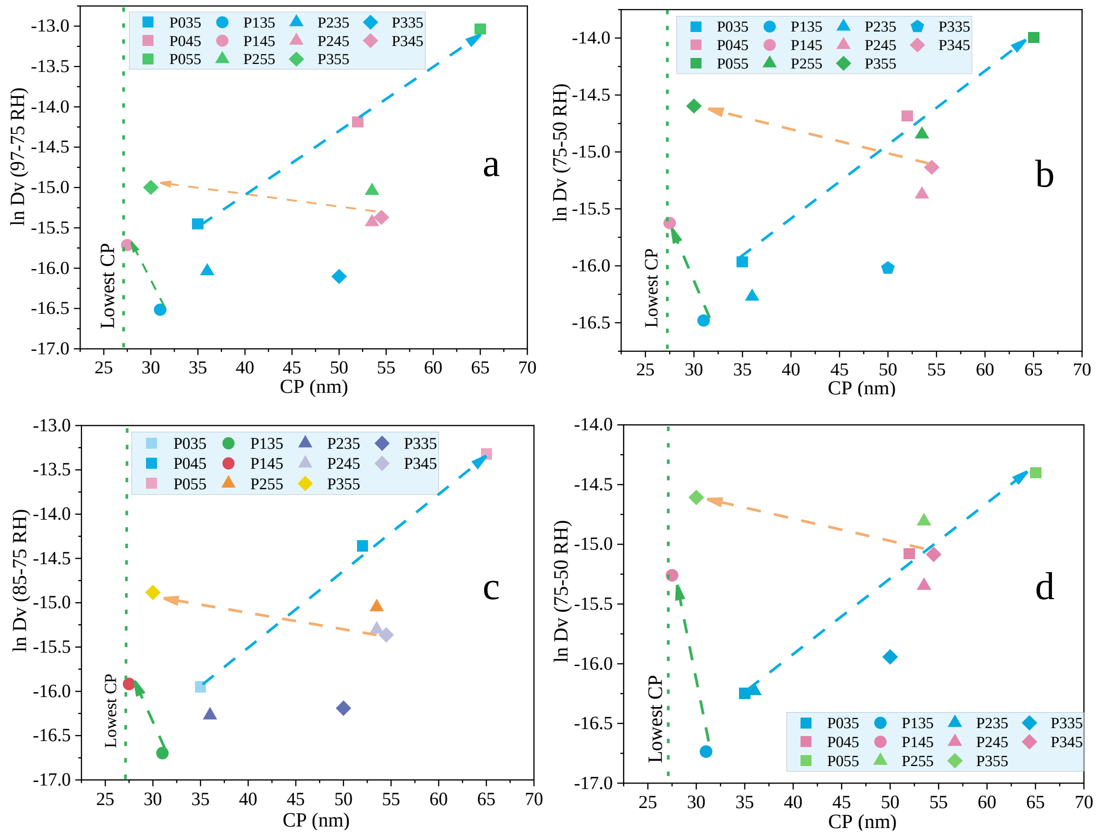

Figure A4. The relationships between CP and D_v of pastes.

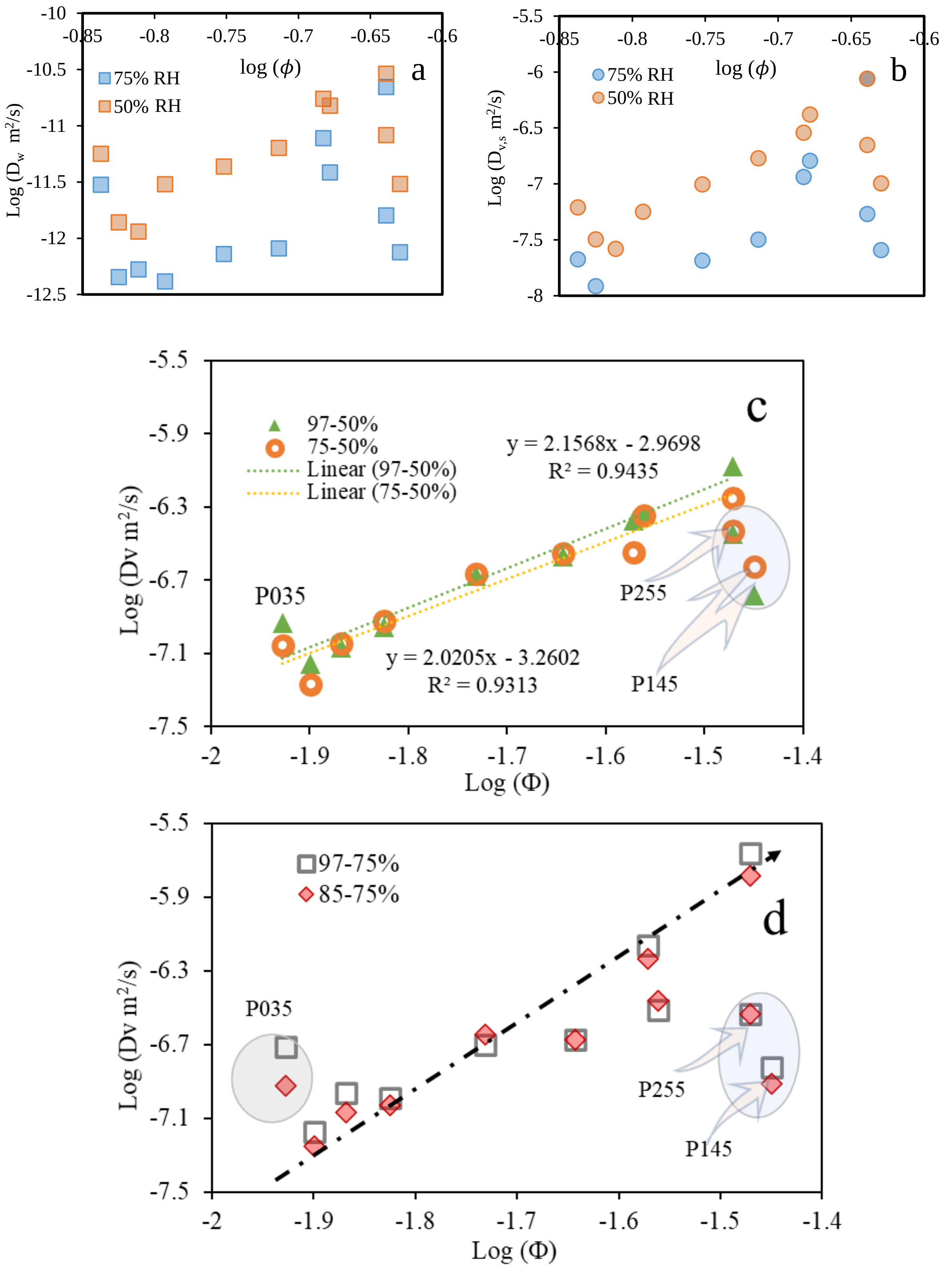

Figure A5. The correlations between porosity and D_w (a), $D_{v.s}$ (b), D_v in the intervals of 97-50% and 75-50% (c) and in the intervals of 97-75% and 85-75% (d).

Table A1. The calculated parameters of 3 parallel tubes of different samples during drying at 75% RH.

Samples	k_w(Kg/(m^{2}s$^{1/2}$))	dW(kg/m^3)	DW(m^2/s)	logD$_w$	Dvs(m^2/s)	Log D$_{v.s}$
P035	4.95E-05	25.64	2.92E-12	-11.53	2.06E-08	-7.69
	5.42E-05	25.64	3.51E-12	-11.45	2.48E-08	-7.61
	4.61E-05	25.64	2.54E-12	-11.60	1.79E-08	-7.75
P045	1.79E-04	56.58	7.84E-12	-11.11	1.17E-07	-6.93
	1.79E-04	56.58	7.84E-12	-11.11	1.17E-07	-6.93
	1.76E-04	56.58	7.58E-12	-11.12	1.13E-07	-6.95
P055	8.11E-04	149.83	2.30E-11	-10.64	9.06E-07	-6.04
	7.93E-04	149.83	2.20E-11	-10.66	8.68E-07	-6.06
	7.84E-04	149.83	2.15E-11	-10.67	8.47E-07	-6.07
P135	8.16E-05	102.26	5.00E-13	-12.30	1.35E-08	-7.87
	8.01E-05	102.26	4.82E-13	-12.32	1.30E-08	-7.89
	7.06E-05	102.26	3.74E-13	-12.43	1.01E-08	-8.00
P145	1.30E-04	129.31	7.89E-13	-12.10	2.68E-08	-7.57
	1.29E-04	129.31	7.79E-13	-12.11	2.65E-08	-7.58
	1.21E-04	129.31	6.92E-13	-12.16	2.35E-08	-7.63
P235	4.13E-05	50.84	5.18E-13	-12.29	6.93E-09	-8.16
	4.13E-05	50.84	5.18E-13	-12.29	6.92E-09	-8.16
	4.26E-05	50.84	5.51E-13	-12.26	7.37E-09	-8.13
P245	9.71E-05	107.92	6.35E-13	-12.20	1.80E-08	-7.74
	9.85E-05	107.92	6.55E-13	-12.18	1.86E-08	-7.73
	1.15E-04	107.92	8.87E-13	-12.05	2.52E-08	-7.60
P255	1.81E-04	127.56	1.58E-12	-11.80	5.32E-08	-7.27
	1.81E-04	127.56	1.59E-12	-11.80	5.33E-08	-7.27
	1.84E-04	127.56	1.63E-12	-11.79	5.45E-08	-7.26
P335	5.80E-05	75.90	4.59E-13	-12.34	9.17E-09	-8.04
	5.13E-05	75.90	3.59E-13	-12.44	7.17E-09	-8.14
	5.55E-05	75.90	4.21E-13	-12.38	8.40E-09	-8.08
P345	1.54E-04	148.04	8.51E-13	-12.07	3.31E-08	-7.48
	1.44E-04	148.04	7.47E-13	-12.13	2.91E-08	-7.54
	1.53E-04	148.04	8.42E-13	-12.07	3.28E-08	-7.48
P355	3.50E-04	158.28	3.83E-12	-11.42	1.60E-07	-6.80
	3.57E-04	158.28	4.00E-12	-11.40	1.67E-07	-6.78
	3.45E-04	158.28	3.73E-12	-11.43	1.55E-07	-6.81

Table A2. The calculated parameters of 3 parallel tubes of different samples during drying at 50% RH.

Samples	k_w(Kg/m^{2}s$^{1/2}$)	dW(kg/m^3)	DW(m^2/s)	logDw	Dvs(m^2/s)	Log Dv.s
P035	2.44E-04	88.35	5.99E-12	-11.22	6.52E-08	-7.19
	2.24E-04	88.35	5.06E-12	-11.30	5.51E-08	-7.26
	2.42E-04	88.35	5.90E-12	-11.23	6.42E-08	-7.19
P045	6.03E-04	134.05	1.59E-11	-10.80	2.62E-07	-6.58
	6.54E-04	134.05	1.87E-11	-10.73	3.09E-07	-6.51
	6.35E-04	134.05	1.76E-11	-10.75	2.91E-07	-6.54
P055	1.51E-03	243.07	3.02E-11	-10.52	9.04E-07	-6.04
	1.52E-03	243.07	3.06E-11	-10.51	9.16E-07	-6.04
	1.41E-03	243.07	2.66E-11	-10.58	7.95E-07	-6.10
P135	2.46E-04	186.57	1.36E-12	-11.87	3.13E-08	-7.50
	2.49E-04	186.57	1.40E-12	-11.85	3.22E-08	-7.49
	2.49E-04	186.57	1.40E-12	-11.85	3.22E-08	-7.49
P145	5.15E-04	269.93	2.86E-12	-11.54	9.52E-08	-7.02
	5.58E-04	269.93	3.35E-12	-11.47	1.11E-07	-6.95
	5.21E-04	269.93	2.92E-12	-11.53	9.71E-08	-7.01
P235	2.30E-04	185.09	1.21E-12	-11.92	2.77E-08	-7.56
	2.23E-04	185.09	1.13E-12	-11.95	2.59E-08	-7.59
	2.19E-04	185.09	1.10E-12	-11.96	2.51E-08	-7.60
P245	4.47E-04	185.09	4.58E-12	-11.34	1.04E-07	-6.98
	4.35E-04	185.09	4.33E-12	-11.36	9.87E-08	-7.01
	4.24E-04	185.09	4.11E-12	-11.39	9.38E-08	-7.03
P255	6.93E-04	217.80	7.96E-12	-11.10	2.13E-07	-6.67
	7.14E-04	217.80	8.44E-12	-11.07	2.26E-07	-6.65
	7.16E-04	217.80	8.48E-12	-11.07	2.27E-07	-6.64
P335	2.92E-04	151.31	2.93E-12	-11.53	5.46E-08	-7.26
	3.07E-04	151.31	3.23E-12	-11.49	6.02E-08	-7.22
	2.92E-04	151.31	2.93E-12	-11.53	5.46E-08	-7.26
P345	6.07E-04	216.25	6.19E-12	-11.21	1.65E-07	-6.78
	6.37E-04	216.25	6.81E-12	-11.17	1.81E-07	-6.74
	6.02E-04	216.25	6.08E-12	-11.22	1.62E-07	-6.79
P355	1.03E-03	224.82	1.63E-11	-10.79	4.52E-07	-6.34
	9.65E-04	224.82	1.45E-11	-10.84	4.00E-07	-6.40
	9.63E-04	224.82	1.44E-11	-10.84	3.99E-07	-6.40

Table A3. The conductivity of pastes and pore solution at 28 and 90 days.

Samples	Pastes (mS/cm)		Pore solution (mS/cm)	
	28 d	90 d	28 d	90 d
P035	0.576	0.424	165.641	165.641
P045	0.940	0.826	131.308	131.319
P055	1.221	1.244	102.947	102.950
P135	0.334	0.049	104.180	104.387
P145	0.536	0.082	88.549	92.612
P235	0.185	0.140	145.392	148.188
P245	0.280	0.184	110.835	113.472
P255	0.392	0.225	93.125	102.234
P335	0.143	0.108	115.272	123.082
P345	0.205	0.132	83.155	85.470
P355	0.265	0.172	69.834	74.487